

# **Long-term Effects of Dairies On Groundwater Nitrate**

## **Task Report 7**

Project

“Long Term Risk of Groundwater and Drinking Water  
Degradation from Dairies and Other Nonpoint Sources in the  
San Joaquin Valley”

Prepared by:

Dylan Boyle, Aaron King, Giorgos Kourakos, Katherine Lockhart, Megan Mayzelle,

Graham E. Fogg, Thomas Harter

August 2013

**STATE WATER RESOURCES CONTROL BOARD**

**Proposition 50 Nonpoint Source -- CALFED Drinking Water Quality Grant**

**SWRCB Agreement Number 04-184-555**

**Awarded to:**

**The Regents of the University of California, Davis**

This Project Report is not an official publication of the United States Geological Survey or the University of California Davis. It is provided for review and comment by interested parties, and not intended for general publication in print or electronic form. Rights to all material contained herein are retained by the authors, the United States Geological Survey, and the University of California. The rights for publication for material in some sections of this report have been assigned to other parties for the purpose of publication. Any further publication may be subject to prior copyright and require express permission. Information on publication venues may be obtained by contacting the principal investigators.

Suggested Citation:

Boyle, D., A. King, G. Kourakos, K. Lockhart, M. Mayzelle, G. E. Fogg, and T. Harter, 2013. Long-term effects of dairies on groundwater nitrate. Task Report 7. SWRCB Agreement Number 04-184-555. Department of Land, Air, and Water Resources. University of California, Davis. 86 pages.  
<http://groundwater.ucdavis.edu>.

# Table of Contents

---

Tables .....	5
Figures .....	6
Abstract .....	10
1. Introduction and General Conceptual Overview of the Approach .....	11
1.1 Nonpoint Source Pollution a Global Groundwater Quality Threat .....	11
1.2 Key Differences Between Nonpoint Source Pollution and Point Source Pollution Dynamics .....	12
1.3 Groundwater Nonpoint Source Assessment Tools .....	13
1.4 Proposed Modeling Framework .....	15
2. Nonpoint Source Assessment Toolbox .....	17
2.1 Conceptual Approach .....	17
2.2 High Resolution Groundwater Velocity Field Computation .....	18
2.3 Transport Simulation: Streamlines .....	21
2.4 Streamline Computation .....	23
2.5 Unit Response Function Approach .....	25
2.6 Transport Simulation along Streamlines .....	26
2.7 Unit Response Function Parameterization .....	27
2.8 Summary of Construction Phase .....	27
2.9 Implementation Phase: Computing Breakthrough Curves at CDSs .....	28
3. Approach to Generate Representative Groundwater Velocity Distribution .....	30
3.1 Steady-state Model for Tulare Lake Basin .....	30
3.2 Conceptual Background .....	34
Well Generation Algorithm .....	34
3.3 Groundwater and Transport Simulation .....	42
4. NPSAT Implementation Based on Coarse Model .....	50
5. Results .....	54
5.1 Nitrogen Loading Scenarios .....	54

---

5.2 Model Validation..... 60

5.3 NPSAT Modeling Predictions ..... 68

6. Conclusions ..... 76

7. Acknowledgments..... 77

8. References ..... 78

## Tables

---

No Tables for this Task Report

## Figures

---

Figure 1. Typical spatial variability of a land use (and implicitly, associated diffuse pollution) in an intensively managed semi-arid agricultural region with significant groundwater pumping for irrigation (black dots), Tule River Groundwater Subbasin, Central Valley Aquifer System, California. (Source: modified from Ruud et al. 2004.).....	12
Figure 2. Schematic illustration of Simplistic Domain Decomposition Method. ....	20
Figure 3. Left) Geometric definition of symbols involved in the weight calculation, Right) Weight function. ....	21
Figure 4. Distribution of exit points around the well screen. ....	22
Figure 5. Prism element. ....	24
Figure 6. Calculation of Unit Response Function. ....	27
Figure 7. Construction phase of the NPSAT. ....	28
Figure 8. Simulation phase of the NPSAT.....	29
Figure 9. Simulated cumulative annual changes in aquifer storage (reprinted with permission from: Faunt 2009, p. 77, Figure B9.). Red circled area indicates the years chosen to represent steady-state stress conditions. ....	31
Figure 10. Water budget of CVHM, where “delivery requirement” is the irrigation water requirement from both groundwater and surface water sources. (Reprinted with permission from: Faunt 2009, p. 73, Figure B6.).....	32
Figure 11. Steady state head distribution for the water year 1996.....	33
Figure 12. Comparison of averaged heads against the monthly heads used for averaging.....	34
Figure 13. Empirical cumulative distribution function of maximum well pumping rate.....	35
Figure 14. Empirical cumulative distribution function of well depth [m] (distance between water table and bottom of the well screen). ....	35
Figure 15. Correlation between well depth and screen length. ....	36

Figure 16. Left) Empirical cumulative distribution function of the number of wells per square mile. Right) histogram of the number of simulated wells per square mile. ....	37
Figure 17. Locations and pumping rates of simulated wells in the TLB study area. ....	38
Figure 18. Empirical cumulative distribution function of simulated pumping rates. ....	39
Figure 19. Sampling range for screen length. ....	40
Figure 20. Empirical cumulative distribution function of Simulated well depth (distance between simulated water table and bottom of the well). ....	41
Figure 21. Correlation between simulated well depths and screen lengths. ....	41
Figure 22. Discretization based on finite elements. The red lines correspond to the cells of the CVHM model. The dense black areas indicate the highly detailed discretization around the wells. ....	43
Figure 23. Histogram of degrees of freedom for the simulated subdomains. ....	44
Figure 24. Domain decomposition of study area into overlapping subdomains. The strips correspond to the overlapping zone. ....	45
Figure 25. Illustration of weighting scheme between adjacent subdomains. ....	46
Figure 26. Computed streamlines based on the fine simulation model. ....	48
Figure 27. Unit Response Functions. ....	49
Figure 28. Streamlines based on coarse model and analytical particle tracking. ....	51
Figure 29. Comparison of the distribution of streamline length [m] and age [years] between the two simulation models. A log of 0, 1, 2, 3, and 4 corresponds to 1, 10, 100, 1000, and 10,000 units (m or years), respectively. ....	52
Figure 30. Comparison between streamlines computed with the detailed and coarse model. Red streamlines correspond to detailed model and blue to coarse model. Top panel shows the overall streamline shapes of the 100 streamlines for a particular well. The bottom panels show the orbits of particles around the wells. Due to the absence of a cone of depression on the coarse model (blue lines) the streamlines are actually straight lines. ....	53
Figure 31. Cumulative probability distribution of N loading per year assigned to each streamline. The left panels correspond to N loading with units kg/ha -output of N loading algorithm Technical Report 2 (Viers et al. 2012), while the right panels correspond to the actual loading of N as nitrate (45 mg/L drinking	

water limit), which is used as input to NPSAT simulation model. All scenarios here are “by study area” and are explained in Section 1.8 of Technical Report 2 (Viers et al. ,2012). ..... 56

Figure 32. Exceedance probabilities of N loading rates as nitrate. All scenarios used here distribute excess nitrogen “by study area” and are explained in Section 1.8 of Technical Report 2 (Viers et al. ,2012). ..... 57

Figure 33. Cumulative distribution function of N loading based on the coarse model. All scenarios used here distribute excess nitrogen “by study area” (see Section 1.8 of Technical Report 2, Viers et al. ,2012). ..... 59

Figure 34. Exceedance probabilities of leaching rates as nitrate based on coarse model.. All scenarios used here distribute excess nitrogen “by study area” (see Section 1.8 of Technical Report 2, Viers et al. ,2012). ..... 60

Figure 35. Decadal means of nitrate concentration for the three regions based on measured data. The solid line represents the mean and the dashed line the confidence interval. .... 61

Figure 36. Decadal exceedance probabilities based on measured data. The solid line represents the de-clustered mean exceedance probability within each region and the dashed line the 95% confidence interval. .... 62

Figure 37. De-clustered, back-transformed mean of equal area log nitrate medians in each region of annual well means. Comparison of mean and 95% confidence interval between measured data and model predictions. .... 63

Figure 38. Comparison of decadal trends of exceedance probability of 9 mg/L, between measured data and model predictions. .... 65

Figure 39. Comparison of decadal trends of exceedance probability of 22.5 mg/L, between measured data and model predictions. .... 66

Figure 40. Comparison of decadal trends of exceedance probability of 45 mg/L, between measured data and model predictions. .... 67

Figure 41. Breakthrough curves based on model simulation for each well for the four alternative (by study area) scenarios (thin colored lines). The black thick lines correspond to exceedance probabilities and the red lines show the drinking water limit (45 m/L). Scenario details are provided in Section 1.8 of Technical Report 2 (Viers et al., 2012). ..... 69

Figure 42. Comparison between coarse model and fine model based on scenario D. .... 71

Figure 43. Comparison between scenario A and C based on the fine model predictions. .... 72

Figure 44. Exceedance probabilities for 22.5, 45, and 90 mg/L based on the fine model. .... 73

Figure 45. Exceedance probabilities for 22.5, 45, and 90 mg/L based on the coarse model. .... 74

## Abstract

---

The increase in groundwater nitrate concentration measured in domestic wells, irrigation wells, and public supply wells lags significantly behind the actual time of nitrate discharge from the land surface. The lag is due, first, to travel time between the land surface or bottom of the root zone and the water table, which ranges from less than 1 year in areas with shallow water table (<3 m (10 ft)) to several years or even decades where the water table is deep (>20 m (70 ft)). High water recharge rates shorten travel time to a deep water table, but in irrigated areas with high irrigation efficiency and low recharge rates, the transfer to a deep water table may take many decades.

Once nitrate is recharged to groundwater, additional travel times to shallow domestic wells are from a few years to several decades, with travel times of one to several decades, and even centuries, for deeper production wells.

Further information (publications, related reports, multi-media materials) is available at <http://groundwater.ucdavis.edu>.

# 1. Introduction and General Conceptual Overview of the Approach

---

## 1.1 Nonpoint Source Pollution a Global Groundwater Quality Threat

Nonpoint source (NPS) pollution of groundwater has been recognized as a key water quality problem worldwide (WWAP, 2009). Agriculture is considered the most dominant NPS polluter of groundwater, primarily through emissions of nitrogen and salt, but also pesticides and other farm-chemicals (Humenik et al., 1987; Bower, 2000; VanDrecht et al., 2003; Vitousek et al., 2010; Watanabe et al., 2010). Nitrate-nitrogen is considered by far the most common type of groundwater contamination associated with agricultural activities (e.g., Spalding and Exner, 1993; Harter et al., 2002; Spruill et al., 2002; VanDrecht ,et al. 2003; Burow et al. 2010). Groundwater nitrate is largely derived from fertilizer nitrogen and animal nitrogen applied in agriculture, where nitrogen is a vital nutrient for plant growth (WWAP 2006, p. 117). The increasingly intensive use of nitrogen-based fertilizers in agriculture has allowed global food production to stay ahead of rapid population growth (Almasri and Kaluarachchi 2007; Stadler et al., 2008; Laftouhi et al., 2003), but at potentially significant cost to current and future water quality in production wells (Corwin and Wagenet, 1996). With further growing world population and higher standards of living, food consumption is estimated to increase 70% over the next four decades, while global land and water resources have limited growth reserves. Intensification of agriculture will therefore continue (Molden, 2007). Besides nitrate, long-term salinization of groundwater basins from nonpoint sources, particularly in semi-arid and arid irrigated agricultural regions is a second critical threat to groundwater quality around the globe (Burkhalter and Gates, 2005; Martín-Queller et al., 2010).

The degradation of groundwater resources not only impacts ecosystems worldwide via return flow of groundwater to surface water (Bouwman et al., 2009), but it affects both irrigation water (salinity) and drinking water quality (nitrate, salinity, pesticides, pathogens). Approximately half of the global population depends on groundwater as a drinking water source (UN WWAP, 2003; Giordano, 2009). In contrast, most of the global population in intensively farmed agricultural regions such as the California Central Valley, the North-American High Plains and Floridan aquifers, Central Europe's unconsolidated aquifers, the Indo-Gangetic aquifer complex, and the North China plains, relies on – often shallow – groundwater (e.g., Power and Schepers, 1989; Chakraborti et al., 2011). Globally, 43% of consumptive water used in irrigation is groundwater (Siebert et al. 2010). Furthermore, particularly in Europe and North America, the need to protect drinking water quality for large populations sectors has driven and continues to drive NPS policy (e.g., Sonneveld and Bouma, 2003; Dowd et al., 2008 ).

Sound policy requires thorough scientific understanding of nonpoint sources and how they work, and of the linkage between nonpoint sources and groundwater discharges to users or affected

ecosystems (domestic wells, irrigation wells, urban/municipal wells, springs, discharges to stream reaches). Significant scientific effort has been dedicated to understand, manage, and monitor potential sources, to understand the dynamics of NPS pollutants in the vadose zone and in groundwater, and to assess the environmental and public health consequences of NPS pollution of groundwater (Addiscott and Wagenet, 1985; Corwin et al., 1999; Pavlis et al., 2010). The spatio-temporal and process complexity of NPS pollution of groundwater on one hand and the number and large diversity of affected stakeholders on the other hand (Figure 1) requires management of large datasets, the bridging of possibly huge datagaps, upscaling, the use of potentially complex models, and – most importantly – that science effectively communicates with policy and decision makers (King and Corwin, 1999; National Research Council 1993).

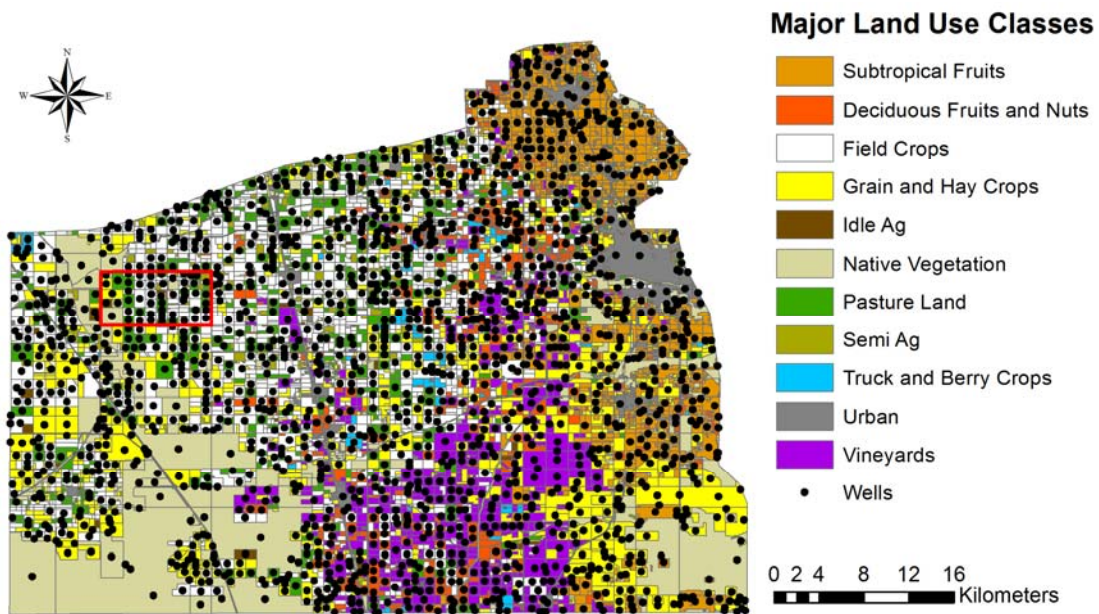


**Figure 1. Typical spatial variability of a land use (and implicitly, associated diffuse pollution) in an intensively managed semi-arid agricultural region with significant groundwater pumping for irrigation (black dots), Tule River Groundwater Subbasin, Central Valley Aquifer System, California. (Source: modified from Ruud et al., 2004.)**

### **1.2 Key Differences Between Nonpoint Source Pollution and Point Source Pollution Dynamics**

Agricultural activities are the dominant nonpoint source of groundwater nitrate and salts. Other significant sources include urban wastewater discharge, septic systems, wastewater holding ponds, and atmospheric deposition. For assessment, planning, and regulatory purposes, nonpoint source pollution, particularly from nitrate and salt, has a distinctly different problem set than point sources:

1. Control measures for point sources have been in development now for four decades (e.g., U.S. Code Title 42 Chapter 103 U.S. Comprehensive Environmental Response, Compensation and Liability Act of 1980), while control and monitoring measures for nonpoint sources of groundwater have only begun to be developed over the last one to two decades (e.g., EU Nitrate Directive<sup>1</sup> and California Salt and Nutrient Basin Plan<sup>2</sup> development).
2. Point sources, most commonly, are accidental spills of limited duration contributing a negligible fraction of basin recharge. Nonpoint sources are commonly associated with natural or intentional, managed or unmanaged sources of recharge that provide a significant fraction or even the majority of a groundwater basin's recharge on a time-varying but continuous basis (GWSP, 2008; UN/WWAP, 2006; Burow et al., 2010).
3. Point sources tend to be of limited spatial and temporal extent. One-time spills may occur over areas from less than 0.1 ha (0.25 acres) to few ha in size (Freeze and Cherry, 1979; Bower, 2000; Domenico and Schwartz, 2008). In contrast, nonpoint source pollution can occur repeatedly across the majority of the land surface area of entire groundwater basins, particularly in agricultural regions. Sources are spatially near-contiguous, while individual source facilities (liable parties) range from ten to several hundred hectares in size and are characterized by large spatial as well as temporal variability and, hence, uncertainty. For example the volume of irrigated water and its concentration in nitrogen vary significantly with crop type and season. In addition there is significant uncertainty related to the estimated amounts of excess nitrate that leach to groundwater (Loague and Corwin, 1998). Similar uncertainty exists in rain-fed crops, where nitrate leaching depends on various factors such as rainfall intensity, air temperature (Xin-Qiang et al., In press), the form of nitrogen application (Pilbeam et al., 2004), N application rate, form, and timing (Basso et al., 2010), etc.
4. Point sources of pollution are often very intensive (i.e., the associated pollution level (concentration) at and near the source can be many orders of magnitude above the regulatory limit). Nonpoint source pollution is typically of low intensity (i.e., at concentration levels near the regulatory limit and up to one order of magnitude above the regulatory limit (e.g., nitrate and salts)) (Burow et al., 2010).

These differences between point source pollution and nonpoint source pollution of groundwater require that assessment methods, monitoring approaches, and regulatory frameworks for nonpoint source control do not simply copy the approaches taken in the point source arena, but that methods are developed specifically for nonpoint sources.

### **1.3 Groundwater Nonpoint Source Assessment Tools**

Studies have developed various modeling tools for assessing and predicting aquifer pollution impacts or concentration levels in response to land use and management strategies. These models can be generally grouped into three categories:

---

<sup>1</sup> [http://ec.europa.eu/environment/water/water-nitrates/index\\_en.html](http://ec.europa.eu/environment/water/water-nitrates/index_en.html)

<sup>2</sup> [http://www.swrcb.ca.gov/centralvalley/water\\_issues/salinity/index.shtml](http://www.swrcb.ca.gov/centralvalley/water_issues/salinity/index.shtml)

1. Overlay and index methods, where different parameters of spatially distributed hydrologic, geographic, soils, and source information are combined to give an estimation of the vulnerability in the form of an index (National Research Council, 1993; Pavlis et al., 2010) such as DRASTIC (Aller et al., 1987), SINTACS (Civita and De Maio, 2004), etc.
2. Statistical methods that estimate the vulnerability by correlating spatial variables with actual occurrence of pollutants in the groundwater (Pavlis et al., 2010) such as regression (Nolan et al. 2002; Worrall et al. 2000), fuzzy logic (Uricchio et al., 2004), etc.
3. Process based methods to simulate the contaminant transport using mathematical formulas (Fogg et al., 1999).

The majority of these latter models are limited to the simulation of pollutants in the vadose zone, while simple methods such as zero-order mixing models (Mercado 1976; Lee 2007) or vertical plug-flow models (Refsgaard et al., 1999; Hansen, 1991; Cho and Mostaghimi, 2009) are used for the estimation of the fate of contaminants in the saturated zone. These kinds of approaches are not able to properly capture the spatial and temporal variability of contaminant loading across large aquifer systems.

Detailed spatio-temporal nonpoint source impact assessment in an aquifer requires numerical flow and transport models in two and three dimensions. A few studies developed analytical solutions to governing flow and transport equations (Leij & Dane, 1990; Fry et al., 1993; Perez-Guerrero et al., 2009); however, their applicability is limited to simple geometry cases under special boundary conditions. Coupled numerical solution schemes of groundwater flow and transport have been applied in groundwater remediation studies and nonpoint source prediction models at relatively small scale sites (Trowsdale and Lerner, 2007) or large scales (Carle et al., 2006), but often using relatively coarse gridded solutions (Almasri and Kaluarachchi, 2007; Jiang and Somers, 2009; Zhang and Hiscock, In Press).

The implementation of a fully three-dimensional flow and transport model for nonpoint source assessment is largely limited by computational resources; typically, current numerical flow and transport models are designed with  $10^5$  to  $10^8$  degrees of freedom (particle lines, finite difference cells, finite elements), allowing for  $10^2 - 10^3$  discretization points per dimension. At typical (point source) contamination sites to which these are applied, the resulting spatial discretization is on the order of  $10^{-1}$  to  $10^2$  meters (Carle et al., 2006). On the other hand, the simulation of entire groundwater basins affected by, for example, agricultural nonpoint source pollution, being tens to hundreds of kilometers across (e.g., Floridan aquifer system, High Plains aquifer system, Central Valley aquifer system, North China Plain aquifer system, Indo-Gangetic aquifer system), would require spatial grids that are four to six orders of magnitude larger ( $10^9 - 10^{14}$  degrees of freedom), at effectively similar discretization. The latter is necessary to properly capture individual sources (e.g., crop fields, lagoons, septic leach fields) and the impacts to individual contaminant sinks or receptors (wells, stream reaches, springs) across a basin (Bloomfield et al. 2006). The application of classic numerical contaminant modeling approaches to model nonpoint sources and their impacts at multiple locations (sinks) across entire basins is generally beyond current computational capacities. This is particularly true if the focus is on the impact to individual production wells (domestic, municipal, irrigation), of which there may be tens of thousands across a single groundwater basin.

To render the computational burden tractable, alternative methods have been proposed. For example Lin et al. (2010) developed a simplified numerical model where the governing equations of 3D groundwater flow and contaminant transport are replaced by a 2D finite element approximation in x-y direction, with a 1D finite difference approach for the vertical direction. Almasri and Kaluarachchi (2007) used surrogate models such as Modular Neural Networks in order to predict nitrate contamination in the Sumas-Blaine aquifer in Washington State, but performance was found inferior to the classical fate and transport model.

A widely used alternative technique is the streamline simulation model, where a multi-dimensional simulation problem is decoupled into multiple one-dimensional problems (Martin and Wegner, 1979). Streamline models have been used extensively in petroleum engineering (Blunt et al., 1996; Baker et al., 2002). Jang and Choe (2002) utilized the streamline model to simulate solute transport in fractures, and found that the Breakthrough Curves (BTCs) from simulations matched excellently with experimental data. Bandilla et al. (2009) combined an analytic element based solution of groundwater flow with the streamline method neglecting transverse dispersivity effects. Recently, Herrera et al. (2010) proposed an improved version of the method for simulating reactive solute transport in porous media. Streamline methods have also been used for model calibration (Jang, 2007; Jang and Choe, 2002, 2004), where the flow domain is decomposed into streamlines and the calibration parameters are adjusted along the streamlines. The efficiency of the streamline method stems from neglecting transverse numerical dispersion. Depending on the modeling objective, the method is computationally far less demanding than a full three-dimensional solution at equivalent high resolution.

Although the streamline method has been established as a reliable alternative solution to simulate transport in aquifers, simulation time for long simulation periods can be exceptionally large. For environmental managers interested in evaluating or optimizing multiple nonpoint source management scenarios, these simulation models are not practical. Tools for efficiently evaluating the long-term impacts of past, current, and (alternate) future nonpoint source loading scenarios at the groundwater basin scale are still lacking.

#### ***1.4 Proposed Modeling Framework***

In this report we developed and use a very efficient, yet highly resolved transport simulation approach that accounts for and takes advantage of the distinct attributes of nonpoint source pollution (as opposed to point source pollution). Our objective is to design a Non Point Source Assessment Tool (NPSAT) applicable to large groundwater basins with a highly heterogeneous, but spatio-temporally continuous coverage of nonpoint sources, that gives stakeholders, decision makers, and environmental managers specific information on the time-dependent statistical distribution of nonpoint source pollutants in a finite-sized ensemble of discrete groundwater discharge surfaces (e.g., well screens and streambeds). The latter comprise a distributed set of discrete compliance surfaces, which can be further categorized (grouped) by significantly controlling factors such as depth, hydrogeologic sub-regions, landscape and land use regions, etc. The concentration history at a discharge surface is controlled by

aquifer properties and their spatial distribution, by groundwater pumping and other discharges, and by the spatio-temporally variable, continuous nonpoint source pollution fluxes across the recharge surfaces of the aquifer. Specifically, our objective is to develop an efficient physically-based hydrogeological modeling framework to predict time-dependent pollutant concentration histograms and their probability distributions for compliance surfaces in a groundwater basin under spatio-temporally variable nonpoint source loading.

## 2. Nonpoint Source Assessment Toolbox

---

### 2.1 Conceptual Approach

Groundwater flow is governed by Darcy's law and the conservation of mass (Bear, 1979):

$$\nabla \mathbf{q} + Q_s = \nabla(\mathbf{K}\nabla h) + Q_s = S \frac{\partial h}{\partial t} \quad (\text{Eqn. 5})$$

subject to appropriate initial and boundary conditions. Here,  $\mathbf{q}$  is the Darcy flux,  $h$  is the hydraulic head,  $\mathbf{K}$  is the hydraulic conductivity tensor,  $Q_s$  represents a vector of sources and/or sinks,  $S$  is the storage coefficient, and  $t$  represents time. The governing equation of contaminant transport in groundwater is (Bear, 1979):

$$R \frac{\partial c}{\partial t} = \nabla \cdot (\mathbf{D}\nabla c) - \nabla(\mathbf{v}c) + G \quad (\text{Eqn. 6})$$

where  $c$  is the concentration of the contaminant,  $\mathbf{v} = \mathbf{q}/\theta$  is the velocity field,  $\theta$  is the porosity of the porous medium,  $\mathbf{D}$  is the dispersion tensor,  $t$  represents time,  $G$  represents sources and sinks (e.g., via recharge, wells) and  $R$  is the retardation factor (Putti et al. 1990). Pollutant concentrations (Eqn. 6) in a groundwater basin are controlled by spatio-temporally variable, dynamic sources and sinks of water and associated (dissolved) pollutants (Figure 1) and by spatially distributed (heterogeneous) aquifer properties.

Of particular interest to groundwater quality protection and management is the pollutant concentration (historical, current, and future) in water discharged from a (finite) set of individual wells or gaining stream reaches (Compliance Discharge Surfaces-CDSs) within a groundwater basin. The pollutant concentration history of the well water or stream reach discharge is here referred to as the breakthrough curve (BTC). The BTC at the CDS is controlled by the pollutant loading history in the source area of the CDS and by the solute reactions and dispersion along the groundwater flow paths between source area and CDS. The CDS source area is defined as the recharge area associated with all groundwater flow discharging into the CDS. Generally, recharge and pollutant loading within the source area may be spatially and temporally variable and not all locations within the source area contribute to the associated CDS at all times, due to transient changes in groundwater flow direction.

To yield the solution of Eqns. 5 and 6 tractable for nonpoint source pollution at the basin scale, yet with sufficiently high resolution, we make three critical simplifications: first, we assume that groundwater flow is steady-state:

$$\nabla \cdot (\mathbf{K}\nabla h) + Q_s = 0 \quad (\text{Eqn. 7})$$

Second, we assume that transverse dispersion in Eqn. 6 is negligible (longitudinal dispersion only), and, third, we assume that pollutant reactions are limited to first order degradation, linear sorption, or a combination thereof.

We support the first assumption with the following heuristic consideration: a nonpoint source pollutant entering an aquifer at a specific location, but continuously over a period of time may discharge at multiple proximate CDSs at different times if groundwater flow is sufficiently transient. However, our focus here is on exceedance probabilities and hence on the ensemble set of BTCs across a group of CDSs (and, hence, a group of source areas), which are much less sensitive to transient changes in source area. Source areas of CDSs may partially overlap due to transient flow conditions. Hence, a steady-state flow approximation still allows for capturing both central tendencies (mean travel time) and the degree of variability of travel time within a CDS and between CDSs.

The second assumption is thought to introduce limited error, because the lateral extent of nonpoint sources is large relative to the length scale of transverse dispersivity or transverse macrodispersivity (Neuman, 1990; Gelhar et al., 1992; Kim et al., 2004). The third assumption has been found to be applicable to a wide range of nonpoint source pollutants, including salinity, nitrate, and pesticides (Beltman et al., 1995; Lindenschmidt, 2006; Almasri and Kaluarachchi, 2007).

The steady-state flow problem Eqn. 7 is separable from the transport problem Eqn. 6 and here solved subject to the appropriate aquifer domain and boundary conditions using a finite element method (FEM). The grid resolution is chosen to capture the spatial pollutant loading variability as well as the flow dynamics around individual CDSs with sufficient detail. For example, the average size of individual sources in a typical agricultural region (California, Central High Plains, North China Plains, Central Europe) varies from  $10^2$  to  $10^6$  m<sup>2</sup> ( $10^3$  –  $10^7$  ft<sup>2</sup>); hence, the maximum size of a side of an element is in the range from 10 m (~33 ft) to 1000 m (~3300 ft). Near the CDSs, resolution is on the order of 10 m (~33 ft) (e.g., Figure 1 (Pilot study area)) to provide appropriate flow field resolution near the well.

## ***2.2 High Resolution Groundwater Velocity Field Computation***

Nonpoint contamination sources exhibit significant variability across source types (agricultural crops, septic leach field, ponding basins/lagoons) and among similar sources managed by different landowners and subject to variable land uses (e.g., varying crops). Nonpoint source loading is also highly variable in time. To assess nitrate and other NPS pollution in domestic and public supply wells, spatial variability must be resolved to the scale of individual wells and their source area or finer. For some NPS pollutants, such as nitrate and salinity, which typically vary over a relatively narrow range near regulatory limits (+/- one order of magnitude), temporal variations of source loading at the annual and inter-annual scale drive subsequent well pollutant levels, while shorter-term and very small-scale variations in the pollutant signal are absorbed by the mixing that occurs in typical production well screens. Proper resolution of physical transport processes in groundwater requires high resolution

computer models and limits the application of process models to large groundwater basins ( $10^3$  to  $10^5$  km<sup>2</sup> ( $3.8 \times 10^2$  -  $3.8 \times 10^4$  mi<sup>2</sup>)). For example, the average size of individual sources in a typical agricultural region (California, Central High Plains, North China Plains, Central Europe) varies from  $10^2$  to  $10^6$  m<sup>2</sup> ( $10^3$  -  $10^7$  ft<sup>2</sup>) (i.e., the maximum size of a side of an element or cell likely is in the range from 10 m (33 ft) to 1000 m (3280 ft)). Process-based model applications have therefore been limited to site-specific studies of pollution, primarily point source pollution, particularly if aquifer heterogeneity is also considered.

In this report the process-based regional modeling is achieved by introducing an automated two-step domain decomposition method where the domain is first simulated using a coarse resolution and then is divided into several overlapping sub-domains for either sequential or parallel high resolution simulation of flow and transport. Boundary conditions for the sub-domains are interpolated from the coarse grid solution, while a weighted average scheme is used to smooth the velocity field across sub-domain boundaries.

In general Domain Decomposition (DD) Methods are special techniques for solving linear or non-linear systems of equations arising from the discretization of partial differential equations (Smith et al., 1996). The majority of the DD methods require intervention at a computing level that existing simulation models either do not provide (COMSOL, FEFLOW) or that is very difficult to implement (MODFLOW, MT3DMS, HYDROGEOSPHERE). Here we use a simplistic domain decomposition method, which has the advantage that it can be combined seamlessly with the majority of the existing simulation models.

According to the simplistic DD, the aquifer is initially treated as a single domain  $\Omega$  and simulated using a coarse discretization, resulting in a coarse hydraulic head field  $h^c$ . Secondly the domain  $\Omega$  is divided into  $N$  sub-domains  $\Omega_1, \Omega_2, \dots, \Omega_N$  of very fine resolution. In this report we choose to divide the domain into orthogonal sub-domains, but the same method can be extended to any arbitrary sub-domain shape. We define the boundaries  $\partial\Omega$  of domain  $\Omega$  as external, and the artificial boundaries  $\Gamma_n$  as internal. Note that  $\partial\Omega_n$  (i.e., the boundary of sub-domain) consists either of part of  $\partial\Omega$  and  $\Gamma_n$  or exclusively of internal boundaries  $\Gamma_n$ . To assign boundary conditions to internal boundaries  $\Gamma_n$  we use an interpolation method  $I_{\Omega \rightarrow \Gamma_n}$  where the unknown boundary conditions  $\Gamma_n$  are interpolated from the coarse solution  $h^c$  and the fine head field  $h_n^f$  for each sub-domain  $n$  is calculated independently. At the end of this process,  $h^f$  is the union of all individual simulation results  $h^f = h_1^f \cup h_2^f \cup \dots \cup h_N^f$ .

However, based on our simulation results already obtained, it was found that the resultant fine head field  $h^f$  exhibits discontinuities across the internal boundaries  $\Gamma_n$ . To alleviate this problem, we propose to offset the artificial sub-domains boundaries at a specified distance  $l_{of}$ , thus producing an overlapping zone of width  $2l_{of}$ . As shown in Figure 2 the aquifer domain can be of any arbitrary shape, and the simulated area of each sub-domain is defined as the intersection of domain  $\Omega$  and the extended sub-domain boundary. In Figure 2, the solid red lines correspond to the non-extended sub-domain and the green dashed lined to the extended sub-domain after the offset operation.

Let  $i$  be a discrete point, located within the  $j$  non-extended sub-domain and also within  $M$  extended sub-domains (eg., Figure 2, the point  $i$  is located within the 2<sup>nd</sup> non-extended sub-domain and in the 8<sup>th</sup> extended sub-domain eg.,  $M = 1$ ). Each sub-domain returns a slightly different solution  $h_i^j \neq h_i^k \neq h_i^{k+1} \neq \dots \neq h_i^M$  as a result of the different boundary conditions, where  $k \in [1, M]$  are the subdomain IDs. In the case of nonconforming meshes, an interpolated value is used for the heads  $h_i^k, h_i^{k+1}, \dots, h_i^M$ .

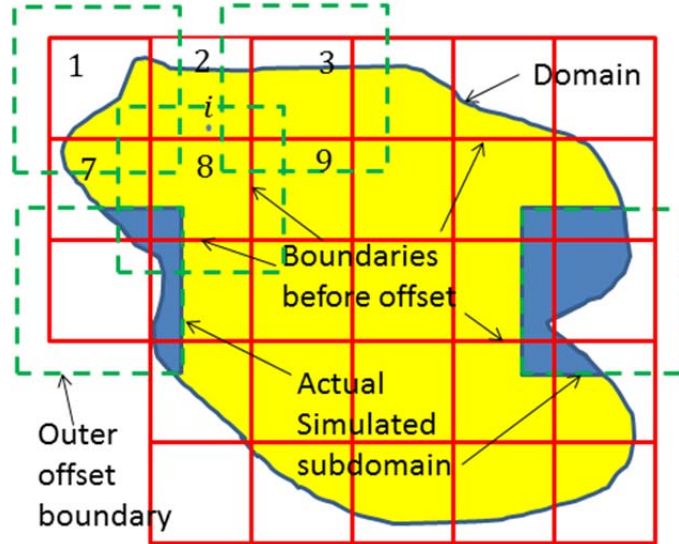


**Figure 2. Schematic illustration of Simplistic Domain Decomposition Method.**

Subsequently the  $M + 1$  head values can be averaged to obtain the head for point  $i$ . However, it has been observed that points closer to the boundaries have a larger head discrepancy from true head values. To counteract this problem, we propose a weighted average scheme, where the weights are taken proportional to the distance from the barycenter<sup>3</sup> of each sub-domain:

$$\bar{h}_i = \frac{1}{\sum_n^M w_i^n} \sum_{n=0}^M w_i^n h_i^n; n \in [j, k, k + 1, \dots, M] \quad (\text{Eqn. 8})$$

where  $h_i^n$  is the calculated head of point  $i$  based on the solution of sub-domain  $\Omega_n$  and  $w_i^n$  is the weight of point  $i$  with respect to sub-domain  $n$ , calculated by the following empirical formula:

$$w_i^n = \min \left\{ W \left( l_x/2, l_{of}, |x_i - x_c^n| \right), W \left( l_x/2, l_{of}, |x_i - x_c^n| \right) \right\} \quad (\text{Eqn. 9})$$

<sup>3</sup> The barycenter of an object is the center of Mass

where  $x_i, y_i$  are the coordinates of the point  $i$ ,  $l_x, l_y$  are the sub-domain lengths before the offset operator along the  $x$  and  $y$  directions, respectively (see Figure 3 left),  $x_c, y_c$  are the coordinates of the barycenter of the orthogonal and  $W$  is a geometric function defined as:

$$W(l, d, x) = \frac{x - (l + d)}{-2d} \quad (\text{Eqn. 10})$$

It can be seen from Eqn. 10, that input arguments  $l$  and  $d$  of Eqn. 10 are constants for each sub-domain. Eqn. 9 returns zero weights for the points that lie on the outer offset edges and weights of ones at the inner offset edges, with weights that vary linearly within the overlapping zone between these two numbers (Figure 3, Right). The negative weights outside the extended orthogonal are not used and they are ignored. The result of the above formulation is a smooth velocity field across the artificial boundaries.

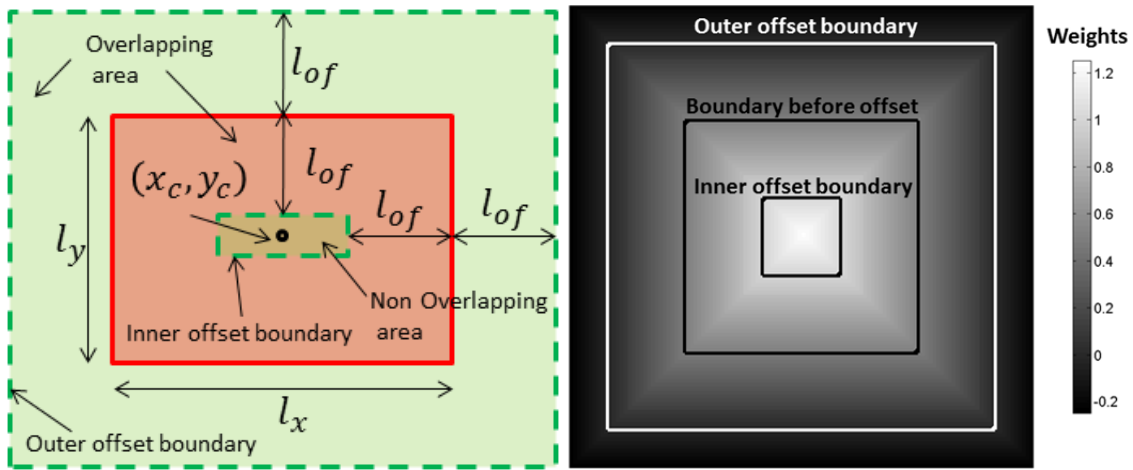


**Figure 3. Left) Geometric definition of symbols involved in the weight calculation, Right) Weight function.**

The velocity field is then used by transport simulation model of NPSAT for a highly efficient, streamline-based quasi-3D solution of an (arbitrary) solute transport equation yielding a pollutant unit response Functions (URF).

### 2.3 Transport Simulation: Streamlines

Neglecting transverse dispersion, the transport equation (Eqn. 6) is solved through an ensemble of one-dimensional streamline-based solutions focused on the CDSs rather than a fully three-dimensional solution. Obtaining a quasi-3D solution with the streamline approach specifically for CDS locations can be significantly more efficient than computing fully three-dimensional transient solutions over the entire groundwater nonpoint source contamination domain for time-horizons spanning decades to centuries (Thiele, 2001).

Here, we define streamlines by their exit points on the CDS and use backtracking to the source area (Figure 4). Exit points of streamlines are distributed across each CDS such that each streamline represents a known fraction of flow into the CDS. Streamline exit points around a well screen CDS are organized in multiple horizontal layers, each with a finite number of exit points per layer:  $N_s = N_l \cdot N_{ppl}$  where  $N_l$  is the number of layers,  $N_{ppl}$  is the number of exit points per layer and  $N_s$  is the total number of streamlines exiting on the well screen. Streamline contributions to the CDS BTC are weighted based on the exit velocity at the CDS.

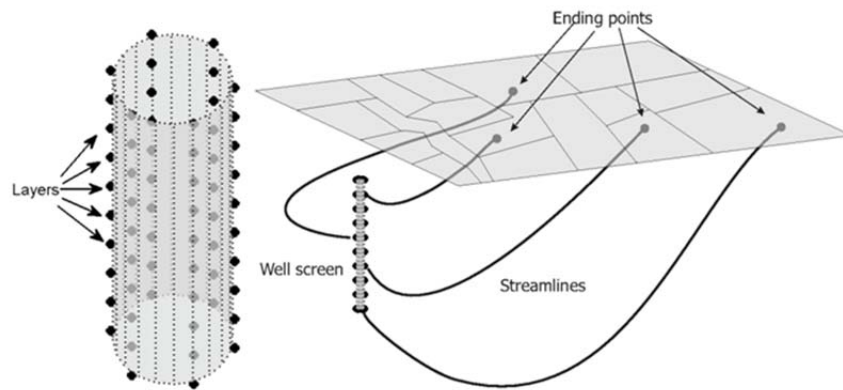


**Figure 4. Distribution of exit points around the well screen.**

The accuracy of the breakthrough curve simulation at the CDS is determined by the number of streamlines used relative to the (spatio-temporally variable) pollutant loading across the source area (source loading). For computational efficiency, a balance must be sought between accuracy and numerical efficiency. The choice of the number of streamlines used is application-specific and depends on the desired accuracy. Given typical uncertainties and inaccuracies associated with estimating groundwater flow parameters and source loading, a practical simulation goal is to obtain discharge (well) concentrations that have a numerical accuracy within 5% of the true mathematical solution or, alternatively, at the 5%–10% level of a problem-specific contaminant concentration level of interest (e.g., drinking water limits for nitrate, salinity), whichever is larger. Consider a nonpoint source concentration that varies between 10% (background) and 1,000% (intensive source) of the regulatory control level while recharge is relatively uniform. This is typical for nitrate and salinity pollution from agricultural landscapes (Harter et al., 2002; Burow et al., 2010). In this case, the scenario requiring the highest resolution occurs if 1% of the CDS source area has the maximum concentration of 1,000% of the regulatory control level, while the remainder of the source area recharges at a background concentration of only 10% of the regulatory control level. Hence, the high polluter adds ( $1\% \cdot 1000\% =$ )

10% of the regulatory concentration level to the background concentration at the CDS. The number of streamlines must be sufficiently large to ascertain that the procedure captures the 1% of the source area with high concentration. Generally, from  $10^2$  to  $10^3$  streamlines are therefore needed to properly simulate the BTC at such a CDS.

## 2.4 Streamline Computation

To define the streamline associated with each exit point on the CDS, a backward particle tracking is performed for each of the  $N_s$  exit points, and the positional and velocity vectors are computed for  $N_s \times N_{CDS}$  streamlines, where  $N_{CDS}$  is the number of CDSs included in the simulation area. Backward particle tracking for streamlines has two distinct advantages; transport is computed only for the part of the aquifer that is of interest to the simulation outcome (concentration hydrographs at contaminant sinks), and by using backward particle tracking to define streamlines, we avoid the so-called “weak-sink” problem in numerical solutions of (5) (Zheng and Wang, 1999).

For each starting point  $i_s \in [1, N_s]$  a backward particle tracking is performed until the particle intersects the water table, yielding a streamline  $S_{i_s}^{i_{CDS}}$ . In groundwater, the streamlines describe the time  $t$  for a particle to travel a certain distance  $s$  within the groundwater velocity field. Mathematically the streamlines are expressed by the following first-order, initial-value, ordinary differential equation:

$$\frac{d\vec{x}_p}{dt} = \vec{v}_p(\vec{x}_p, t) \quad (\text{Eqn. 11})$$

$$\vec{x}_p(t = \tau_p) = \vec{x}_{p_0}$$

where  $\vec{x}_p$  is the position vector,  $\vec{v}_p$  is the pore velocity vector, and  $\vec{x}_p(t = \tau_p)$  is the starting point (e.g., exit point of streamline Figure 4). Eqn. 11 can be solved analytically (Pollock, 1994) or numerically using any known numerical methods. In this report we used a hybrid numerical integration method. The method is a mix of the predictor-corrector scheme and the fourth order Runge-Kutta integration method. The method starts by calculating the velocity  $\vec{v}_p$  at a given point  $\vec{x}_p$ . The velocity is computed through interpolation based on the head field. Next we estimate a new point  $\vec{x}_{p+1}^{(1)}$  using an explicit Euler formula:

$$\vec{x}_{p+1}^{(1)} = \vec{x}_p + \vec{v}_p \cdot h \quad (\text{Eqn. 12})$$

Where  $h$  is a predefined step. According to the predictor-corrector scheme, the position  $\vec{x}_{p+1}^{(1)}$  is improved iteratively using the corrector:

$$\vec{x}_{p+1}^{(i+1)} = \vec{x}_p + \frac{1}{2}(\vec{v}_p + \vec{v}_p^{(i)}) \cdot h; i = 1,2,3 \quad (\text{Eqn. 13})$$

The iterations stop when the discrepancy between the positions of points  $i$  and  $i + 1$  is smaller than a specified threshold.

Typically, based on our simulations, the predictor-corrector scheme converges after 2–5 iterations. However, it was observed that in some cases (i.e., very irregular geometry of mesh elements) the predictor-corrector scheme either does not converge fast or in very few cases does not converge at all. To counteract this, we employed a fourth order Runge-Kutta integration method when the iterations of the predictor-corrector integration exceed a certain number without converging (e.g., 10). In these cases the new position  $\vec{x}_{p+1}^{(1)}$  is calculated using Eqn. 12 where  $\vec{v}_p$  is the weighted average of four velocities along the direction of flow.

A critical step in the particle tracking method is the computation of velocity, based on a hydraulic head field. In general, velocity is defined as the negative gradient of head divided by the aquifer porosity (i.e.,  $v = -K\nabla H/\theta$ , where  $K$  is the hydraulic conductivity tensor,  $H$  is the hydraulic head, and  $\theta$  is the porosity). According to the finite element method a continuous hydraulic head  $H(x, y, z)$  field is approximated as the weighted average of the heads  $H_i$  at specific discrete locations  $i = [1,2, \dots, N]$  (i.e., the nodes of the finite element mesh) weighted by the shape functions  $N_i(x, y, z)$ ,  $H(x, y, z) = \sum_{i=1}^N N_i(x, y, z)H_i$ . Similarly, the gradient of the hydraulic head is approximated as the weighted average of the heads  $H_i$  multiplied by the gradient of the shape functions  $\nabla N_i(x, y, z)$ . Since the hydraulic heads  $H_i$  are computed from the solution of the groundwater flow equation, the calculation of velocity is simplified to the calculation of the shape function derivatives. However in 3D models, shape function derivatives are very complex expressions of  $x, y, z$ . In this report we used exclusively prism elements (Figure 5) and isoparametric shape functions, which simplify the derivative calculations.

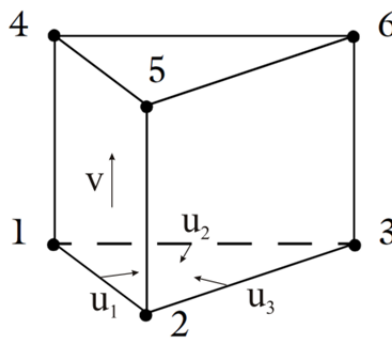


**Figure 5. Prism element.**

Isoparametric shape functions are defined on an element local coordinate system and in the case of prism elements are expressed as the following:

$$\begin{aligned}
N_1 &= u_1 (1 - v)/2 \\
N_2 &= u_2 (1 - v)/2 \\
N_3 &= u_3 (1 - v)/2 \\
N_4 &= u_1 (1 + v)/2 \\
N_5 &= u_2 (1 + v)/2 \\
N_6 &= u_3 (1 + v)/2
\end{aligned}
\tag{Eqn. 14}$$

where  $u_1 + u_2 = u_3$ . Note that shape functions are defined in a local coordinate system  $N(u_1, u_2, v)$  and velocity computation requires the derivatives with respect to the physical coordinate system  $\partial N(x, y, z)$ . However the conversion is straightforward and is obtained by the following equation:

$$\partial \mathbf{N}(x, y, z) = \mathbf{J}^{-1} \mathbf{G} \cdot \mathbf{N} \tag{Eqn. 15}$$

where  $\mathbf{G}$  is the gradient operator in the local coordinate system  $\mathbf{G} = [\partial/\partial u_1 \ \partial/\partial u_2 \ \partial/\partial v]^T$ ,  $\mathbf{N} = [N_1, N_2, \dots, N_6]$  and  $\mathbf{J} = \mathbf{G} \cdot \mathbf{N} \cdot [\mathbf{x} \ \mathbf{y} \ \mathbf{z}]$ , where  $\mathbf{x} = [x_1, x_2, \dots, x_6]^T$ ,  $\mathbf{y} = [y_1, y_2, \dots, y_6]^T$ , and  $\mathbf{z} = [z_1, z_2, \dots, z_6]^T$ .

In the above analysis we used linear shape functions. Higher order elements can be also used, at the expense of computational complexity and increased CPU runtime.

After the calculation of the streamlines, each one consists of a positional vector  $\mathbf{x}_i$ , and velocity vector  $\mathbf{v}_i$ . The positional vector  $\mathbf{x}_i$  contains the distance along the streamline  $S_{i_s}^{i_{CDS}}$  measured from the initial point  $i_s$ , and the velocity vector  $\mathbf{v}_i$  contains the velocity magnitude that corresponds to positions of vector  $\mathbf{x}_i$ . Note that the last element of vector  $\mathbf{x}_i$  is the key link of the streamline  $S_{i_s}^{i_{CDS}}$  with the nonpoint source loading function  $L_j$ ;  $j \in [1, N_{land}]$ , and eventually links each exit point on the CDS with a contamination source  $L_j$ .

## 2.5 Unit Response Function Approach

The linearization of the transport problem (Eqn. 6) allows for the application of the principle of superposition (Jury and Roth, 1990); the concentration history at any streamline exit point on the CDS, due to a temporally variable source loading history at the associated source boundary, can be computed as a superposition of solutions of the so-called unit response functions (URF). URFs have been widely used for the simulation of rainfall-runoff processes (Saghafian, 2006; Jukic and Denic-Jukic, 2009), where the URF is known as unit hydrograph. Researchers also employed URFs as transfer functions to simulate solute transport in the unsaturated zone (Jury, 1982; Jury et al., 1982, 1986; Jury & Roth, 1990; Heng and White, 1996; Stewart and Loague, 2003; Jaladi and Rowell, 2008; Mattern and Vanclooster, 2010) and in watersheds (Botter et al., 2006). Here, the transfer function concept explored in Jury and Roth (1990) is interpreted as a transfer function across a finite-sized three-dimensional streamtube linking a fraction of the source area with a fraction of the CDS. Each streamline represents an infinite number of stream-filaments (particle paths) within the associated streamtube (Ginn, 2002).

$$\frac{\partial c}{\partial t} = \frac{\partial}{\partial x} \left( D \frac{\partial c}{\partial x} - vx \right) \quad (\text{Eqn. 16})$$

## 2.6 Transport Simulation along Streamlines

For each streamline, a one-dimensional transport model is applied to compute the URF. Generally, any transport model may be applied within the NPSAT framework to compute the URF provided that the superposition principle can be applied (e.g., Continuous Time Random Walk (Berkowitz et al., 2006), Fractional Advection Dispersion equation (Meerschaert et al., 1999), the tempered one-sided stable residence time density (Cvetkovic, 2011), and others). Here, we use the one-dimensional Advection Dispersion Equation (ADE) (Jury and Roth, 1990):

subject to:

$$\begin{aligned} c(x, 0) &= 0 \\ c(0, t) &= 1 ; t > 0 \text{ (Heaviside step function input)} \\ \left( \frac{\partial c}{\partial t} \right)_{x=x_{\max}} &= 0 \end{aligned} \quad (\text{Eqn. 17})$$

where  $D$  represents the effective macrodispersion, given by  $D = \tilde{\alpha}_L v$ . The macrodispersivity,  $\tilde{\alpha}_L$  intrinsically accounts for the effects of aquifer heterogeneity within the streamtube represented by the 1D streamline. Consistent with field experiments (Gelhar et al., 1992) and numerical experiments (Green et al., 2010), the longitudinal macrodispersivity,  $\tilde{\alpha}_L$  is scaled relative to the length of the streamline,

$$\tilde{\alpha}_L = f(L_s) \quad (\text{Eqn. 18})$$

where  $L_s$  is the streamline length. The velocity varies along the streamline, and is calculated from the flow solution by the norm  $v = \sqrt{v_x^2 + v_y^2 + v_z^2}$ . The solution to Eqn. 16 is obtained numerically for each streamline. The streamline URF is computed from the resulting solution  $c(t)$

$$URF = c(t) - c(t - 1) \quad (\text{Eqn. 19})$$

This ensures that the area of the URF is always equal to 1 (Figure 6).

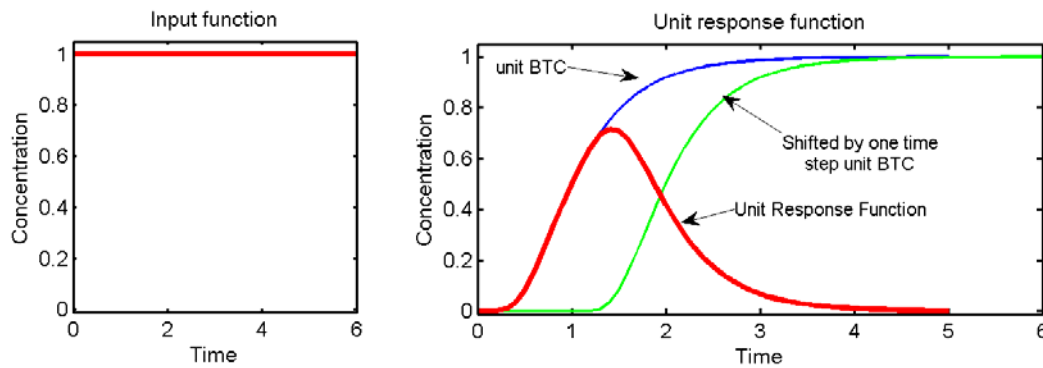


**Figure 6. Calculation of Unit Response Function.**

## 2.7 Unit Response Function Parameterization

Streamline URFs are archived for retrieval during the forecasting phase of the NPSAT. We found that the shape of the URFs is similar to that of common probability distribution functions (pdfs) found in the statistical literature and in statistical software. Both functions intrinsically integrate to a unit area. We can therefore readily fit the empirically determined URFs to a library of pdf functions using existing software. Pdfs are typically defined by two to three parameters and the function itself. The fitting procedure used consists of a gradient based optimization method aiming at minimization of the error between the empirical and fitted URF. Rather than archiving on the order of  $10^4 - 10^5$  bytes of data per CDS ( $10^2$  or more datapoints per each of  $10^2 - 10^3$  streamlines), this procedure reduces the archive to 3 to 4 numbers (2–3 parameters and one index to identify the function) per streamline or between  $10^2$  and  $10^3$  bytes of data per CDS. This allows for efficient data storage and forward modeling in applications to large groundwater regions, where the number of CDSs may range from  $10^4 - 10^6$  or even higher.

## 2.8 Summary of Construction Phase

Use of the URF approach computationally decouples the transport process from the nonpoint source loading process. URFs can be computed a priori without knowledge of the actual nonpoint source concentration history. We call this the NPSAT construction phase. The NPSAT construction phase requires the following steps (Figure 7):

- Geospatial mapping of the individual land use parcels and their (non-transient, average) recharge, of the CDSs (e.g., wells) and their (non-transient, average) discharge, and of other boundary conditions
- Computation of a detailed three-dimensional steady-state groundwater velocity field using a high-resolution numerical solution to Eqn. 7 with distributed recharge, groundwater pumping, and groundwater discharge to streams

- Geospatial mapping of the desired distribution of streamline exit points on the set of CDSs
- Backward computation of streamlines from their CDS exit points to the water table (source area)
- Computation of a URF as the one-dimensional solution of Eqn. 16 separately for each streamline, given a unit input step function, and fitting a parametric function to this empirically obtained URF at each streamline, a step that drastically reduces the data storage requirements.

The construction phase yields a geospatial database of the location of CDSs (wells, drains, springs, stream reaches), an identification of associated streamlines, the parameters and a code identifying the form-function of the URF for each streamline, and each streamline's recharge and discharge (beginning and end) location.

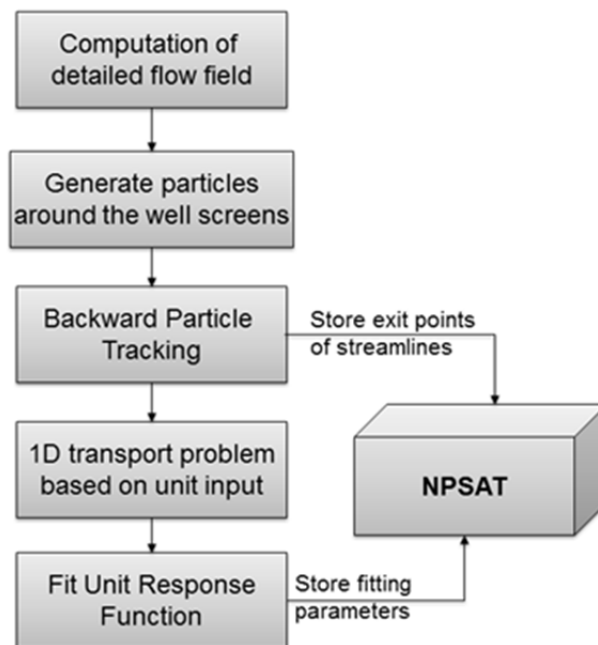


Figure 7. Construction phase of the NPSAT.

## 2.9 Implementation Phase: Computing Breakthrough Curves at CDSs

In the implementation phase of the NPSAT, the BTC of a CDS is computed by convoluting each streamline-specific unit response function with the actual, location-specific nonpoint source loading function, then performing a flux-weighted integration of streamline-output concentrations at time  $t$  over all streamlines exiting in a specific CDS (model prediction phase). Suppose that  $N_s$  streamlines and associated unit response functions  $\mathbf{URF} = \{URF_1, URF_2, \dots, URF_{N_s}\}$  were computed for the  $i_{CDS}^{\text{th}}$

compliance discharge surface. The source loading functions associated with the **URF** are denoted as  $L_i; i \in [1, N_s]$ . For each streamline, the concentration history is obtained by convolution:

$$BTC_j(t) = \sum_{d=0}^t L_j(t-d) \cdot URF_j(d) \quad (\text{Eqn. 20})$$

where  $d$  increases in the summation at time step intervals and  $t$  is the total runtime of the transport model. Eqn. 20 is the numerical approximation of the general convolution operator between two functions  $f$  and  $g$  expressed as  $f * g = \int_0^t f(\zeta)g(t-\zeta)d\zeta$ . After the calculation of the concentration history at each streamline, the BTC of the CDS is computed from:

$$\overline{BTC}_{i_{CDS}}(t) = \frac{1}{w_1 + w_1 + \dots + w_{N_s}} \sum_{j=1}^{N_s} w_j \cdot BTC_j(t) \quad (\text{Eqn. 21})$$

where  $w_j$  is the weight that represents the amount of flow that corresponds to each streamline.

Unlike in watershed NPS modeling, where the CDS output of individual stream reaches or tributaries is effectively integrated at the watershed outlet (Basso et al., 2010), the solute output at individual groundwater well CDSs does not further mix among CDSs (similarly in the case where a large number of low order stream reaches are considered separately). Instead, the BTCs provide the basis for constructing time-dependent pollutant exceedance probability distribution functions (pdfs) across user-specified specific population sets of CDSs (e.g., domestic wells, irrigation wells, drinking water wells, stream reaches) within the modeling domain. This stochastic analysis is the final step in the NPSAT process (Figure 8).

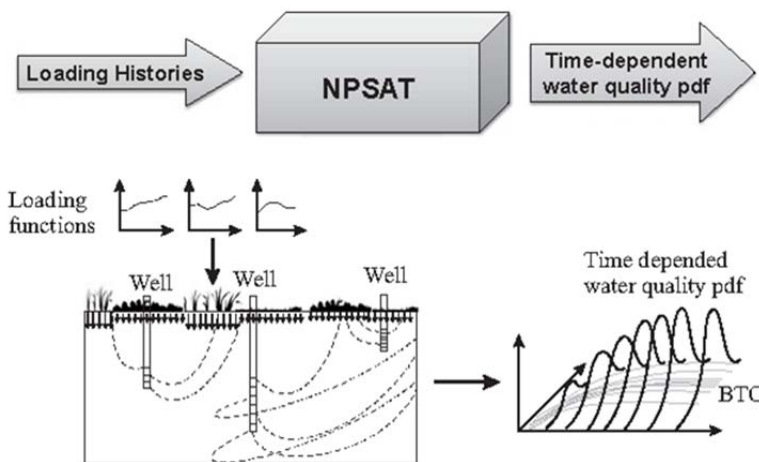


**Figure 8. Simulation phase of the NPSAT.**

## 3. Approach to Generate Representative Groundwater Velocity Distribution

---

One of the main assumptions of the proposed modeling approach is the aquifer flow field is steady state. While this assumption might not be valid when a monthly or even seasonal temporal scale for the analysis is used, it is justifiable with the rationale that the model will be used for prediction at the annual temporal scale (see justification in subsection 7.2.1 Conceptual approach).

To choose a representative steady state flow field for the study area we used two criteria: 1) the change of storage volume in the aquifer for the selected period should be as small as possible (i.e., the volume of water that entered the groundwater aquifer must be equal to the losses) and 2) the various stresses for the selected period have to correspond with the average stresses for the study area.

### 3.1 Steady-state Model for Tulare Lake Basin

For the TLB the analysis is based on the Central Valley Hydrologic Model (CVHM) (Faunt, 2009). The CVHM is a transient state groundwater model, with a monthly time step, coupled with the FARM process (Schmid et al., 2006) which is used as a water budget tool to estimate the groundwater stresses due to agricultural practices (e.g., groundwater recharge and pumping, etc.). The CVHM simulates the groundwater flow for the entire Central Valley aquifer for the years 1962 – 2003. According to CVHM transient simulation, the storage in the aquifer decreases over the 41-year simulation period. Figure 9 illustrates the cumulative change in groundwater storage for four basins of the Central Valley. The violet line corresponds to the TLB. It can be seen that, despite the general declining trend, there is a two-year period (1995 – 1997) where the change in storage is rather negligible (see red oval Figure 9). The next requirement is that the stresses need to be representative of the study area. Figure 10 shows the simulated water budget from the CVHM. In particular it shows the agricultural pumping, the surface water deliveries, the water delivery requirements for irrigation (groundwater plus surface water deliveries), and the landscape recharge. Note also that three years, 1975, 1990, and 1998, have been designated as typical, dry, and wet, respectively. Interestingly, for the years 1996 and 1997 the simulated agricultural pumping, surface water deliveries, total delivery requirements, and the landscape recharge are very close to those of the typical year (compare the ends of the arrows which point to the amount of acre feet per year for the typical year 1975, and the year 1996 in Figure 10).

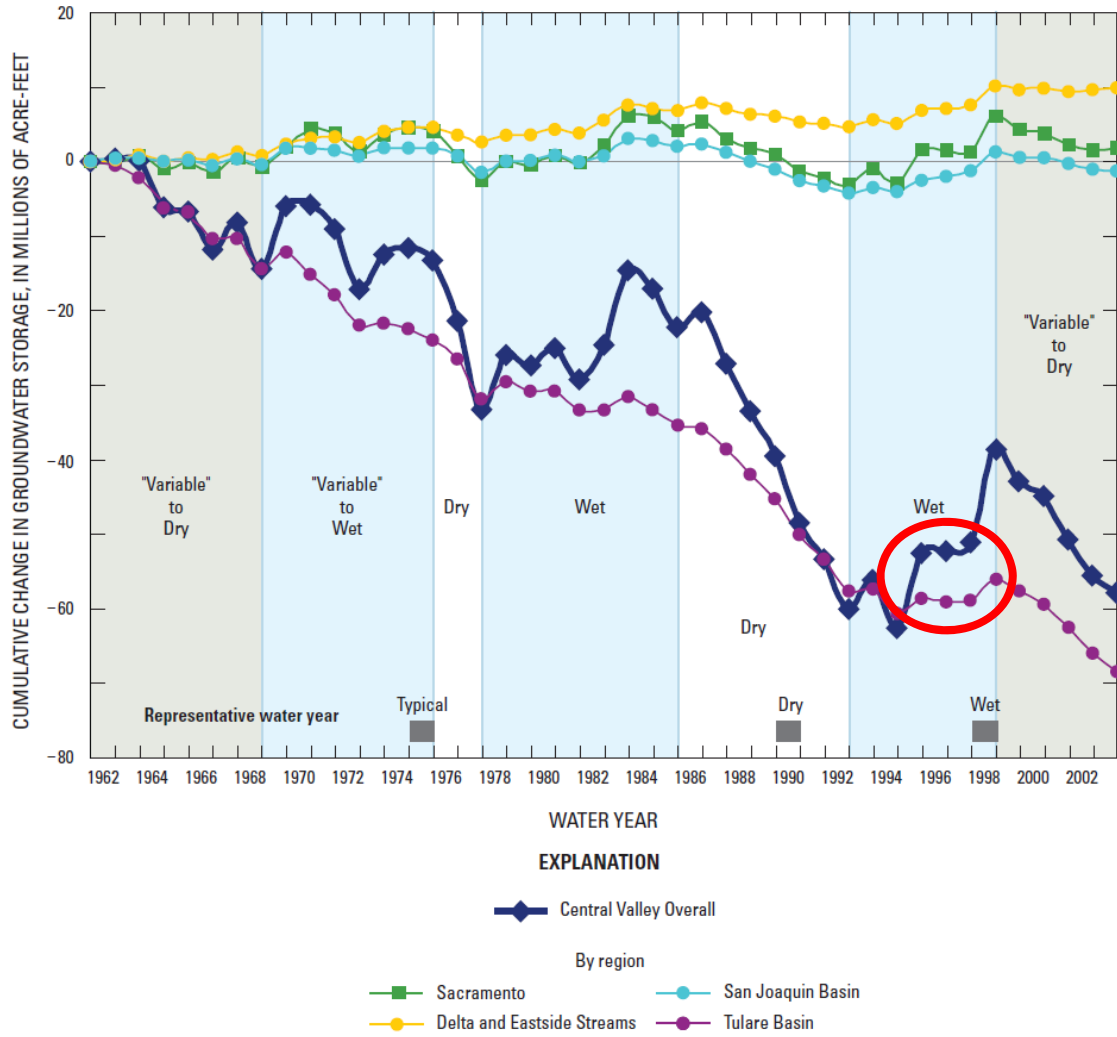
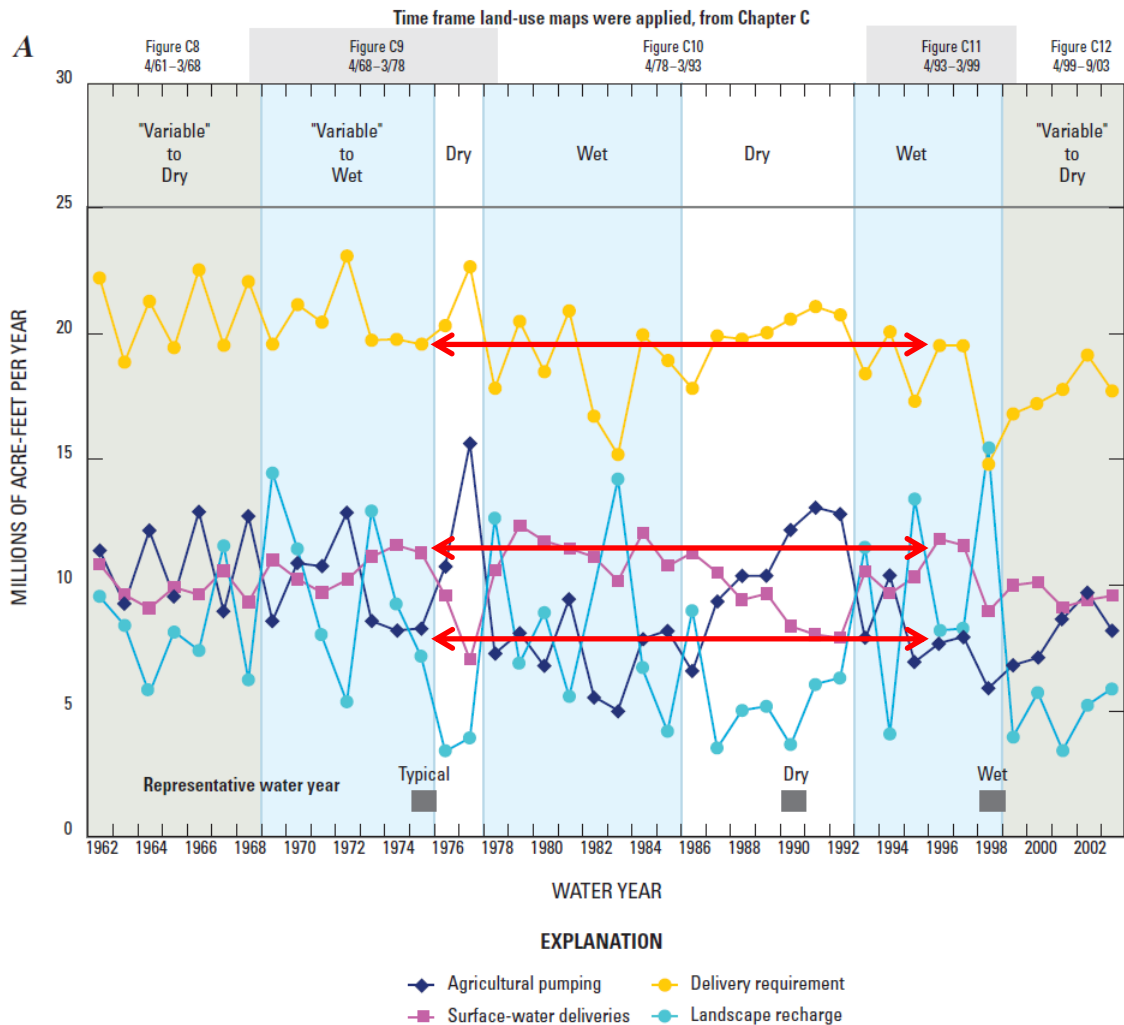


Figure 9. Simulated cumulative annual changes in aquifer storage (reprinted with permission from: Faunt 2009, p. 77, Figure B9.). Red circled area indicates the years chosen to represent steady-state stress conditions.



**Figure 10. Water budget of CVHM, where “delivery requirement” is the irrigation water requirement from both groundwater and surface water sources. (Reprinted with permission from: Faunt 2009, p. 73, Figure B6.)**

For the simulation we chose the water year spanning Oct. 1996 – Sep. 1997 as the stresses remain nearly constant compared to the previous year.

However, the CVHM model is a transient state model with a monthly step, where the head distribution, groundwater recharge, and groundwater pumping, vary over the year. To obtain a steady head field we average the monthly rates for the water year 1996. The mean hydraulic head relative to mean sea level is shown in Figure 11. The heads vary between -10 to 150 m (-33 to 492 ft). The head field is one of the main drivers of the velocity field and how the contaminants are transported through the aquifer. Therefore an accurate representation of head is very important. Figure 12 shows the cumulative distribution of the discrepancy between the averaged head field and each monthly head field of the year 1996. The discrepancy between the transient simulated head values and averaged head field is less than 1 m for 80% of the head values and less than 2 m for 90%.

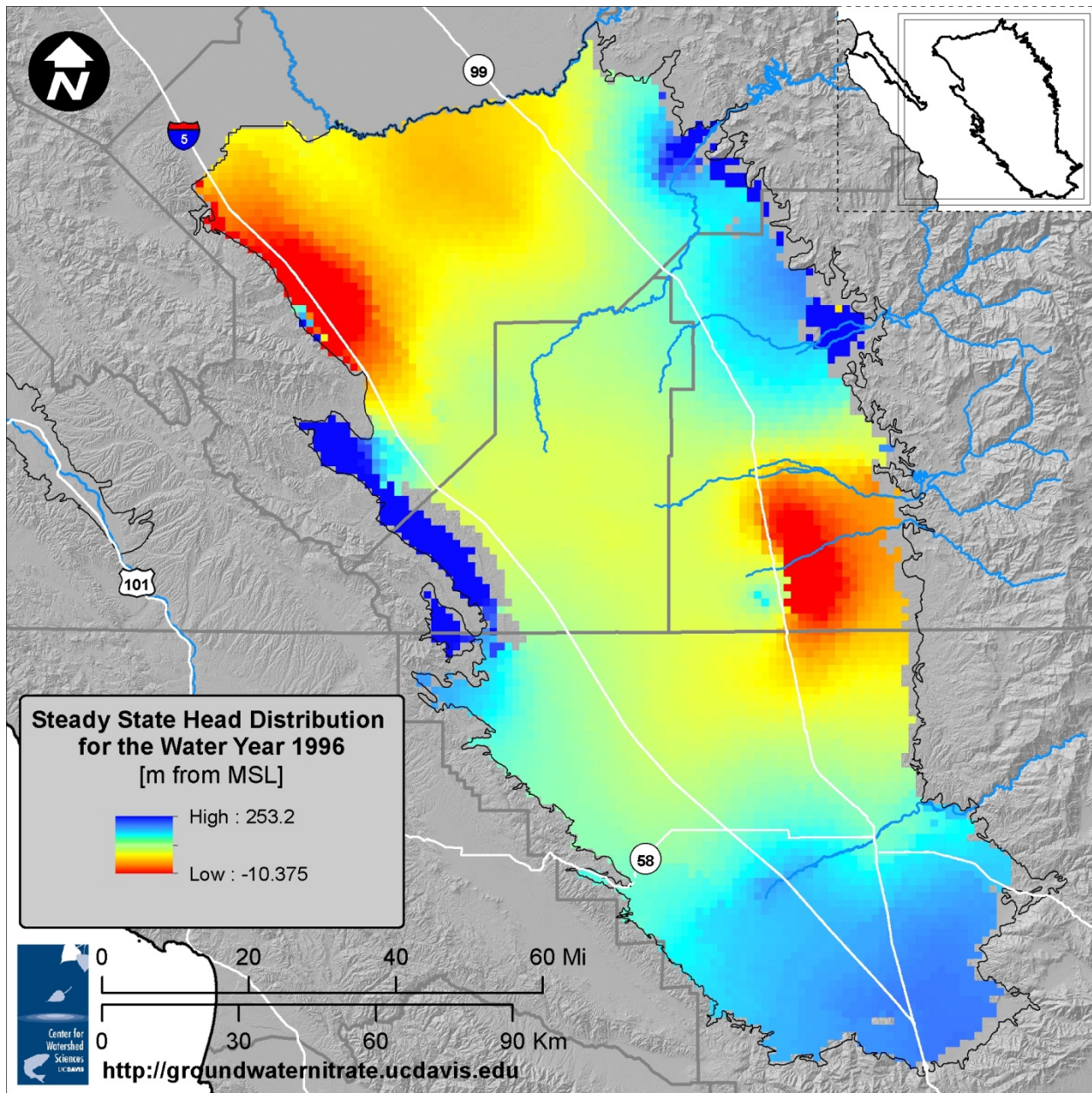


Figure 11. Steady state head distribution for the water year 1996.

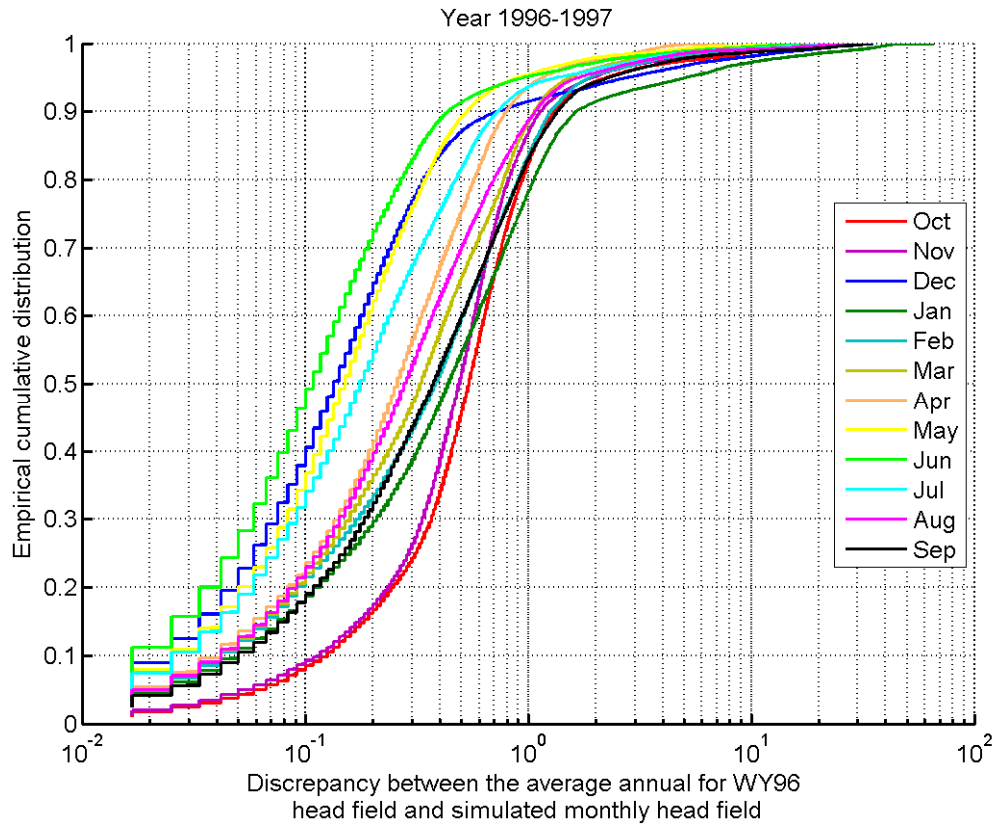
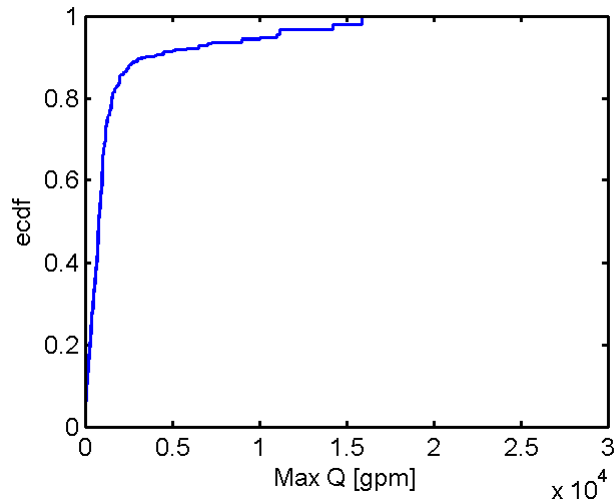


Figure 12. Comparison of averaged heads against the monthly heads used for averaging.

### 3.2 Conceptual Background

#### Well Generation Algorithm

The CVHM uses finite difference approximation with discretization of one square mile. Therefore various stresses such as groundwater recharge, groundwater pumping, and stream interactions, are assigned to the center of each cell, and the assigned values correspond to aggregation of all stresses located in each cell (e.g., the pumping rates of all the wells that are found in a square mile). To compute BTCs for wells with typical characteristics (i.e., pumping rates, well depths and screens that are closer to reality), in the refined model we developed an algorithm for generating wells with representative pumping rates, screen length, and depth. In fact the Well Generation Algorithm (WGA) is an automated way to distribute the well stresses back to individual wells. Since the location of the real wells is unknown, we use the WGA for generating random locations and random pumping rates, which satisfy the overall mass balance and honor the well characteristics, such as pumping rates, screen depth, and length typical of the study area. The input data for the WGA are the empirical distribution functions (ecdfs), which describe the well pumping rates, screen lengths and depths. The ecdfs used in this report are illustrated in Figure 13, Figure 14, and Figure 15.



**Figure 13. Empirical cumulative distribution function of maximum well pumping rate.**

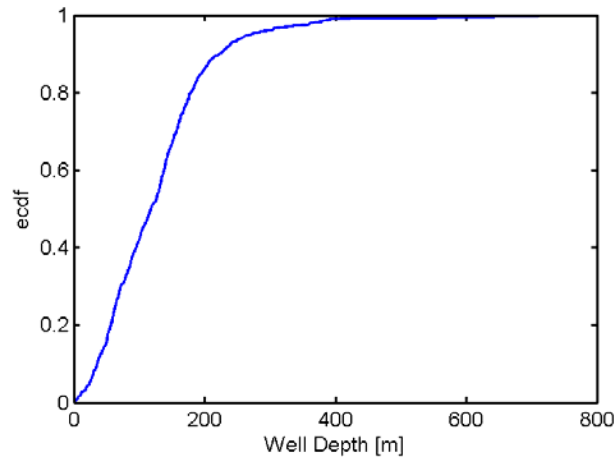


**Figure 14. Empirical cumulative distribution function of well depth [m] (distance between water table and bottom of the well screen).**

The ecdf of pumping rates is shown in Figure 13. Note that the data correspond to the maximum capacity of each well in the sample and not the actual pumping rate, which is unknown. In addition, note that most of the wells, if they operate at their maximum design capacity, they do so approximately 5 months per year (dry season) while during the remaining months, they either do not operate or operate at reduced rates. Based on expert opinion, it was suggested to sample from a subset of the full distribution, excluding the extremely large rates ( $>0.9$ ) or negligible rates ( $<0.05$ ). Note also that, in the simulation, we are interested in the yearly average rates, therefore the sampled rates were further reduced to correspond with yearly rates.

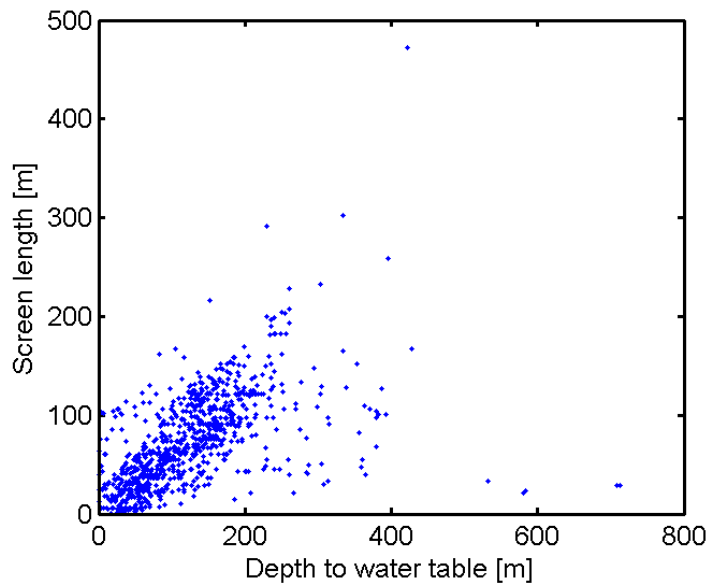


**Figure 15. Correlation between well depth and screen length.**

The steps of the WGA to generate locations and pumping rates are outlined as follows and explained in more detail below:

- I. Choose a cell with assigned pumping rate
  1. Generate a well location
  2. Generate pumping rate and keep track of cumulative pumping
  3. If cumulative pumping is less than the cell assigned pumping rate, repeat steps 1 and 2
  4. Else, subtract the difference from the nearest cell, and proceed to the next cell
- II. Generate random depth and screen length based on the distribution
- III. If the depth is greater than 100 m assign the depth to a well with large production rate
- IV. If the depth is less than 100 m assign the depth to any well
- V. Check that there is 3 m (10 ft) of screen for every 100 gpm in coarse material. If not repeat steps II-V.

According to the pseudocode for each cell (square mile) of the CVHM discretization with an assigned pumping rate, we randomly generate wells within the cell using the formula  $\mathbf{x} = \mathbf{x}^{min} + \mathbf{r}(\mathbf{x}^{max} - \mathbf{x}^{min})$  which generates uniformly distributed numbers within the specified limits (e.g., cell extent) where  $\mathbf{x} = [x, y]$  are the coordinates of the generated well and  $\mathbf{r}$  is a vector of two random numbers from the uniform distribution between 0 and 1. In addition, we specified a minimum threshold distance equal to 300 m, so that the wells are not in close proximity. The generation of the wells is a sequential process and each new well is accepted only if the distance with the closest existing well is greater than the threshold. To assign pumping rates, we sample randomly from a subset of the empirical cumulative

distribution function. When the cumulative pumping rate of the generated wells per cell exceeds the rate of the cell, which is specified by the CVHM, we proceed to the next cell. However, to maintain the water budget and at the same time to honor the pumping ecdf, the difference between the total cumulative pumping rate and the specified CVHM rate, is subtracted from the nearest cell to the last generated well in the current cell. Based on the above approach the number of wells per cell (i.e., wells per square mile) is dictated first by the cell pumping rate, (e.g., the higher the rate the more wells will be generated) and secondly by the shape of the ecdf.

In total, the algorithm generated 5,486 wells within the TLB study area. It can be seen (Figure 16) that the average number of wells per square mile is 4 while 80% of the simulated wells are found at a density less than or equal to 5 wells per square mile. This is also in agreement with reality, according to expert opinions. The simulated well locations are illustrated in Figure 17. The regional spatial distribution of the simulated wells is dictated by the parent model, here CVHM, and the CVHM pumping fluxes for the representative period chosen for the steady-state flow field (here: 1996). The WGA introduces an artificial variability at the scale of and within the CVHM grid cells. Due to the much finer discretization, the spatial local distribution of the wells obtained from WGA is therefore different and more detailed than with CVHM.

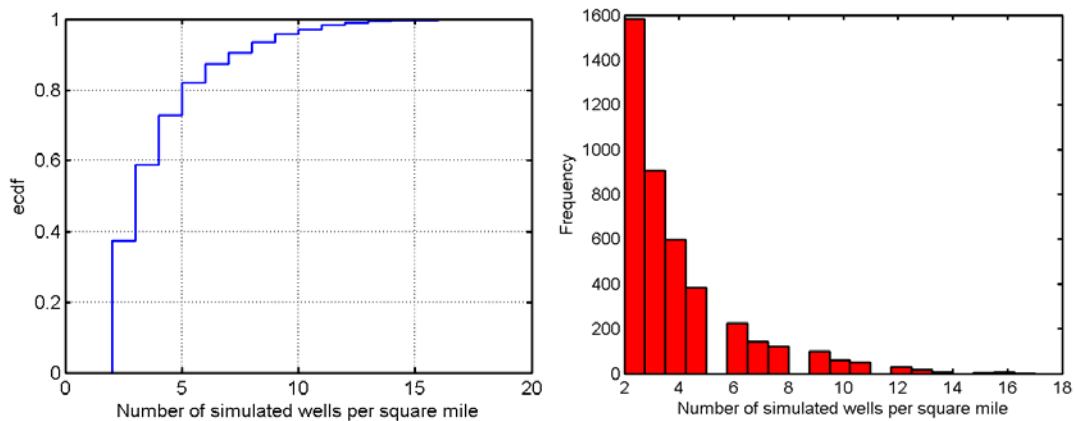


**Figure 16. Left) Empirical cumulative distribution function of the number of wells per square mile. Right) histogram of the number of simulated wells per square mile.**

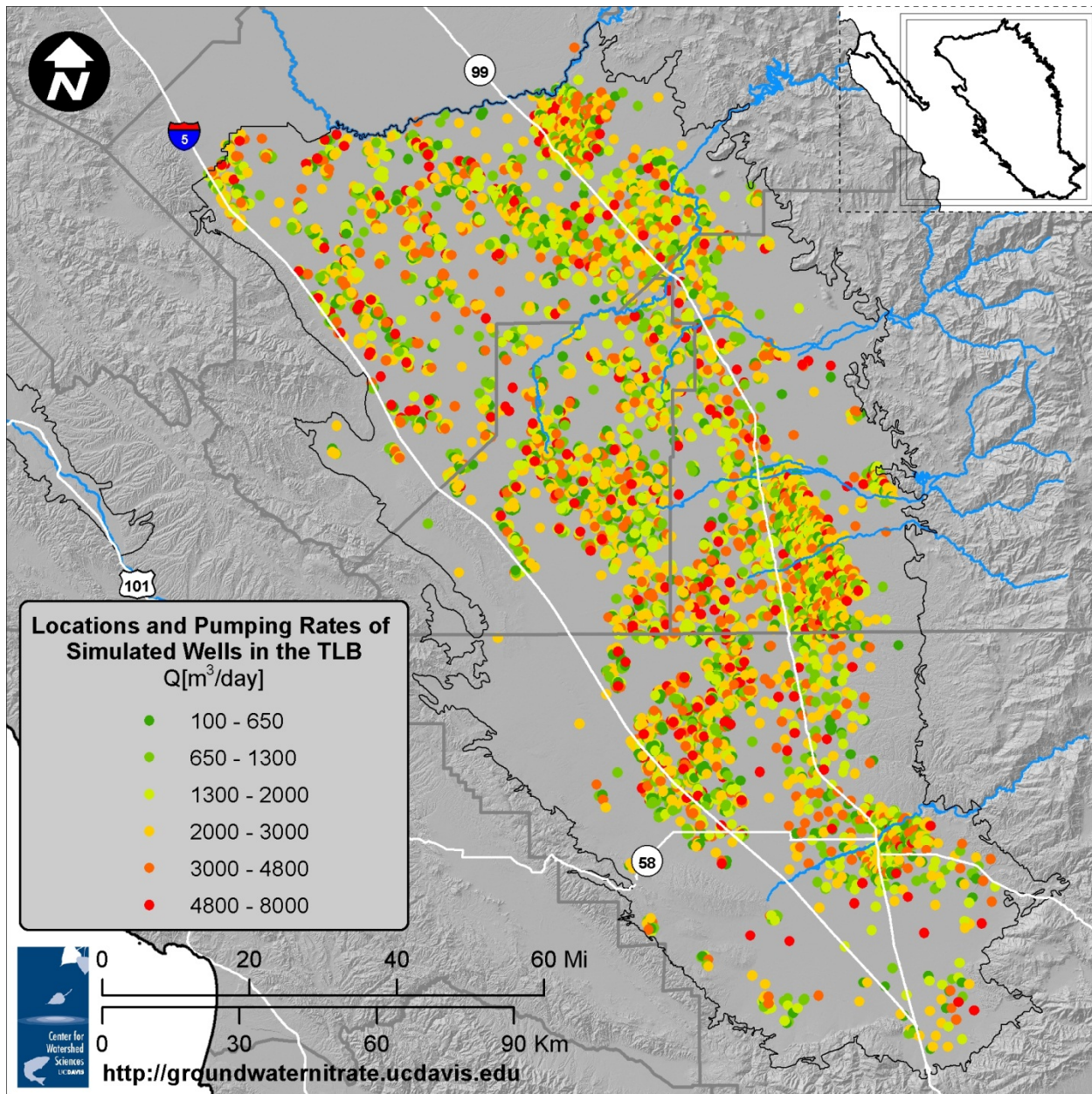


**Figure 17. Locations and pumping rates of simulated wells in the TLB study area.**

The distribution of pumping wells in Figure 85 reflects long-term average agricultural and urban water extractions, as represented by the year 1996 water budget (see discussion above and Figure 78). Under “normal year” conditions, surface water supplies along the easternmost portion of the TLB are sufficient to supply most irrigation water. Hence, most pumping wells in the easternmost part of the TLB are for urban uses (e.g., City of Fresno, City of Visalia, City of Porterville).

The distribution of pumping rates of the simulated wells is illustrated in Figure 18. Since we used a subset of the original distribution, the simulated distribution does not match the data, yet the median

value is approximately equal to 800 gpm, assuming a 5-month pumping period, which is a reasonable assumption for the particular study area.

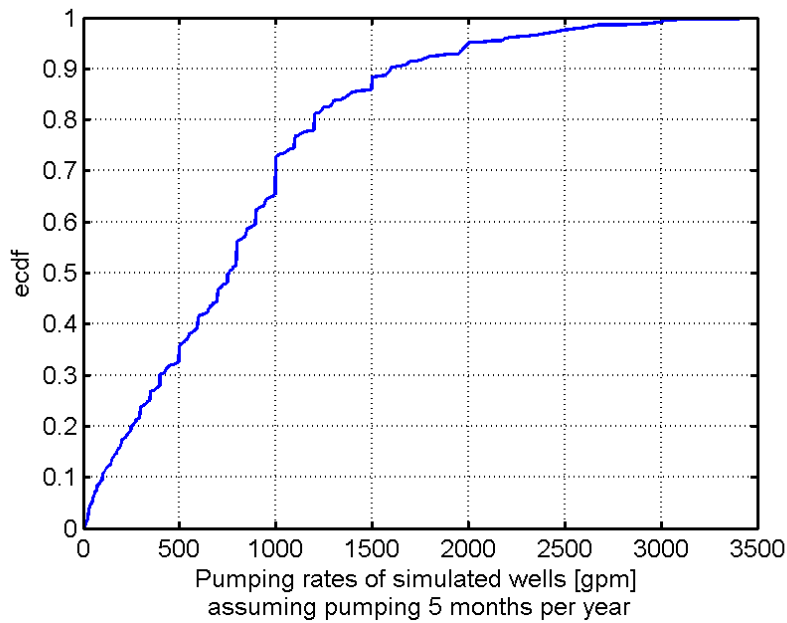


**Figure 18. Empirical cumulative distribution function of simulated pumping rates.**

After the generation of well locations and pumping rates, we assigned depth and screen lengths. Similarly the ecdf of well depths (Figure 14) and the correlation between screen lengths with depth (Figure 15) are used to generate random values. However special treatment is required to avoid assigning very large pumping rates to shallow wells. To do so we imposed a to sample from the upper half of the depth distribution when the pumping rate exceeds the median pumping rate of the pumping rate ecdf. However, when the rate is less than the median we use the full range of the distribution. In addition to pumping rate generation, special treatment is required for the screen length generation. Typically the shallow wells have shorter screen lengths than the deep wells. Figure 15 shows the depth of the well against the screen lengths. Ideally, an empirical bivariate probability density function is computed; however, this requires a large amount of data. Here we choose a two-step approach where, for each well, we first generate the depth and then the screen length. During the screen length generation, instead of sampling from the full distribution, we sample from a narrow range of the distribution. For example, suppose that  $d$  is the depth generated by sampling the depth distribution (Figure 14). To assign screen lengths we identify the samples with depth within the range  $[r - d, r + d]$ ; hence, we use only a limited number of samples instead of the full distribution and construct a local ecdf, which describes the distribution of the well screen lengths in the vicinity of the selected depth  $d$  (Figure 19). The range  $r$  depends on the density of sample points (wells) around  $d$  and it is determined in an automated fashion. For each well, the algorithm starts with a very small value for the range  $r$  and increases the range until a sufficient number of sample points are found to construct a local ecdf.

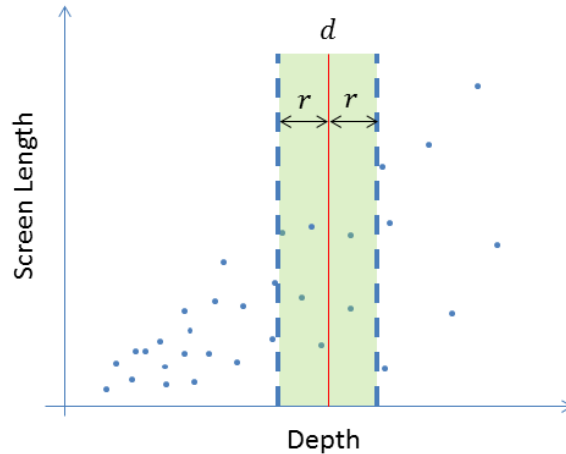


**Figure 19. Sampling range for screen length.**

Based on the depth and screen length distributions we assigned random well depths and screen lengths to the simulated wells that were generated in the previous step, according to their pumping rates. In order to generate an unbiased depth-screen length distribution, first we split the simulated wells into two groups. One group includes all the wells with simulated pumping rates greater than the median (i.e., 800 gpm), while the second group actually contains all the wells. Then we generate random depth  $d$  and random screen length based on the ecdfs. If the generated depth  $d$  is greater than 100 m (328 ft) then the well is designated as deep and the depth is assigned randomly to one of the wells that belongs to the first subgroup (of large production wells) and the well is removed from both sets. If the generated depth is less than 100 m then the pair of depth-screen length is assigned arbitrarily to one of the wells of the second group which contains all the wells. It can be seen that it is possible for wells with relatively small pumping rates to have large screen lengths, yet the suggested approach does not allow large wells to have small screen lengths. At the same time, since all the distributions are sampled independently, we avoid introducing bias. This becomes apparent by comparing Figure 14, which shows the ecdf of depths based on the real data and Figure 20 that shows the ecdf of the simulated well depths. The correlation between well depth and screen length is illustrated in Figure 21, which is very similar to the correlation of the real data (Figure 15). Last, we check if the material between the screen lengths can support the assigned pumping rate. We utilized an empirical formula where, for each 100 gpm we require at least 3 m (10 ft) of coarse material (e.g.,  $K > 10$  m/day (33 ft/day)). If the well does not meet this restriction, we repeat the depth and screen length generation.

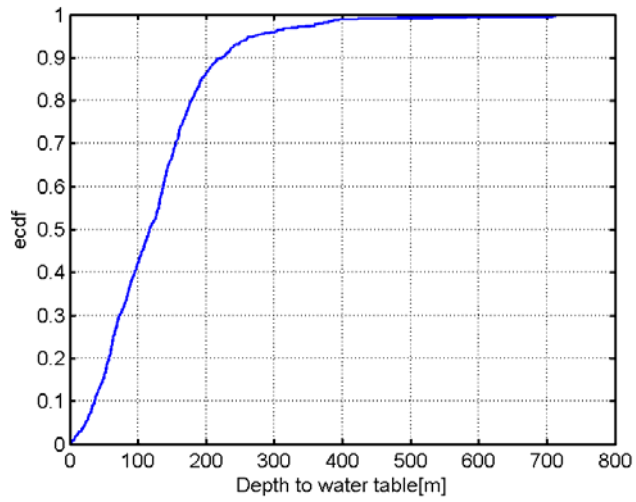


**Figure 20. Empirical cumulative distribution function of Simulated well depth (distance between simulated water table and bottom of the well).**

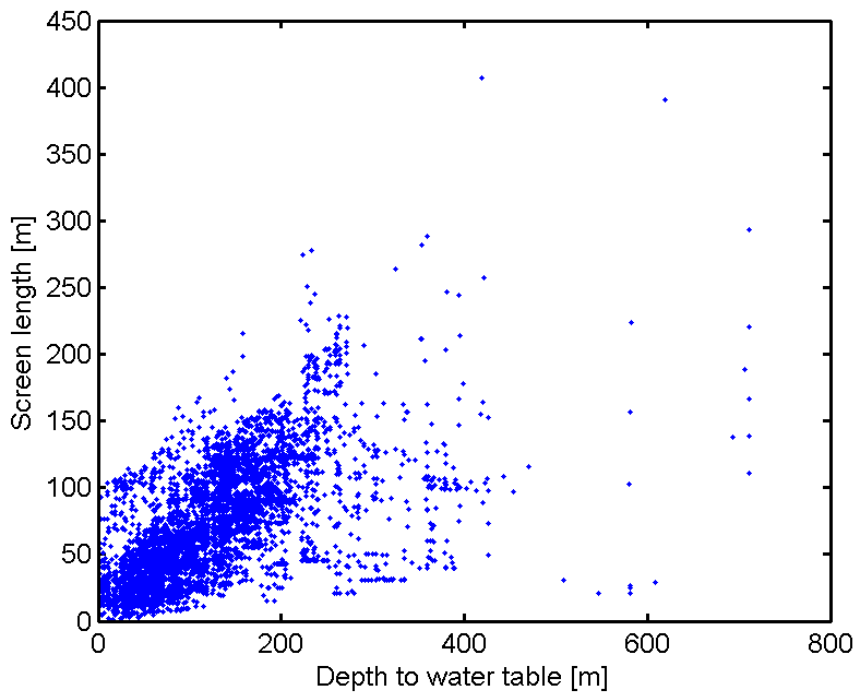


**Figure 21. Correlation between simulated well depths and screen lengths.**

### ***3.3 Groundwater and Transport Simulation***

After the generation of wells, all the additional stresses, which were defined as monthly rates, such as groundwater recharge stream leakage interactions, were averaged to obtain representative yearly rates. The hydraulic conductivity values and the ratios between horizontal and vertical conductivities were obtained from the input files of CVHM model.

To simulate the steady state flow field that corresponds to the water year 1996, we use finite element discretization, where the discretization varies from few meters ~10 m (33 ft) near wells to several hundred meters. Figure 22 illustrates an example of the fine discretization that was used in the steady state solution. The red cells correspond to the cells of the CVHM (i.e., each cell is 2.6 km (1 sq.mi)). For the vertical discretization we used 25 layers as opposed to the 10 layers used in CVHM.

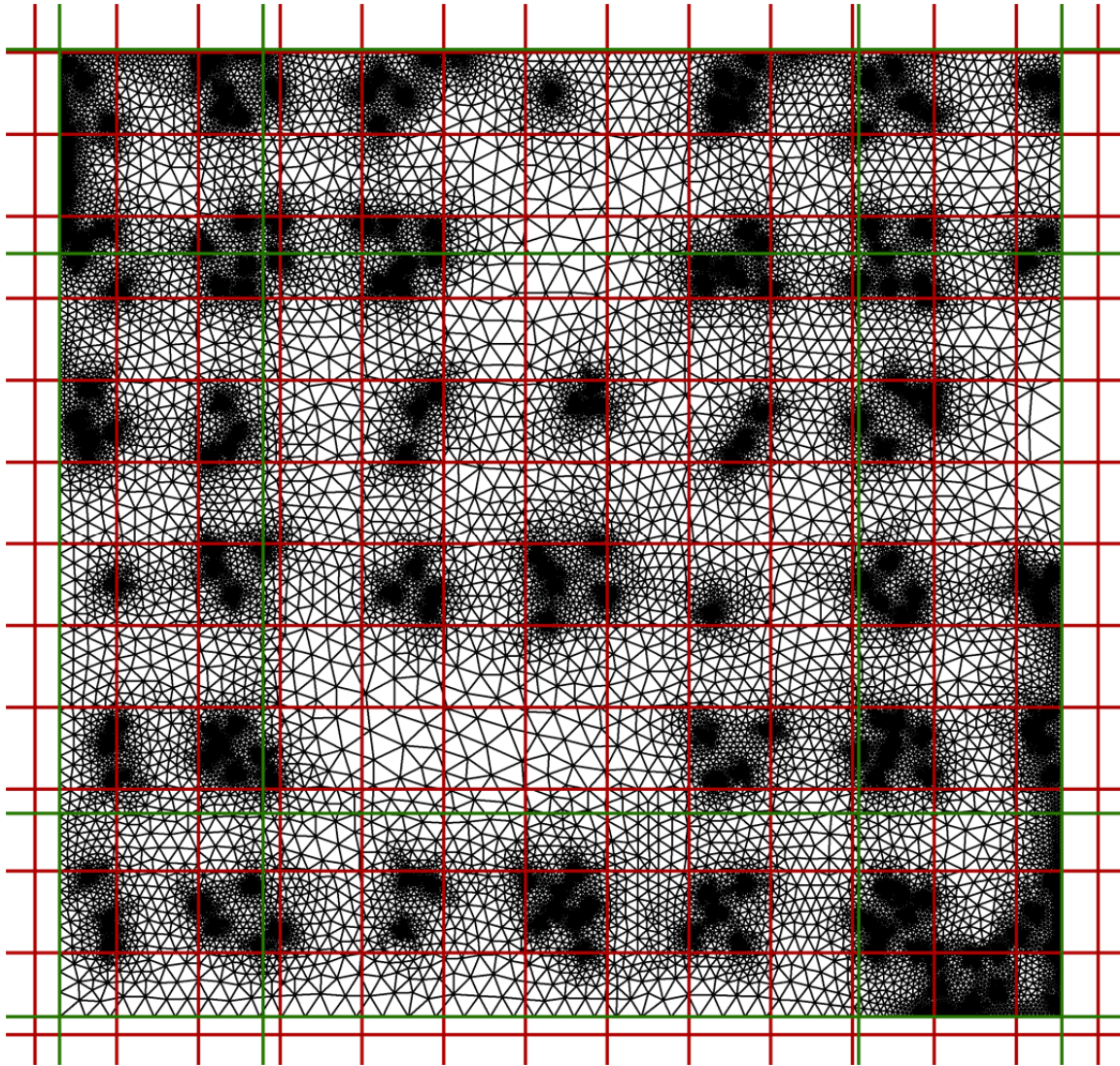


**Figure 22. Discretization based on finite elements. The red lines correspond to the cells of the CVHM model. The dense black areas indicate the highly detailed discretization around the wells.**

To obtain a steady state solution at this level of discretization, we employed the simplistic domain decomposition method presented above. According to the method, the domain was first divided into overlapping subdomains. Figure 24 shows the division of the study area into overlapping subdomains. In total, the subdomain was divided into 97 overlapping subdomains. The dimension of each subdomain was approximately 20 x 20 km., while the width of the overlapping zone was constant and equal to 2 km.

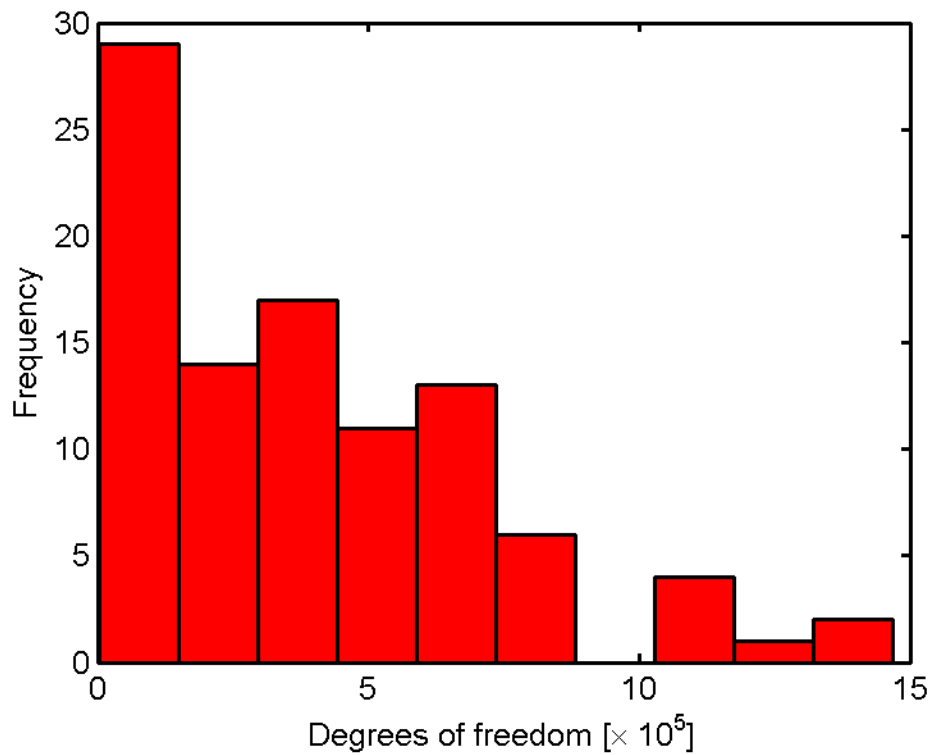


**Figure 23. Histogram of degrees of freedom for the simulated subdomains.**

The degrees of freedom for each subdomain vary from  $3.1 \times 10^3$  to  $14.8 \times 10^5$  (Figure 23). The total number degrees of freedom is  $39 \times 10^5$ . Note that in our approach the meshes of adjacent subdomains were not conforming (i.e., within the overlapping zone the nodes of two subdomains do not coincide). According to the simplistic domain decomposition method, each subdomain was solved independently. The boundary conditions for the inner boundaries of each subdomain were interpolated from the coarse solution of CVHM. To obtain a divergent free velocity field we used the proposed (section 7.2.2) weighted averaging scheme.

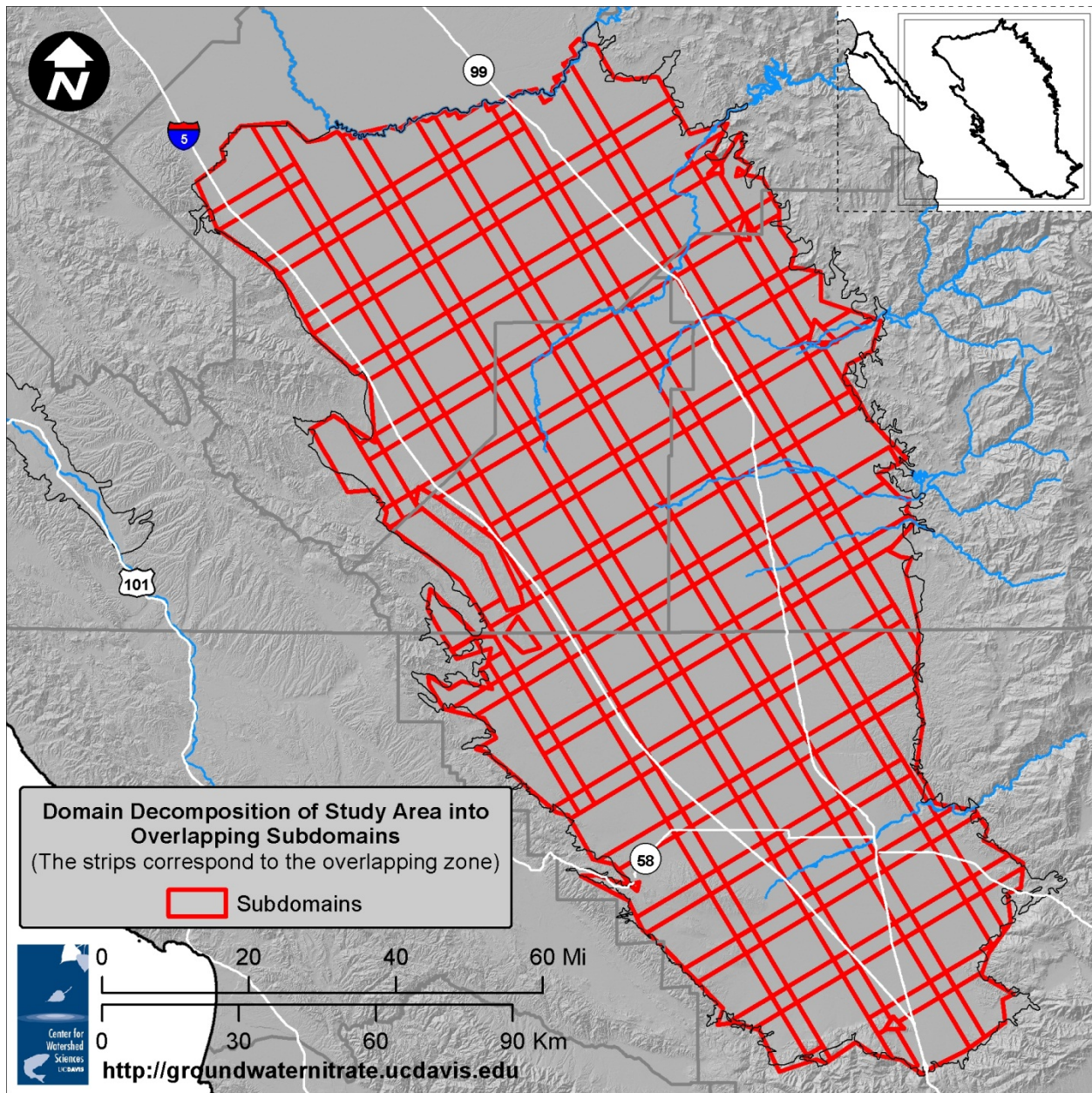


**Figure 24. Domain decomposition of study area into overlapping subdomains. The strips correspond to the overlapping zone.**

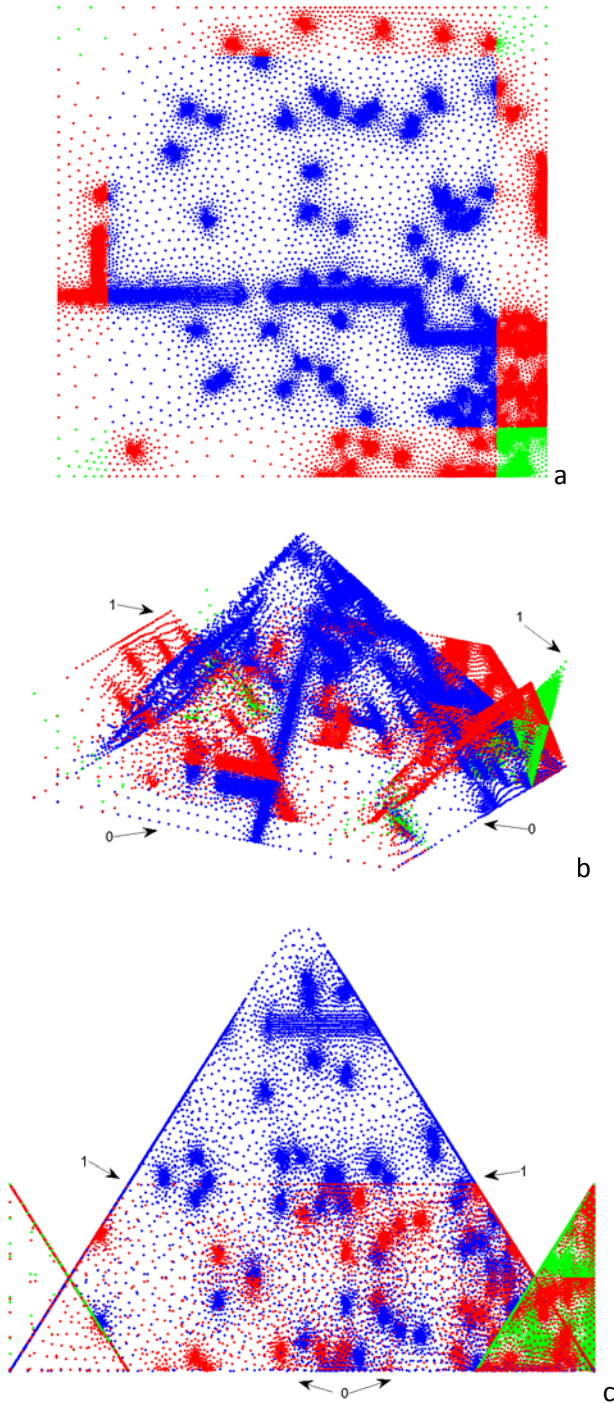


**Figure 25. Illustration of weighting scheme between adjacent subdomains.**

The hydraulic heads for the nodes within the non-overlapping area were obtained directly from the head solution of each subdomain. For the nodes in the overlapping zones, first, we computed the weights associated with each subdomain and then the node heads were calculated as the weighted

average. Figure 25a illustrates the nodes of one of the subdomains. To keep the figure simple the triangularization has been removed from the figure. The blue dots in Figure 25a correspond to the nodes within the non-overlapping area. The nodes with red correspond to the overlapping zone between 2 subdomains and the green to the overlapping -zone between 4 subdomains. In the other two panels, Figure 25b and Figure 25c, the height of each node corresponds to the weight associated with each subdomain. It can be seen that the weight of the main subdomain (blue dots) is zero at the boundaries and increases linearly. Similarly, the weights of the adjacent subdomains are zero at their boundaries and increase linearly as well (see red and green dots). The final head field is the weighted average of the subdomain head distribution. For example, the heads of the main subdomain (blue dots) of Figure 25 at the boundaries will be given zero weight, since the error is expected to be large due to the interpolated (from the coarse solution) boundary constraints. As we move towards to the center of the main subdomain (blue dots) the velocity obtained from the main subdomain will be given higher weight, while the weight from the adjacent subdomains decreases. Hence, the overlapping zone creates a smooth transition zone between subdomains

The head and subsequently the velocity field were used for particle tracking. According to the methodology, for each well we released 100 particles, uniformly distributed, around the well screen and tracked backwards until they exit the aquifer. Since the number of wells is 5,486, the simulated streamlines equal to 548,600 (Figure 26).

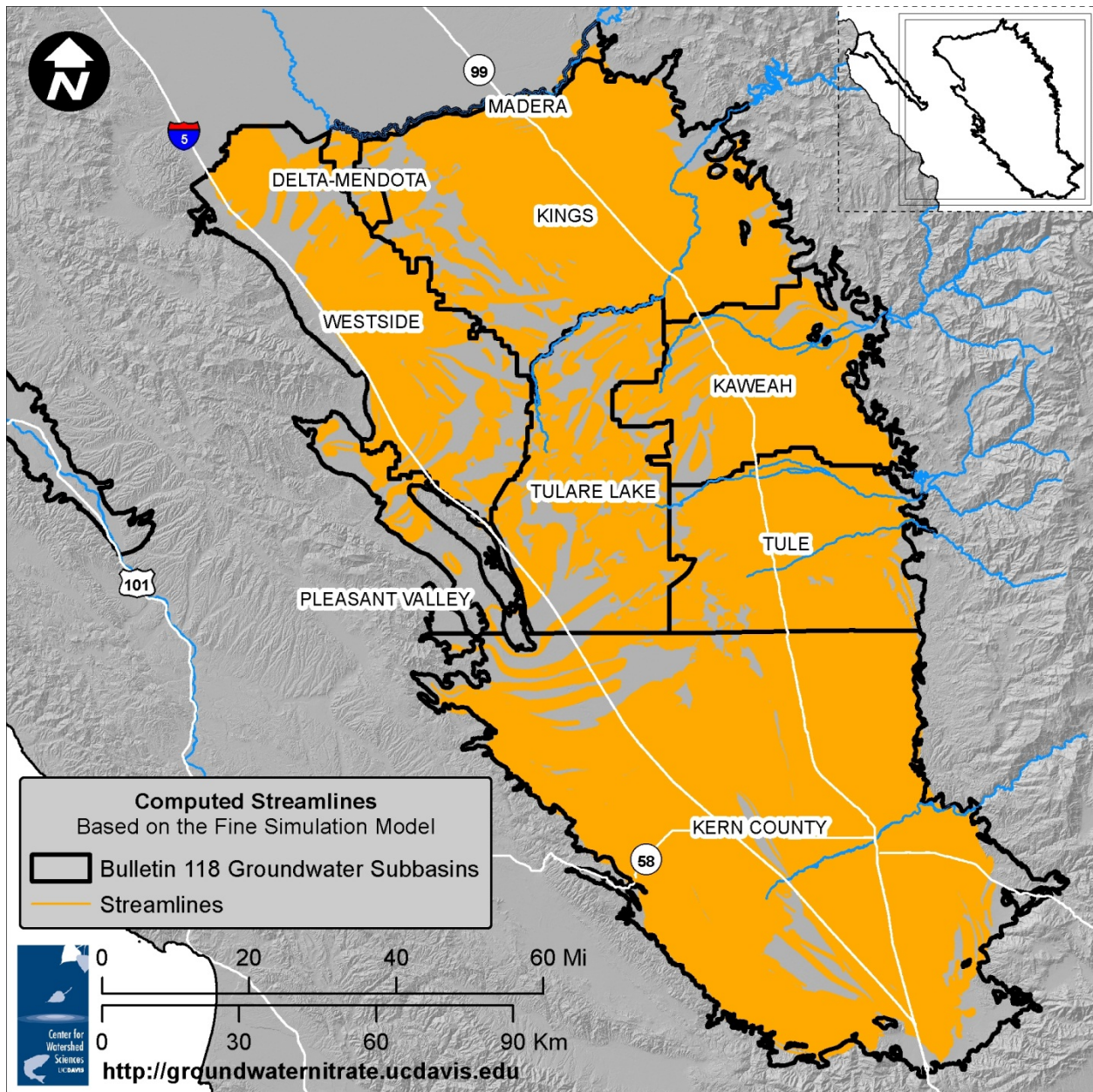


**Figure 26. Computed streamlines based on the fine simulation model.**

Then, for each streamline the 1D ADE transport problem was solved to obtain unit response functions. Here we used the analytical solution of 1D ADE where the longitudinal dispersivity was a function of streamline length and the velocity was set equal to the advective velocity. Note that, during the 1D transport problem, we assumed unit input loading to obtain a unit response function for each streamline, which was subsequently stored into a GIS database and was used for predictions based on different loading scenarios. Figure 27 illustrates the computed URFs for two of the simulated wells. We choose one shallow and one deep well to point out the different responses one should expect. It can be

seen that the travel time distributions for shallow wells are shorter between few years and few decades, as opposed to deep wells where the range of travel time distribution spans from several decades to centuries. In addition, the shape of the URF for shallow wells is spiky, indicating that shallow wells exhibit greater concentrations compared to deep wells.

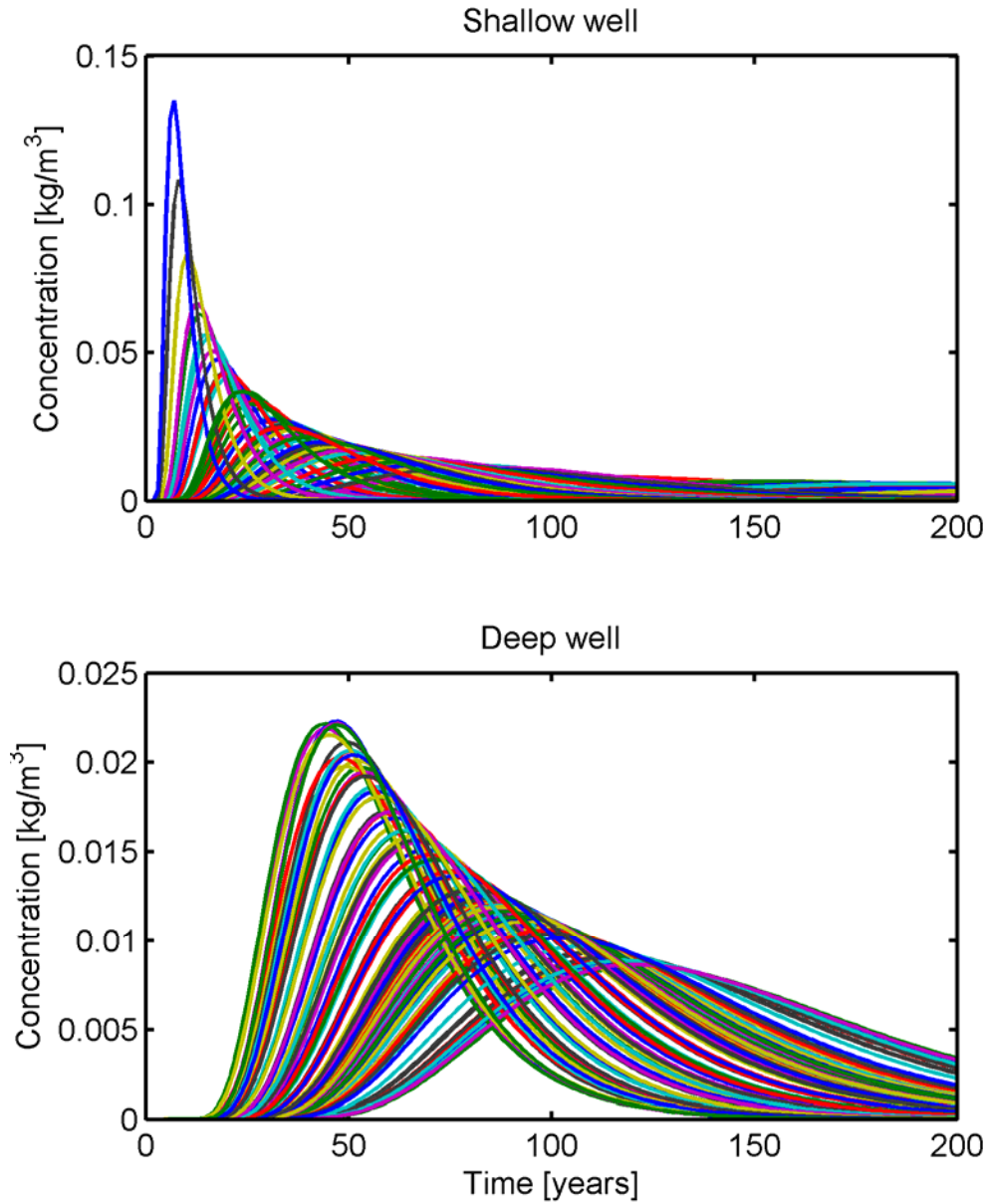


**Figure 27. Unit Response Functions.**

## 4. NPSAT Implementation Based on Coarse Model

---

In addition to the highly detailed model, we applied the NPSAT using the CVHM coarse approximation. Similar to the detailed simulation, to obtain an average steady state flow field for the water year 1996, we averaged the monthly flow fields which were obtained from the output of CVHM. Based on analytical particle tracking (Pollock, 1994), we perform backward particle tracking until the particles exit from the water table. The particle starting points are identical to those used in the detailed model. Yet, due to coarse approximation, there is no cone of depression around each simulated well, resulting in an unrealistic shape of streamlines around the wells, which can be seen locally (Figure 30).

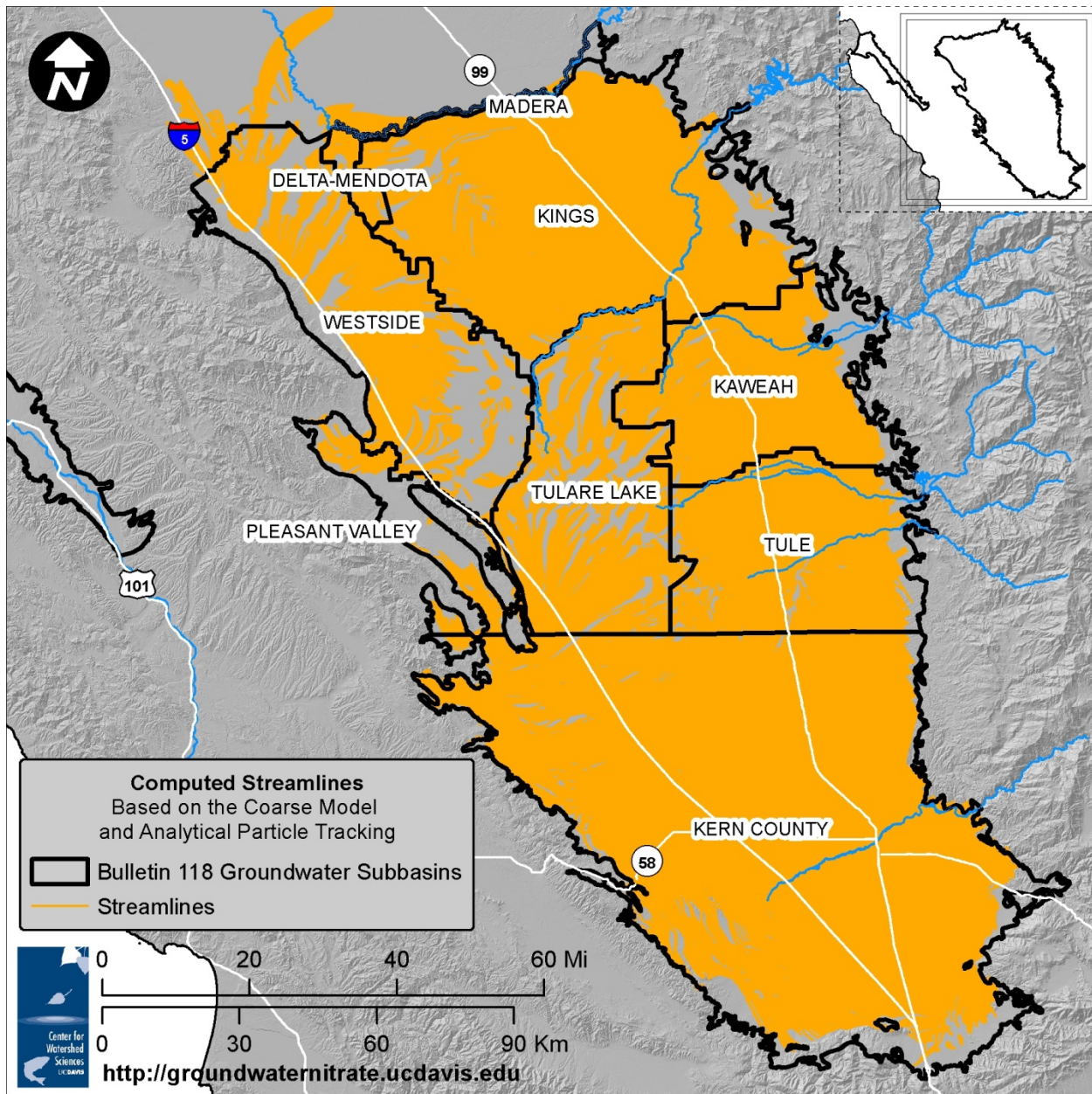


**Figure 28. Streamlines based on coarse model and analytical particle tracking.**

The streamlines based on the coarse approximation are shown in Figure 28. It can be seen that, in general, the streamlines follow the same pattern as in the highly detailed simulation. In both cases the streamlines cover the study area and in both cases there are fewer streamlines in the basins of Tulare Lake and Westside compared to the other basins. This can be attributed to the fact that there are fewer wells, but also that the particle travel distance is shorter in some cases.

Although the average shape of streamlines seems similar in both cases, the statistics of the streamlines reveal significant differences (Figure 97). One of the major differences is the distribution of

the streamline length. In the coarse approximation the logarithm of streamline length appears normally distributed with a mean value of about 15,000 m (15 km), while for the highly detailed simulation, the distribution exhibits two peaks, one close to 6,000 m (6 km) and one close to a few hundred meters. The significant difference in streamline length is reflected also in the age distributions. While the logarithm of age appears normally distributed, the mean value for the detailed model is approximately 1.8 (~65 years), but it is 2.1 (120 years) for the coarse model. In addition there is a significant percentage of streamlines in the detailed model with travel time less than a year.

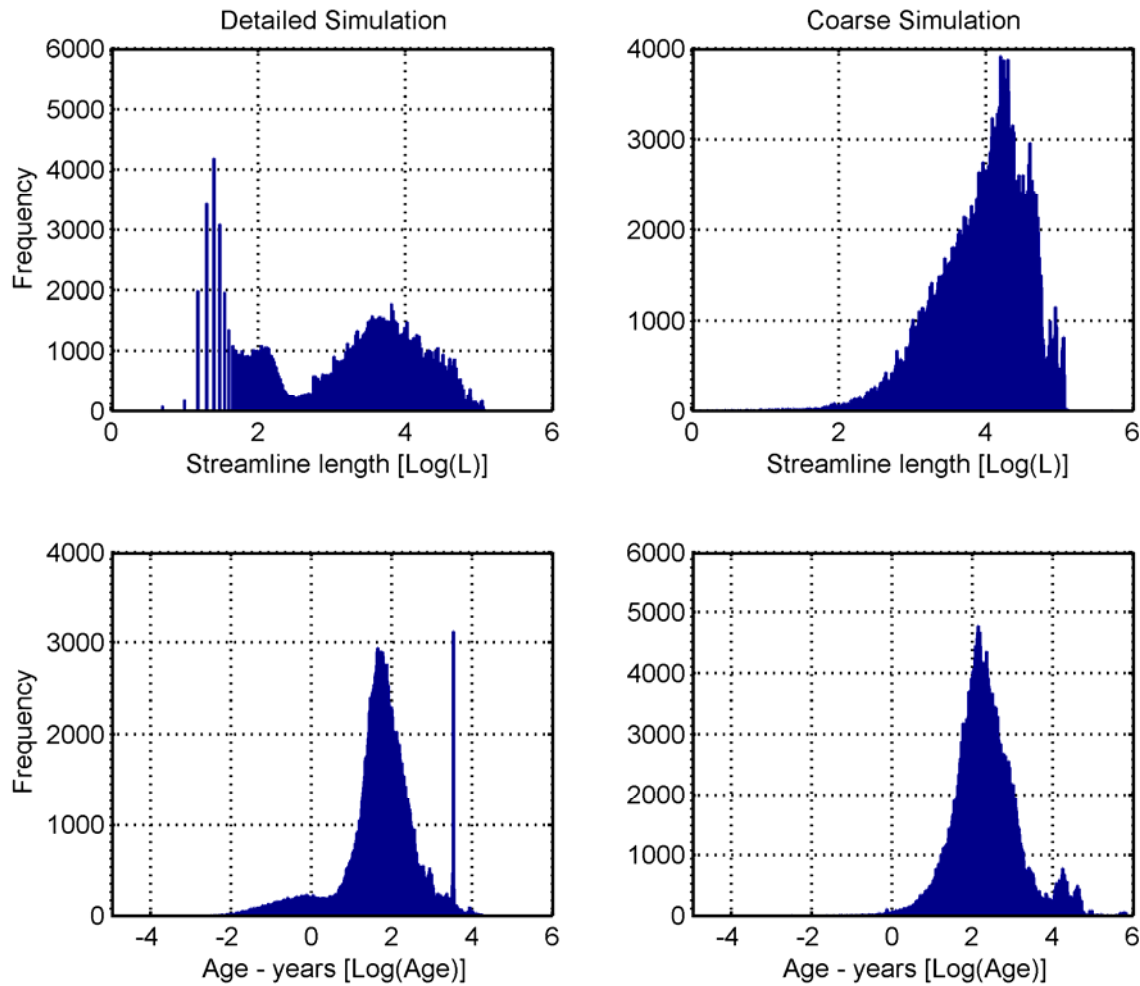


**Figure 29. Comparison of the distribution of streamline length [m] and age [years] between the two simulation models. A log of 0, 1, 2, 3, and 4 corresponds to 1, 10, 100, 1000, and 10,000 units (m or years), respectively.**

One of the main reasons for these differences is the fact that, in the highly detailed simulation, the hydraulic head field was depressed around the wells, due to fine discretization. Note that in coarse simulation the local cone of depression around the simulated wells was absent. Although in both models the particles originated from the exact same positions, in the fine model the particles are actually closer to the water table, due to the cone of depression, which was absent in the coarse mode. Therefore for

the fine model the particle's travel time to exit the aquifer was shorter compared to the coarse model, as well as the length of their streamline. In addition, it was not unusual that part of the screen length was above the water table and the particles above the water table in the detailed model were ignored. To illustrate the difference we have plotted the streamlines for one of the wells (Figure 30 top panel) and zoomed around the well (bottom panels). The blue lines correspond to the coarse model and the red to the highly detailed. The streamlines shown here were selected as representative. Indeed, in most cases the streamlines based on the coarse model were longer and narrower compared to the detailed model, due mainly to the absence of a cone of depression around the well.

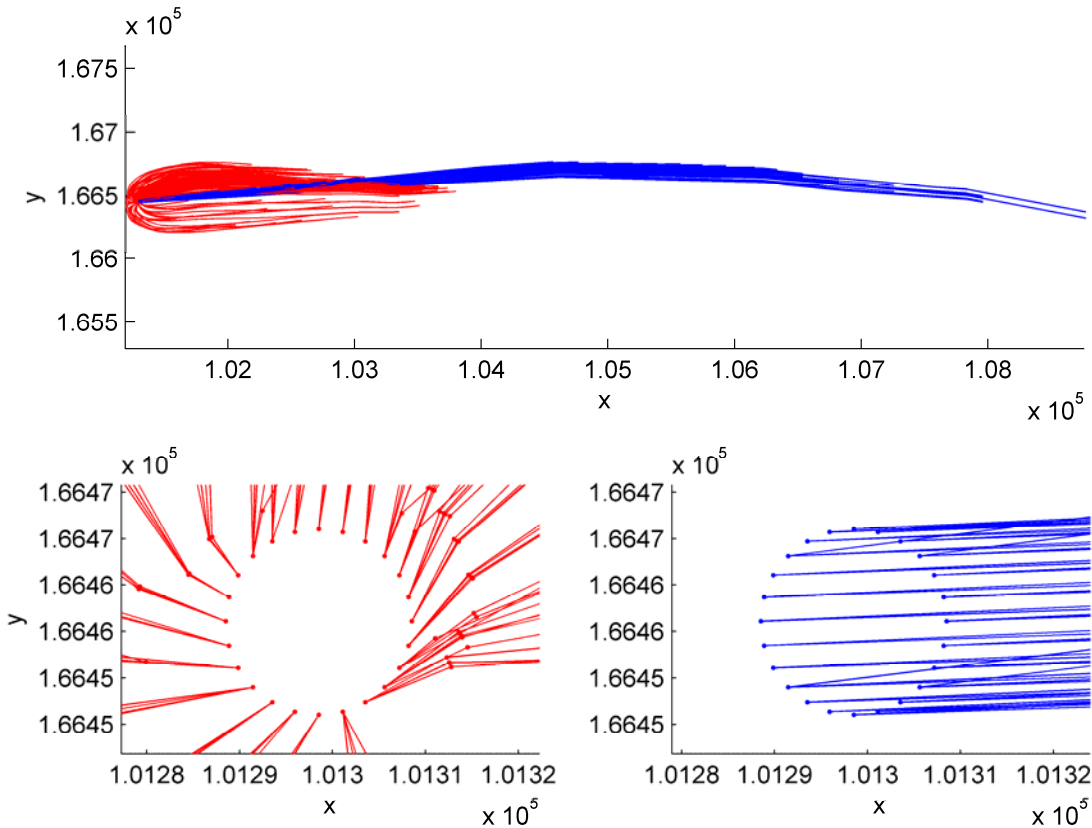


**Figure 30. Comparison between streamlines computed with the detailed and coarse model. Red streamlines correspond to detailed model and blue to coarse model. Top panel shows the overall streamline shapes of the 100 streamlines for a particular well. The bottom panels show the orbits of particles around the wells. Due to the absence of a cone of depression on the coarse model (blue lines) the streamlines are actually straight lines.**

## 5. Results

---

### 5.1 Nitrogen Loading Scenarios

The computed Unit Response Functions (URFs) can be rapidly convoluted with alternative loading scenarios to calculate real breakthrough curves for each well. In this report we examined the impact of four alternative nitrogen loading scenarios. A detailed description of the development of N loading scenarios is discussed in Section 1.8 of Technical Report 2 (Viers et al., 2012). Briefly, the four scenarios represent different management of excess manure N (nitrogen) exported from dairies after 1980: In Scenario A, exported manure N either leaves the study area or is incorporated into nutrient management on non-dairy crops such the typical amount of N applied to crops does not change. In scenario B (by study area) and C (by study area), half and all of exported manure, respectively, is applied to non-dairy cropland across the study area as an amendment in addition to typically applied fertilizer N resulting in higher groundwater nitrate loading. In scenario D, all manure N is applied on manured crops within dairies resulting in very high nitrate loading to groundwater on dairies, but elsewhere identical to Scenario A. The approach taken to modeling manure applications is also used to model food processing waste application, and application of biosolids and WWTP effluent nitrogen, whether it is to cropland or directly into recharge facilities.

The output of the N loading algorithm developed by Viers et al. (2012) is four alternative scenarios of the N leaching into into the groundwater table. The leaching rates are given in kg/ha for 8 different years (1945, 1960, 1975, 1990, 2005, 2020, 2035, and 2050). For the simulation purposes we assumed that the recharge is constant over the 106 years of simulation, while the nitrate leaching rates vary linearly between these yearly values. Groundwater water recharge is a very important parameter, not only due to its influence on the flow field, but also because it determines the final leaching concentration rates. The loading histories need to be converted in units  $\text{kg}/\text{m}^3$  (i.e., concentration). Therefore, prior to convolution of loading functions with the URF, we divided the N rates with the recharge. Figure 31 shows the cumulative distribution of loading rates assigned to each streamline. The left panels shows the N loading leaching rates in kg/ha (e.g., as they were computed by the N loading algorithm), while the right panels show the actual concentration that is assigned as input to each streamline. Note that this plot takes into account the loading rates for each streamline. Therefore, when multiple streamlines originate from the same land parcel, the corresponding rate is counted multiple times. During the prediction phase this does not affect the outcome as the final breakthrough curve is the weighted average of the streamline BTC (eqn. 21)

Similarly, in Figure 32 we plotted the exceedance probabilities of half the MCL, the MCL, and twice the MCL, that is the probability that wells exceed half the MCL, the MCL, or twice the MCL. Note that these three concentration limits will serve as reference values in the prediction phase. It can be seen that, in year 1945, approximately 40% of streamlines (i.e., 40% of the whole well source area) were

associated with land parcels that leach with rates of half of the MCL, while 20% and 13% exceed the MCL and twice the MCL, respectively. Having these conditions as starting points, loading increases somewhat linearly until the year 2005, where 83%, 68% and 55% of the streamlines are associated with land parcels that exceed the 22.5 mg/L, 45mg/L and 90 mg/L, respectively. For future predictions, four different loading scenarios are considered (see details in Section 1.8 of Technical Report 2, Viers et al., 2012). Outside of dairies, there is no difference in N loading to groundwater between “Scenario A” and “Scenario D” as manure exports either don’t affect typical N application or there are no manure exports to areas outside dairies. Post-1990, these two scenarios represent significantly less loading than “scenario B (study area)” and “scenario C (study area)”, which apply half and all exported manure to cropland, respectively, in addition to typical fertilizer applications. No manure exports occur in 1975 and prior to 1975 in any of these scenarios. Hence the loading distribution across the landscape is identical between the scenarios for 1945 – 1975.

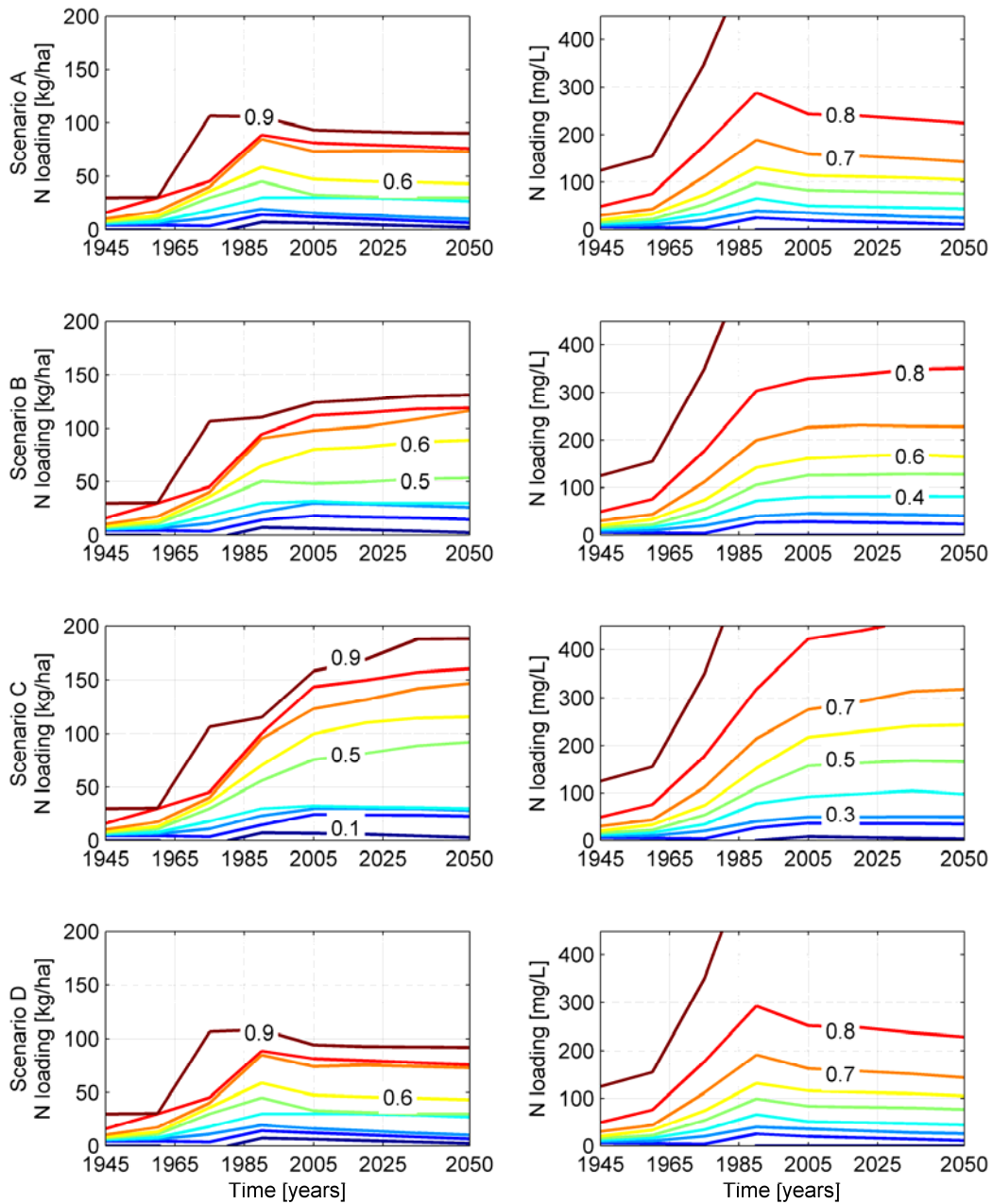


**Figure 31. Cumulative probability distribution of N loading per year assigned to each streamline. The left panels correspond to N loading with units kg/ha -output of N loading algorithm Technical Report 2 (Viers et al., 2012), while the right panels correspond to the actual loading of N as nitrate (45 mg/L drinking water limit), which is**

used as input to NPSAT simulation model. All scenarios here are “by study area” and are explained in Section 1.8 of Technical Report 2 (Viers et al., 2012).

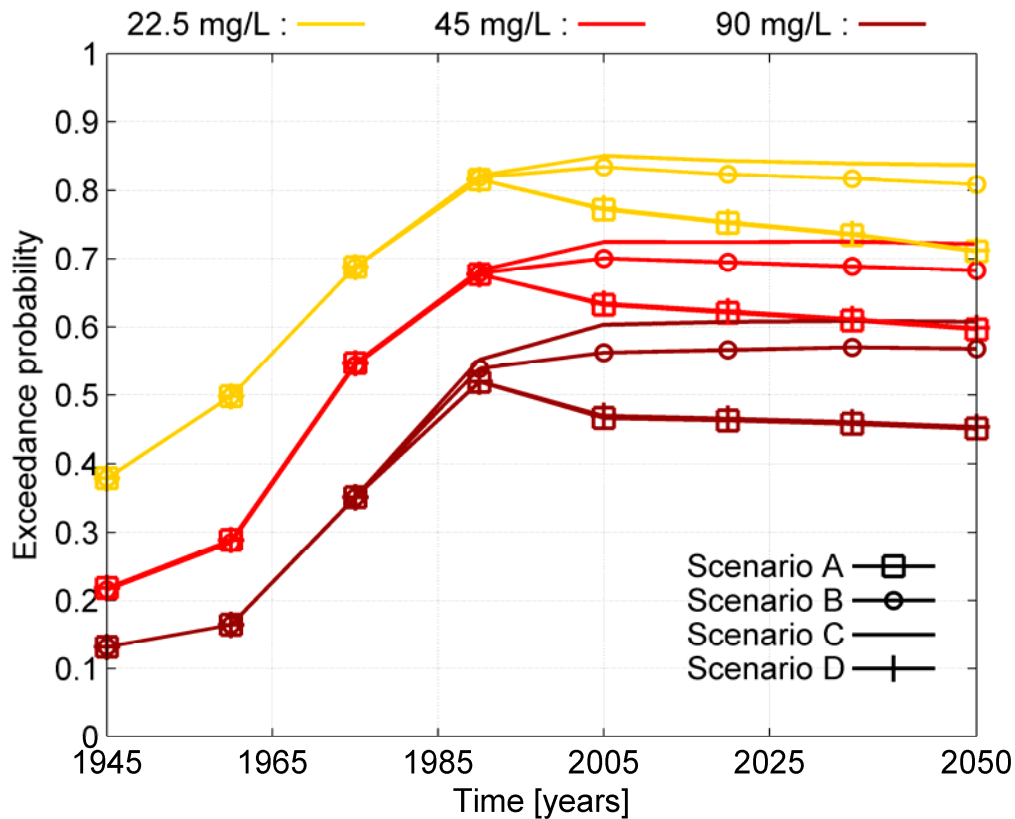
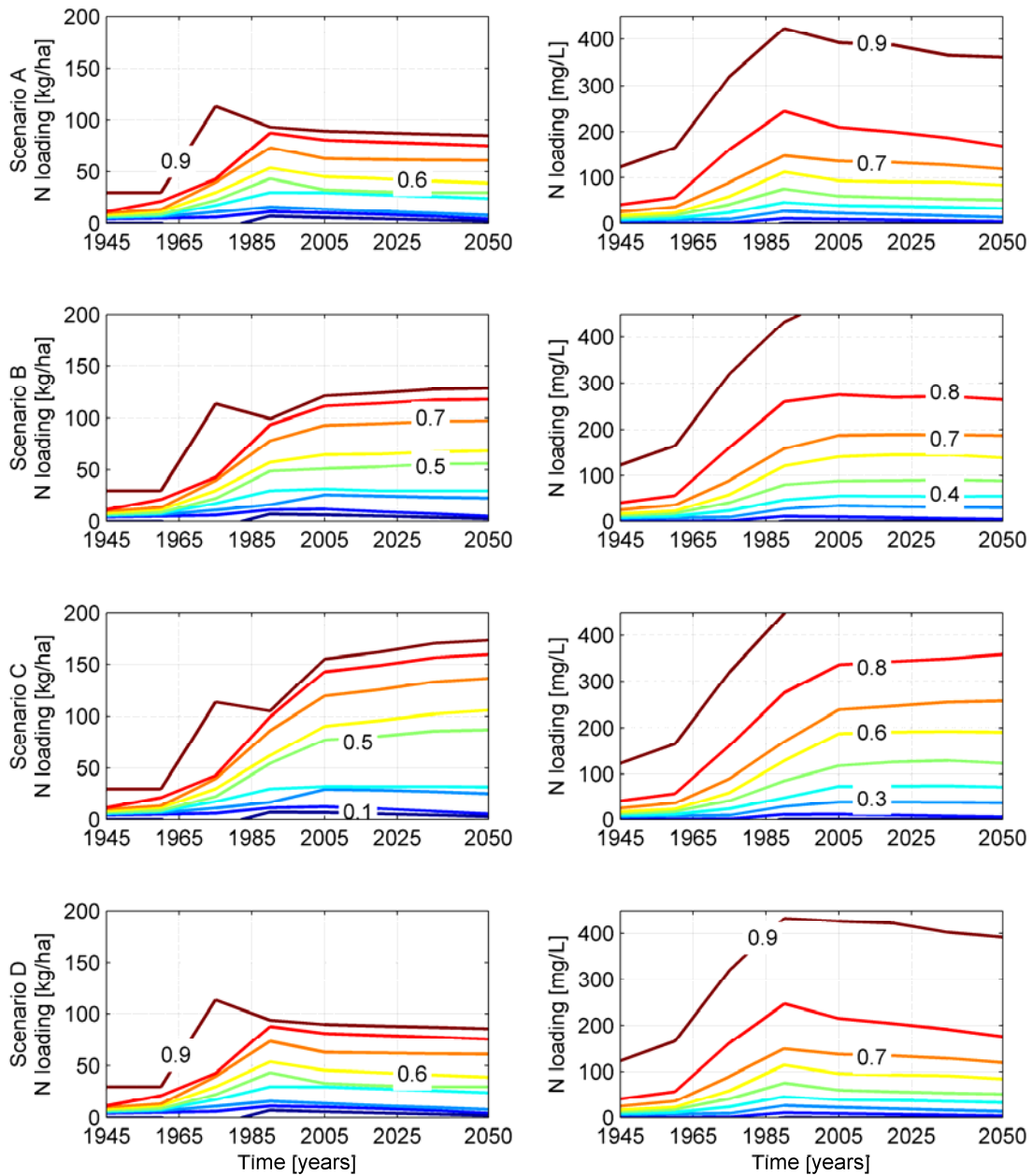


Figure 32. Exceedance probabilities of N loading rates as nitrate. All scenarios used here distribute excess nitrogen “by study area” and are explained in Section 1.8 of Technical Report 2 (Viers et al., 2012).

The above loading functions were computed based on the detailed simulation model. Yet, when the coarse simulation model is used to convert the rates to concentrations, the figures change significantly. Figure 33 illustrates the cumulative distribution functions of N loading over time based on the coarse model. While the output of the N loading algorithm is identical in both cases (compare left panels in both figures) the loading distribution is primarily a function of the starting points of streamlines (i.e., the point where the particles exit the aquifer during backward particle tracking). The four scenarios exhibit similar behavior as described previously (i.e., in scenario A and D the leaching rates are reduced after 1990, in scenario B [by study area] leaching rates remain nearly constant, and in scenario C [by study area] there is an increase in loading), but the magnitude of the overall loading is less compared to the detailed scenario. The main reason is that, in coarse simulation, the particles were likely to connect wells to the higher recharge areas, therefore, during the conversion from mass kg/ha to mg/L the concentrations appear to be smaller. The main reason for that can be attributed to the nature of the particle tracking algorithm that was used in each case (e.g., analytical particle tracking for the coarse case and numerical particle tracking for the detailed simulation.) Furthermore, the streams for

the coarse model are simulated by one square mile cells, while in detailed simulation the streams were assumed line sources with width approximately 50 m. It was found that, in the coarse model, a larger number of streamlines originate from cells associated with streams. Finally, the exceedance probabilities of the three reference concentration limits are shown in Figure 34. By comparing Figure 32 and Figure 34 we see that the N leaching into the groundwater concentration rates for the coarse model are 5% to 10% less than those of the fine model.



**Figure 33. Cumulative distribution function of N loading based on the coarse model. All scenarios used here distribute excess nitrogen “by study area” (see Section 1.8 of Technical Report 2, Viers et al., 2012).**

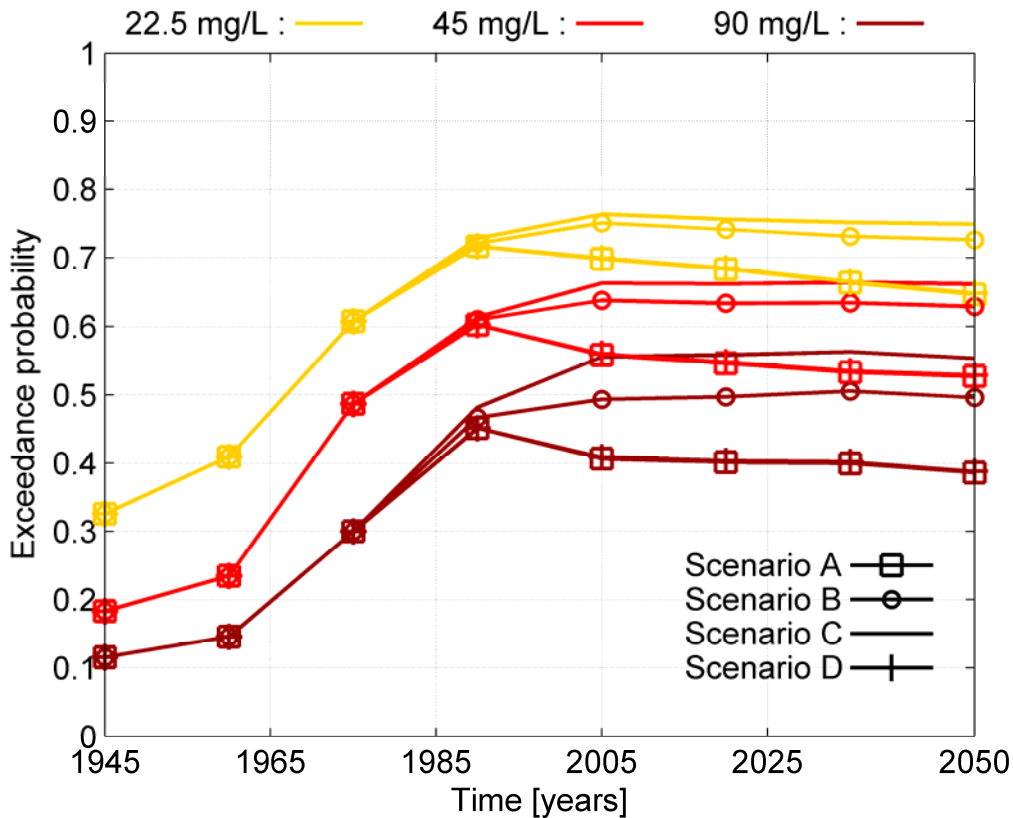


Figure 34. Exceedance probabilities of leaching rates as nitrate based on coarse model.. All scenarios used here distribute excess nitrogen “by study area” (see Section 1.8 of Technical Report 2, Viers et al., 2012).

## 5.2 Model Validation

Prior to using the model for future predictions we perform a validation step, where the outcome of the model is compared against real data that have been gathered from various sources (section 4.4). The rationale for the data gathering and processing is explained in detail in section 4.4; however, for completeness of the section we summarize the main steps. In the well database there is a large number of samples; however, these samples are not uniformly distributed, neither spatially nor temporally. To alleviate both non uniformities the study area was divided into a number of equal area cells (**Error! Reference source not found.**). Then, starting with 1950 and through 2010, for each cell, we compute the median of the annual well concentration means on a decadal basis. At the end of this process we obtain one representative concentration value for each cell for each decade. To calculate a de-clustered decadal average concentration for a particular region we compute the mean and the confidence interval of the mean of the decadal medians of the cells located in that region after they are log transformed. The back-transformed decadal means for the three regions of the TLB (**Error! Reference source not found.**) are shown in Figure 35 and Figure 36, with the 95% confidence interval of the mean.

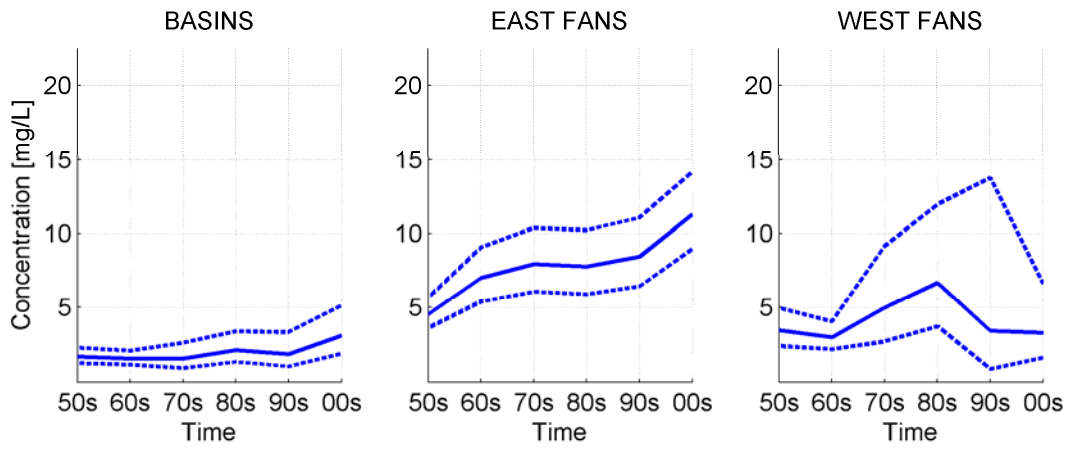
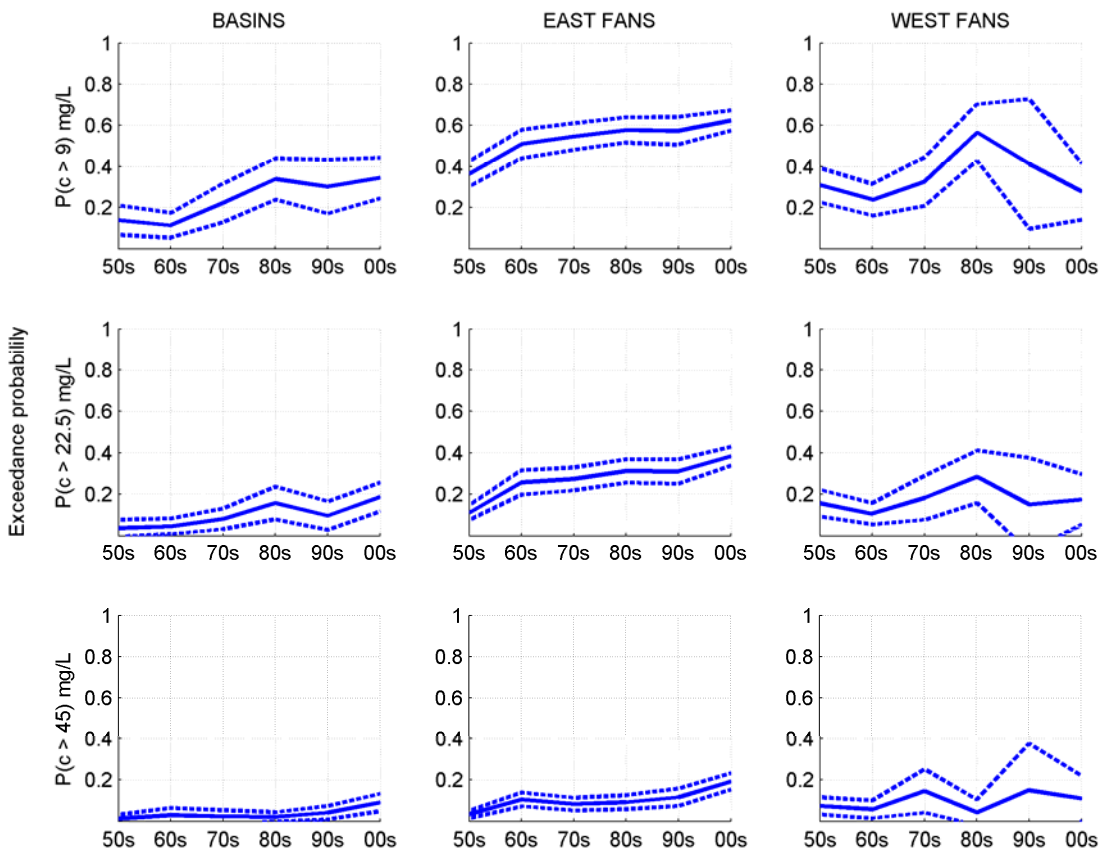


Figure 35. Decadal means of nitrate concentration for the three regions based on measured data. The solid line represents the mean and the dashed line the confidence interval.



**Figure 36. Decadal exceedance probabilities based on measured data. The solid line represents the de-clustered mean exceedance probability within each region and the dashed line the 95% confidence interval.**

Next, the measured data are compared against the simulated trends, based on the two modeling approaches, the fine and coarse model. Similar to the measured data, the simulated results were grouped into the same equal area cells and the de-clustered decadal means and confidence intervals of the means were calculated as described previously.

## Nitrate Concentration [mg/L]

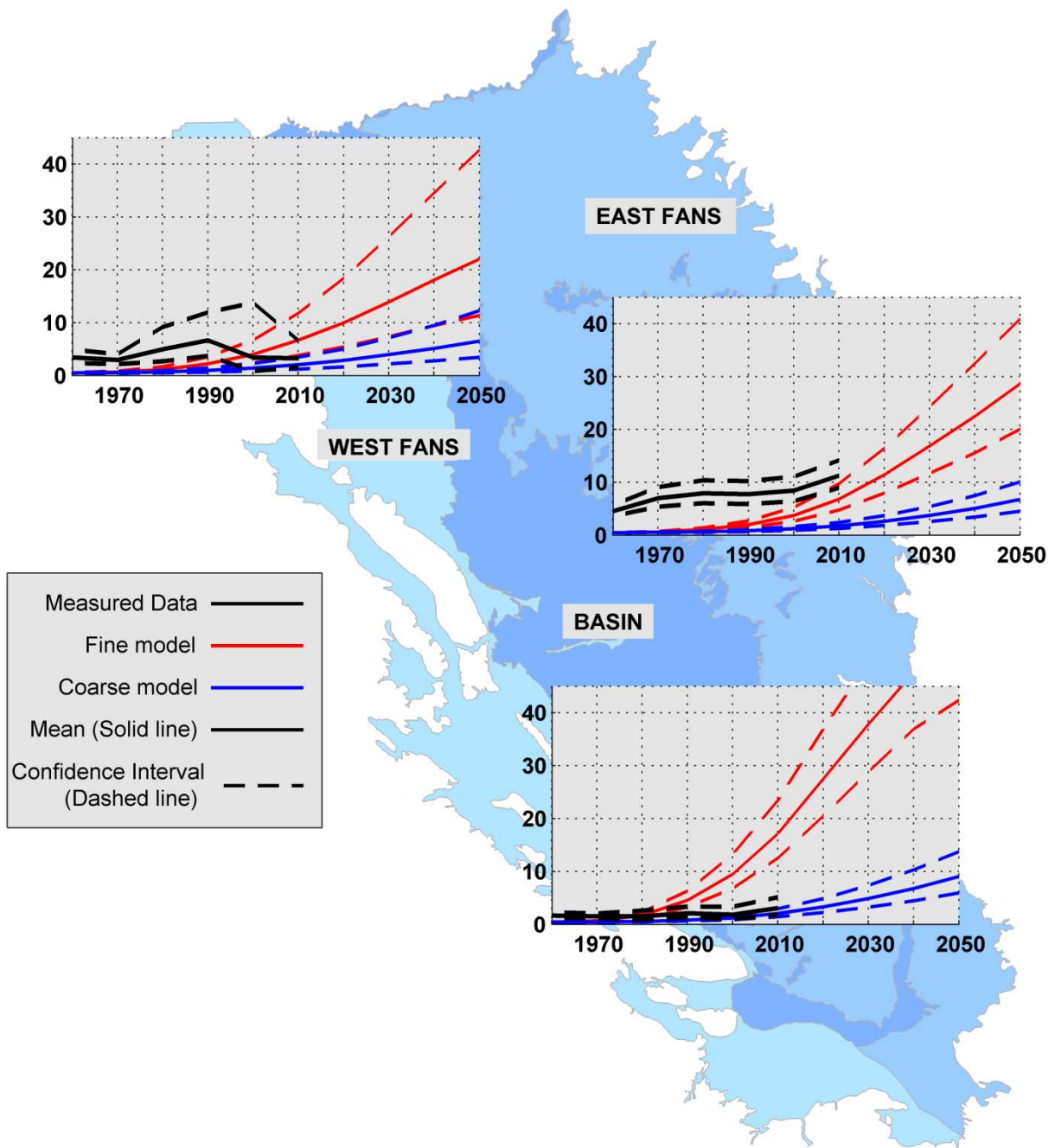


**Figure 37. De-clustered, back-transformed mean of equal area log nitrate medians in each region of annual well means. Comparison of mean and 95% confidence interval between measured data and model predictions.**

First we compare the de-clustered mean concentration data against the model responses (Figure 37). The solid lines represent the de-clustered, back-transformed mean of log transformed

decadal medians of annual well means calculated per equal area cell and the dashed line represents the confidence intervals. In general, both models fail to follow the early decades 1950–1980, with an exception for the Basin region, yet this is due to the very low measured concentrations. Note that, in all regions, the responses of both models are practically identical until the 1970s and both calculate very low concentrations at the beginning of the simulation. This is due to the fact that the groundwater nitrate loading model does not account for nitrate loading from any sources prior to 1945 – groundwater is assumed to be “clean” in 1945. The model also neglects any background nitrate concentration, which is typically on the order of ~4 mg/L nitrate or less. A second reason is that the groundwater model does not include shallow domestic wells with very low pumping rates, which are often affected before the larger production wells with longer screens, simulated here, are affected by higher nitrate concentrations. For the Basin region, the coarse model fits better to the data compared to the fine model. In the Basin region, the fine model predicts a more rapid increase in nitrate concentrations than the measured data suggest. For the Eastside Fans region, early nitrate data are higher than predicted by either model. For the 1990s and 2000s, the fine model, predicting a more rapid increase than the coarse model, comes relatively close to measured de-clustered mean. The coarse model predicts, on average, very low concentrations, less than 10 mg/l, while the upper limit of fine model is approximately identical with the lower limit of the data for the last decade. Note also that the slope for the last decade is somewhat similar to the slope suggested by the fine model. For the Westside Fans region, there is similar discrepancy as in the Eastside Fans region. The fine model predicts a slightly upward trend for the 1980s, which becomes more apparent during the 1990s, then significantly overpredicts the observed average low nitrate concentration measured during last decade (2000-2010). The coarse model underpredicts even further the higher average nitrate concentrations observed during the 1980s in the Westside Fans region, but appears to better predict the more recently observed low average nitrate concentrations. We caution that for the Westside Fans, the measured decadal mean values are based on much fewer measured data than for the other regions, with the source of data and the associated types of wells measured varying significantly over decades (see discussion in Section 5). Overall, it appears that the response of the fine model is closer to what is measured for the Eastside Fans than the coarse model. In contrast, the coarse model, showing a slower rise in nitrate concentrations than the fine model, due to the above discussed inherent conceptual model differences, compared better to the measured average nitrate concentrations in the Basin and Westside Fans regions. Neither model takes into account denitrification, which may be a significant process within the Corcoran Clay separating the upper from the lower aquifer system in the Basin and Westside Fans region. Future modeling efforts may be performed to accommodate denitrification in the Corcoran Clay and other portions of the aquifer system, for which denitrification rates would have to be determined.

## Exceedance Probability > 9 mg/L

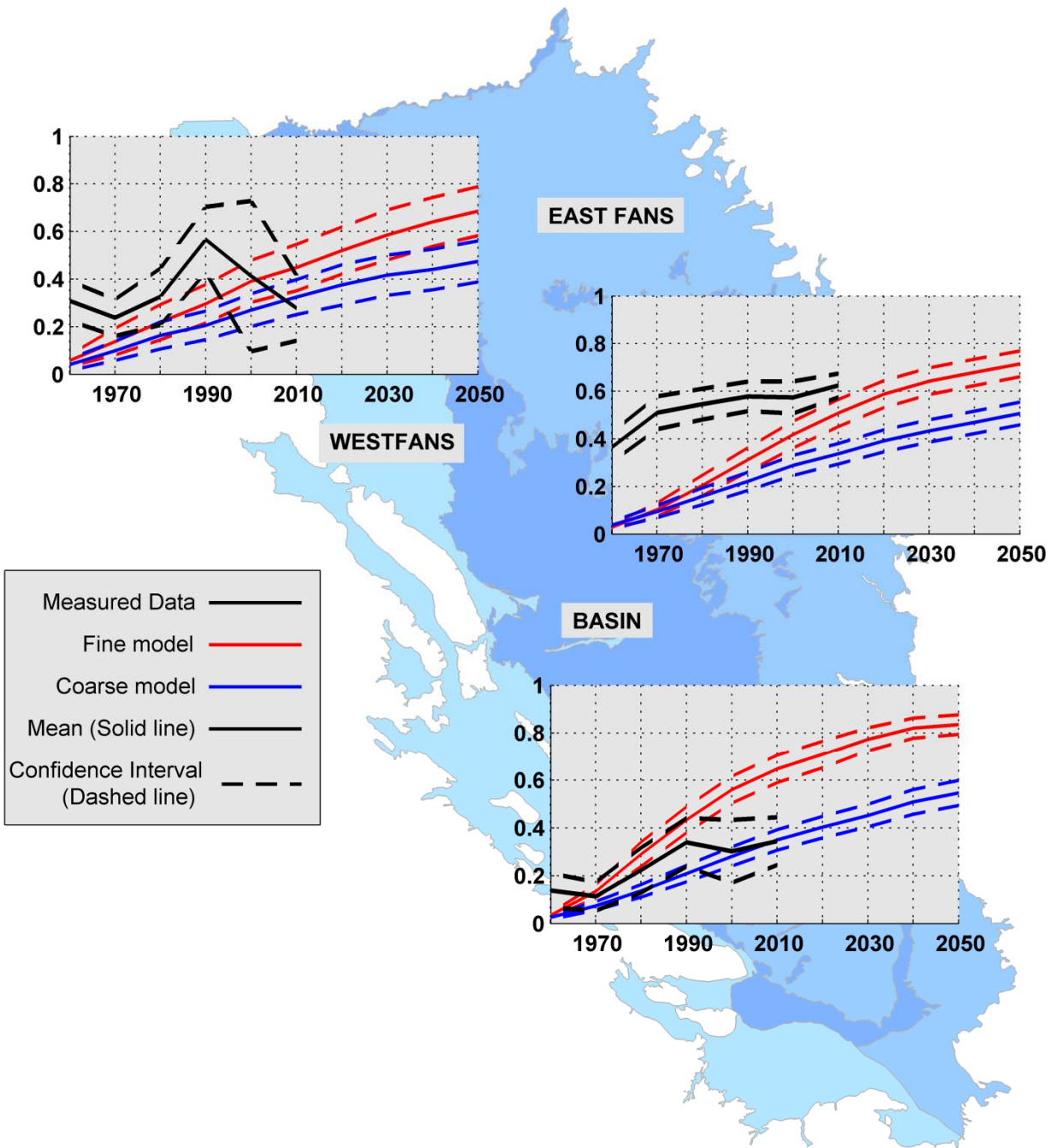


Figure 38. Comparison of decadal trends of exceedance probability of 9 mg/L, between measured data and model predictions.

## Exceedance Probability > 22.5 mg/L

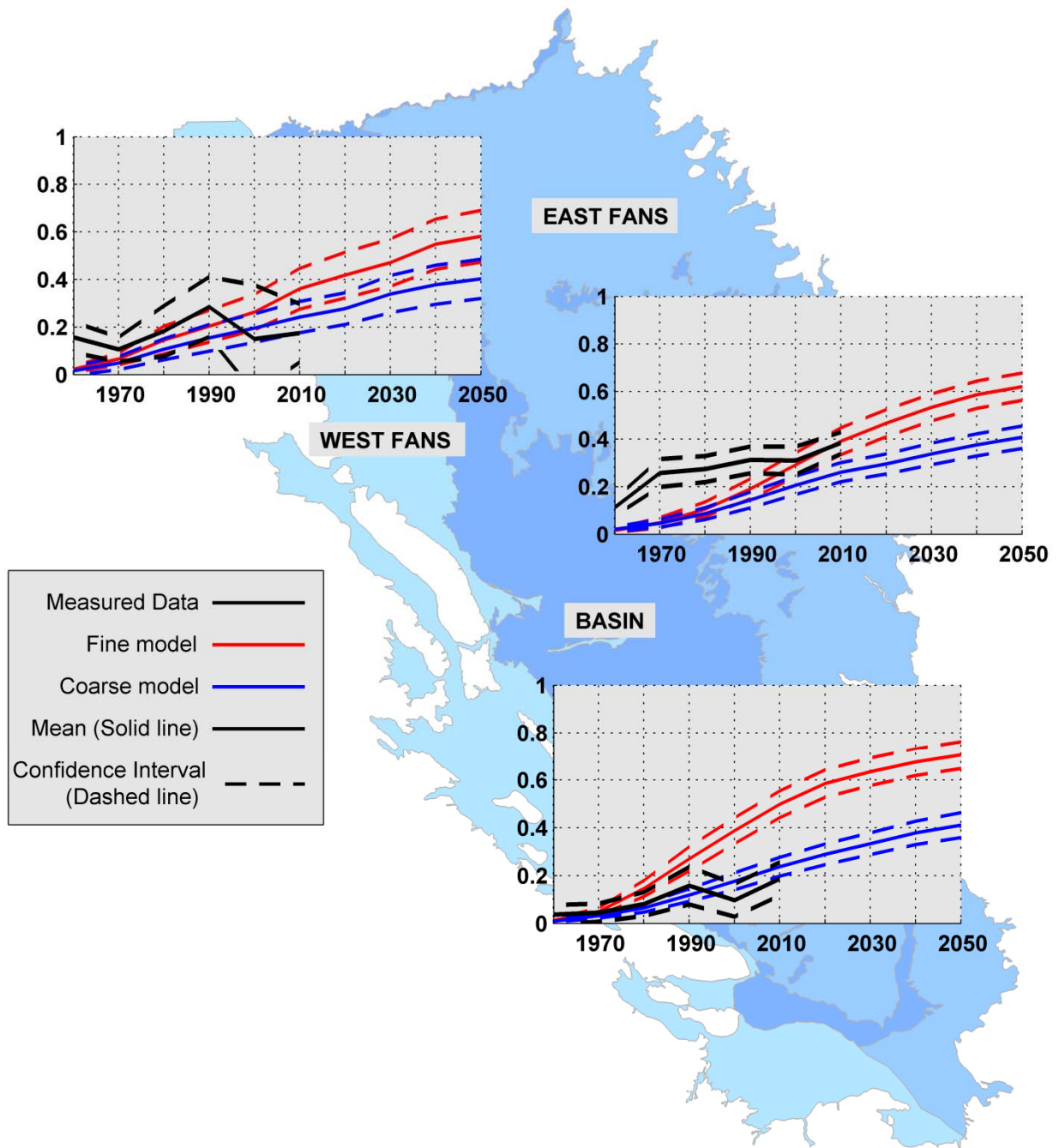


Figure 39. Comparison of decadal trends of exceedance probability of 22.5 mg/L, between measured data and model predictions.

## Exceedance Probability > 45 mg/L

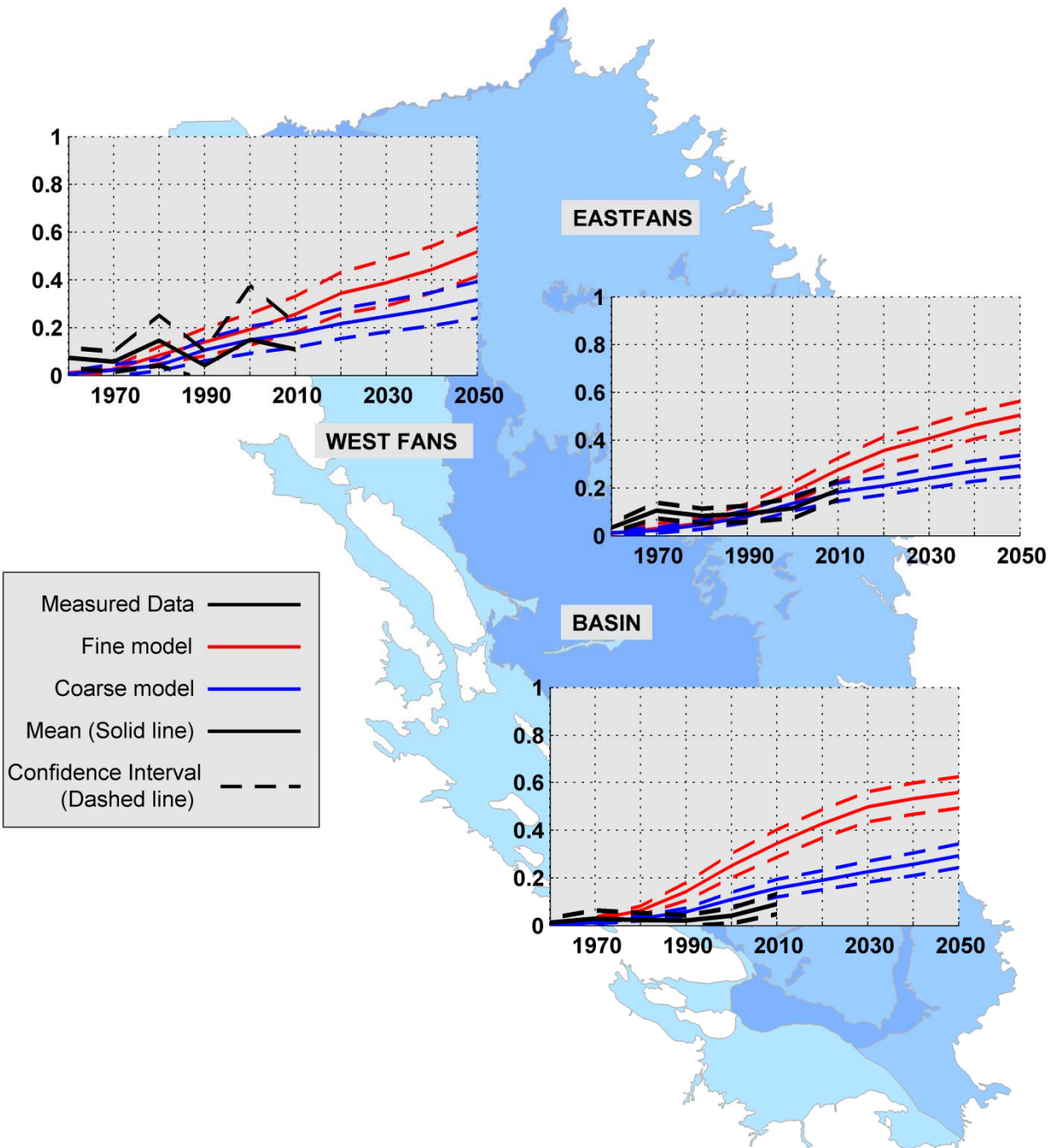


Figure 40. Comparison of decadal trends of exceedance probability of 45 mg/L, between measured data and model predictions.

Another way to study the decadal trends is to examine the exceedance probabilities for a given concentration. To this end we computed the exceedance probabilities for concentration levels 9, 22.5 and 45 mg/L. Note that the drinking water limit is 45 mg/L. Figure 38 illustrates the mean decadal exceedance probabilities of 9 mg/L and the confidence intervals based on the measured data and the responses of the two models per region. Interestingly, for the Basin region the fine and the coarse models follow the upper and lower limit of confidence intervals of the real data for the 70s and 80s, but they fail to reproduce the abrupt change that occurs between 80s and 90s. For the Eastside Fans region both models underestimate their predictions during the first decades, while the response of the fine model are somewhat closer the measured data. Both models behave in a similar manner for the Westside Fans region predicting a continuous increase, yet based on the data there is a significant decreasing trend from the 80s onwards, which is not captured by either model, but maybe due to a sampling bias in the measured data. The response of the models for the exceedance probabilities of 22.5 mg/L (Figure 39) is very similar to the exceedance probabilities of 9 mg/L. Both models fail to capture the decreasing trends for the Westside Fans and Basins regions, while the predictions of the fine model are closer to real data for the Eastside Fans region.

Interestingly, the models are showing better fit for the exceedance probabilities of the MCL (45 mg/L) (Figure 40). In antithesis with the previous figures, the trends in all three regions show a general increasing trend. For the Westside Fans and Eastside Fans regions, both models respond similarly, although the coarse model seems to fit slightly better with the real data. For the Basin region, both models predict a significant upward trend after the 70s; however, based on the real data, the upward trend only occurs two decades later.

In conclusion, the measured nonpoint source pollution system behaves in certain cases very different than what would be expected based on the model. In every case, both models failed to reproduce any downward trend. The fine model predictions seem to fit to the measured data better for the last decade, especially for the Eastside Fans region. Comparison between the models confirms, in certain cases, our expectation that the coarse model tends to underestimate, while the fine model tends to overestimate the actual concentration levels, although there are certain cases where this general “rule” is violated. Accounting for denitrification, with independently measured denitrification rates would provide a tool to improve the average model predictions when compared to average measured data.

### ***5.3 NPSAT Modeling Predictions***

The N loading functions for each scenario were convoluted with the URFs, a process that involves only analytical calculations; hence, we were able to calculate each alternative scenario A, B (by study area), C (by study area), and D (for detailed description of these scenarios, see Section 1.8 of Technical Report 2; Viers et al., 2012). The BTC for each well are shown in Figure 41. The thin colored lines represent the well BTCs, the red lines show the drinking water limit, and the black thick lines depict the exceedance probabilities. It can be seen that there is a significant number of wells with very fast

BTCs (i.e., shallow wells with relatively small screen lengths), and also a significant number of wells that exhibit very slow responses (e.g., deep wells).

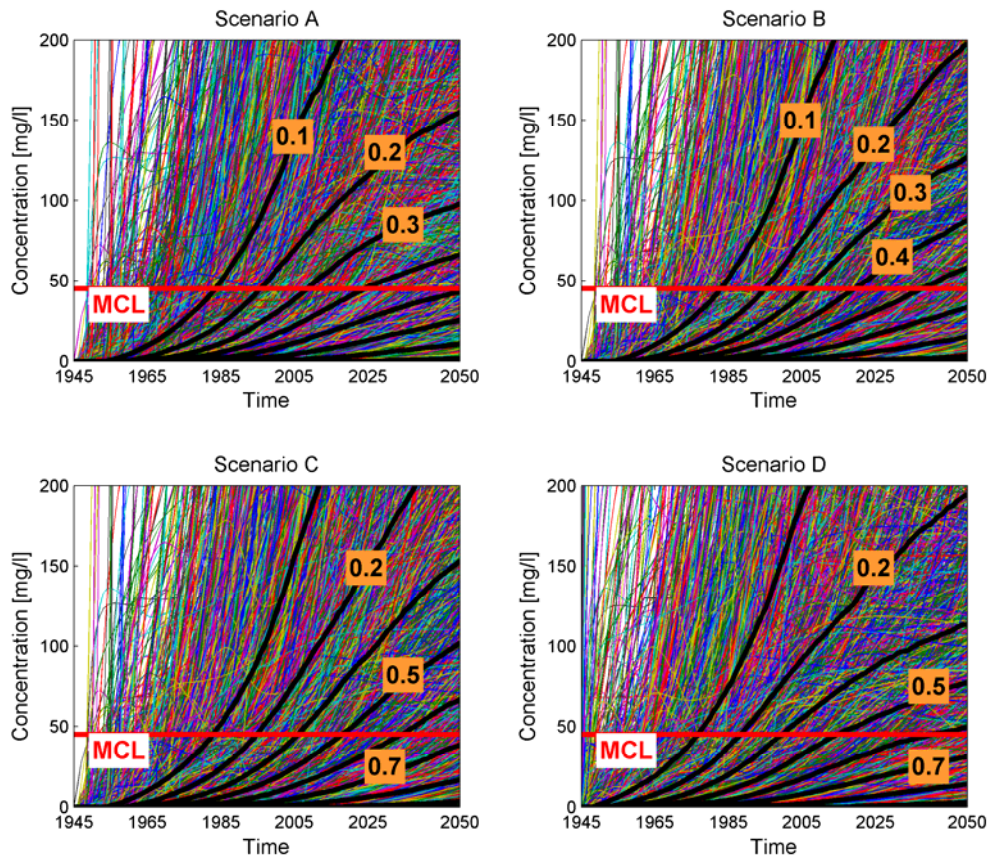


**Figure 41. Breakthrough curves based on model simulation for each well for the four alternative (by study area) scenarios (thin colored lines). The black thick lines correspond to exceedance probabilities and the red lines show the drinking water limit (45 m/L). Scenario details are provided in Section 1.8 of Technical Report 2 (Viers et al., 2012).**

Although the simulated BTCs are temporally uniformly distributed, their spatial distribution is non-uniform. Therefore we utilized a similar method as in the previous section (4.7.5.2) to process the results, where the TLB area was split into six basins (Kern, Kings, Tule, Tulare Lake, Kaweah, and Westside). Each basin was divided into equal area cells, and, according to the previous method, we computed the means and confidence intervals for each basin. Figure 42 shows the comparison between the fine model and the coarse model using the loading functions of scenario D. It can be seen that in all basins the fine model (red lines) predicts higher concentrations compared to coarse model (blue lines). Note also that the uncertainty is rather high in most basins (e.g., Kaweah, Tule), and in particular for the future predictions. In addition, the two models exhibit large discrepancies, yet a few safe conclusions

can be drawn. For example, both models predict that for the Kings and Kern basins the concentrations will remain below the drinking water limit. On the other hand, both models predict high concentrations for the Kaweah basin. By the year 2050 the mean concentration, based on the fine model, is expected to be twice the MCL, and the coarse model estimates concentrations close to MCL with but significant variance in its estimation). This may be attributed to the fact that Kaweah basin contains the majority of dairies. As far as the remaining three basins are concerned, the models exhibit large discrepancies. For example, the coarse model predicts that the concentration in Tule basin will not exceed 10 mg/L by 2050 (the upper confidence limit), while the fine model predicts that the concentration will not exceed, but will be very close to the MCL, yet, this figure is associated with large variance. Note the upper confidence limit is approximately twice the MCL. For the basins on the west side, the coarse model predicts a similar upward trend, where the mean concentration by the year 2050 is expected to be 20 mg/L, approximately. On the other hand, the fine model predicts significantly higher concentrations.

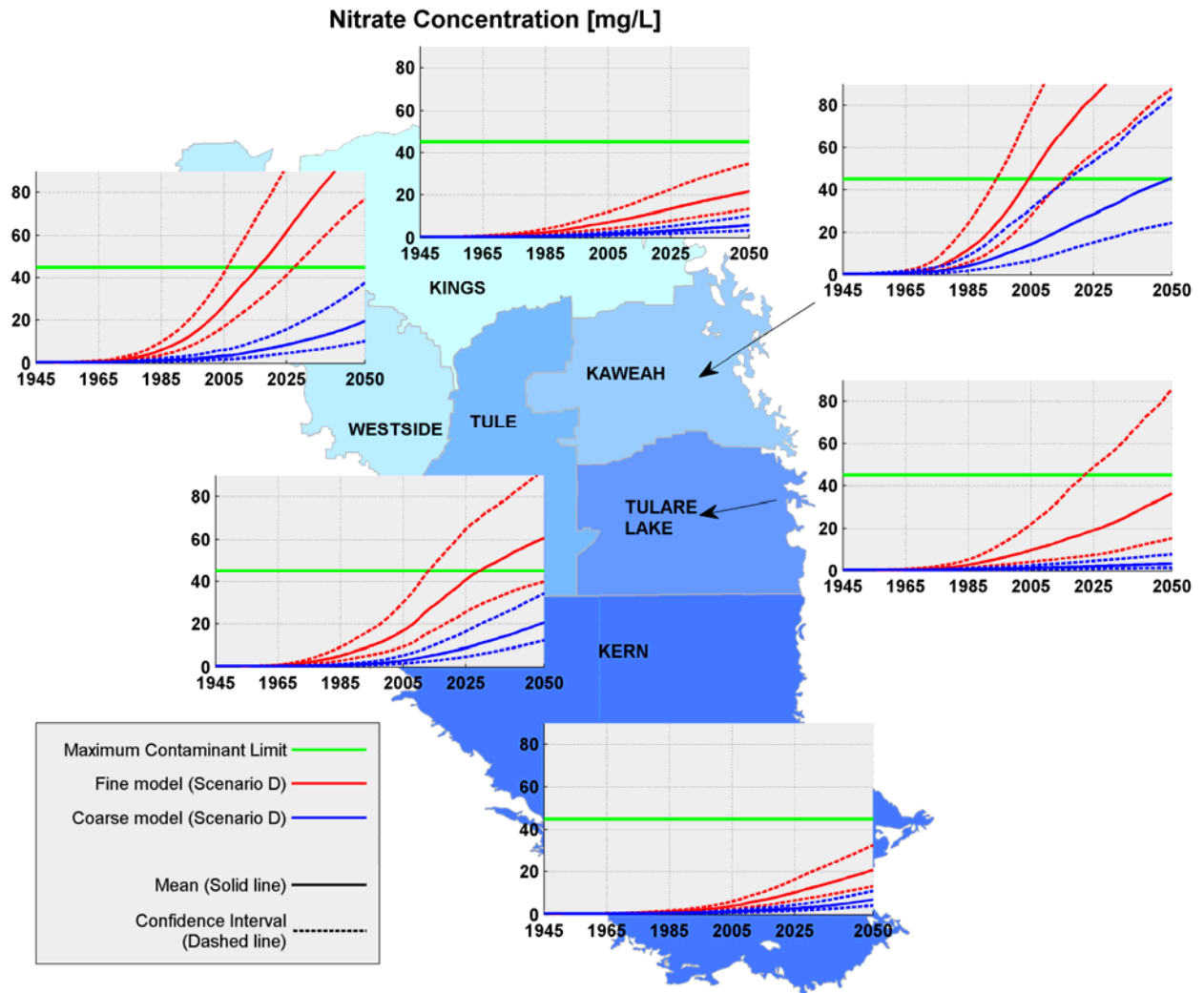
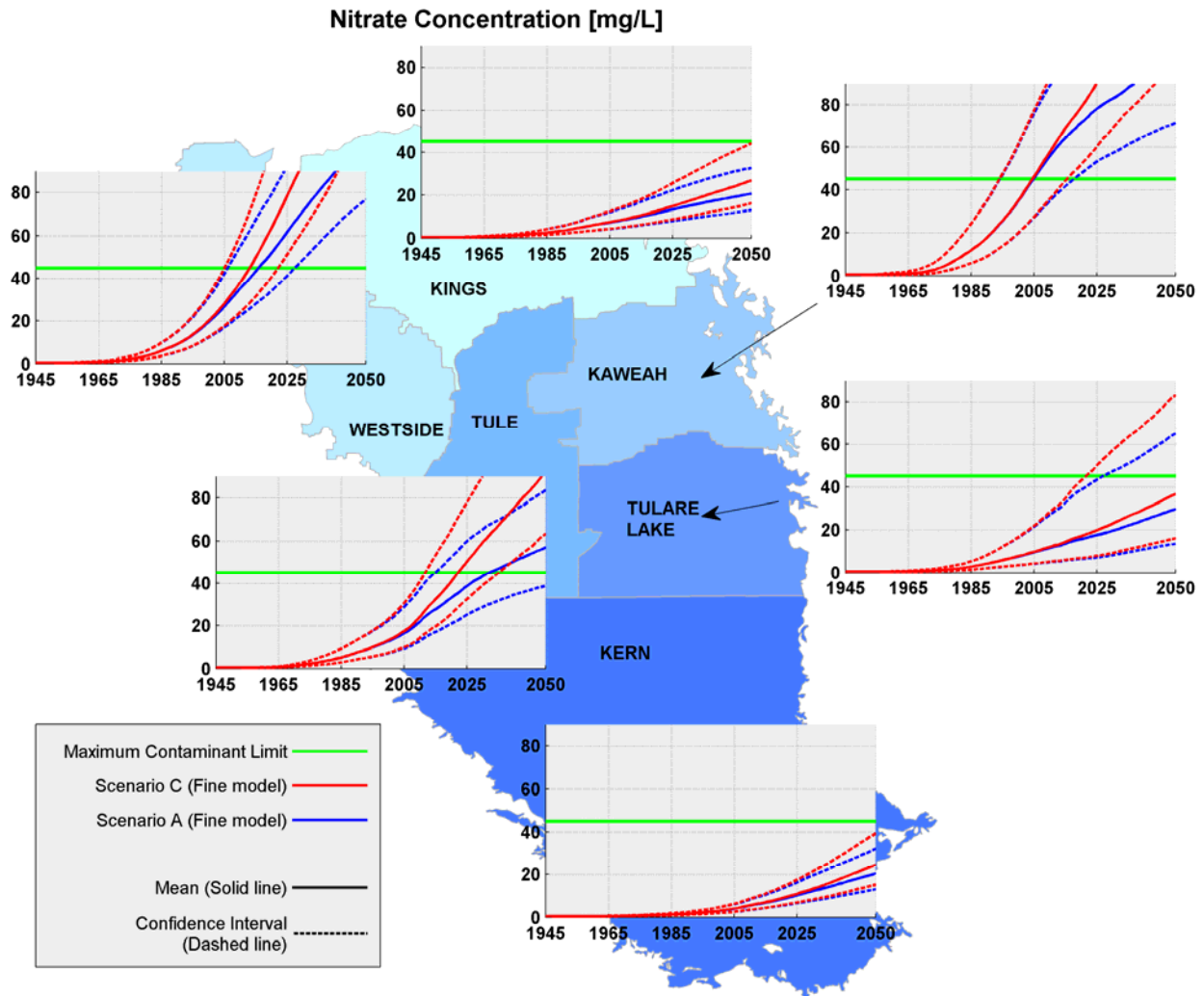


Figure 42. Comparison between coarse model and fine model based on scenario D.



**Figure 43. Comparison between scenario A and C based on the fine model predictions.**

While the models may not accurately capture the actual responses they can still be useful tools to evaluate the impact of alternative scenarios. Figure 43 plots the predictions of the fine model based on the loading scenarios A and C. Scenario C is considered here the worst scenario. It can be seen that the impact of scenario C for the basins of Kern, Tulare Lake, and Kings is rather negligible. In antithesis, the basins of Kaweah, Tule, and West side are significantly affected.

Last, we compute the exceedance probabilities for each basin, based the fine and the coarse models for three given limits (e.g., 22.5 mg/L (half the MCL), 45 mg/L (MCL), and 90 mg/L (twice the MCL)). Figure 44 shows the exceedance probabilities based on the fine model using scenario D, while Figure 45 shows the exceedance probabilities based on the coarse model and the same scenario D. By comparing the two figures we observe similar discrepancy between the two models. The fine model

tends to predict higher exceedance probabilities compared to the exceedance probabilities of the coarse model.

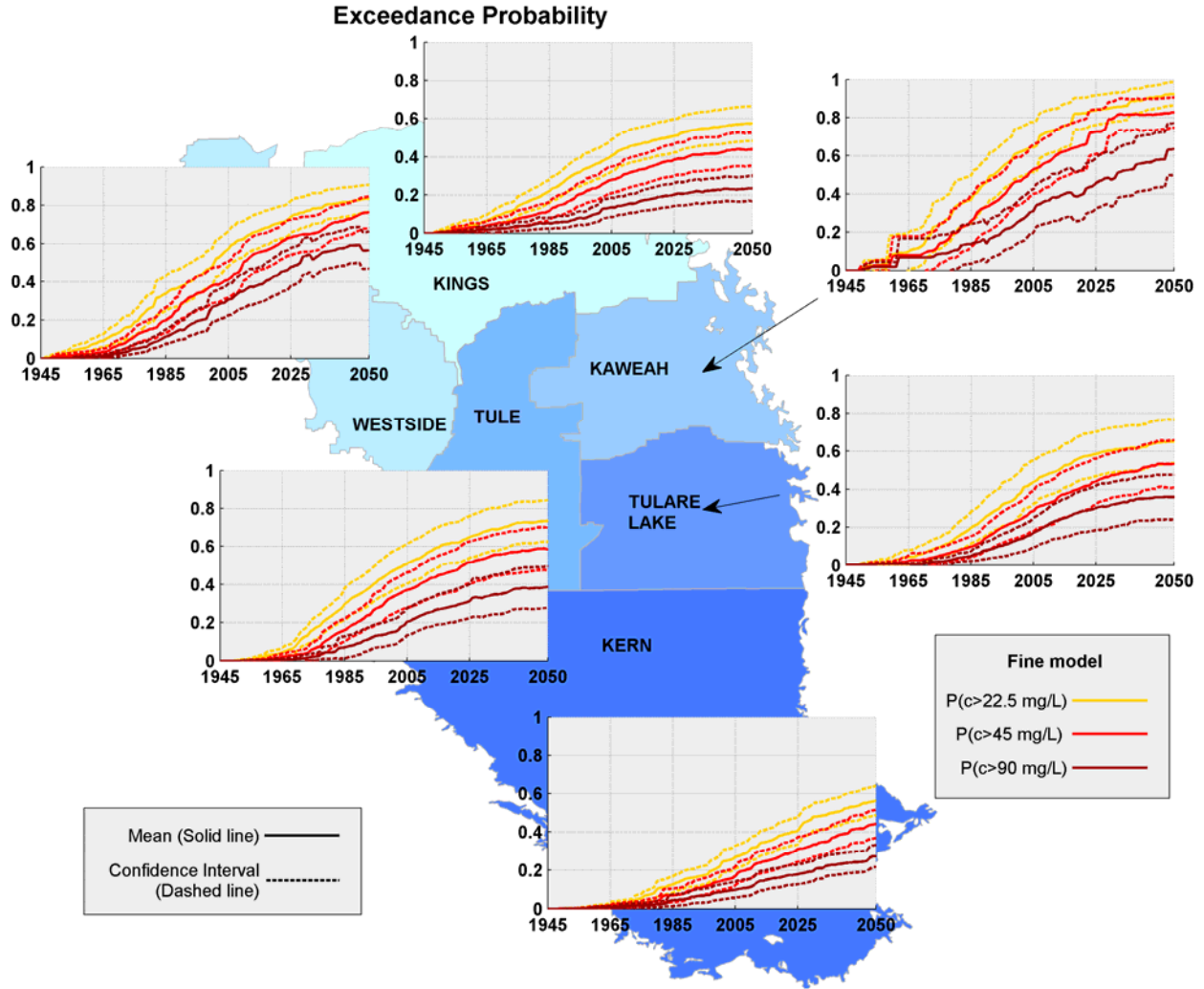
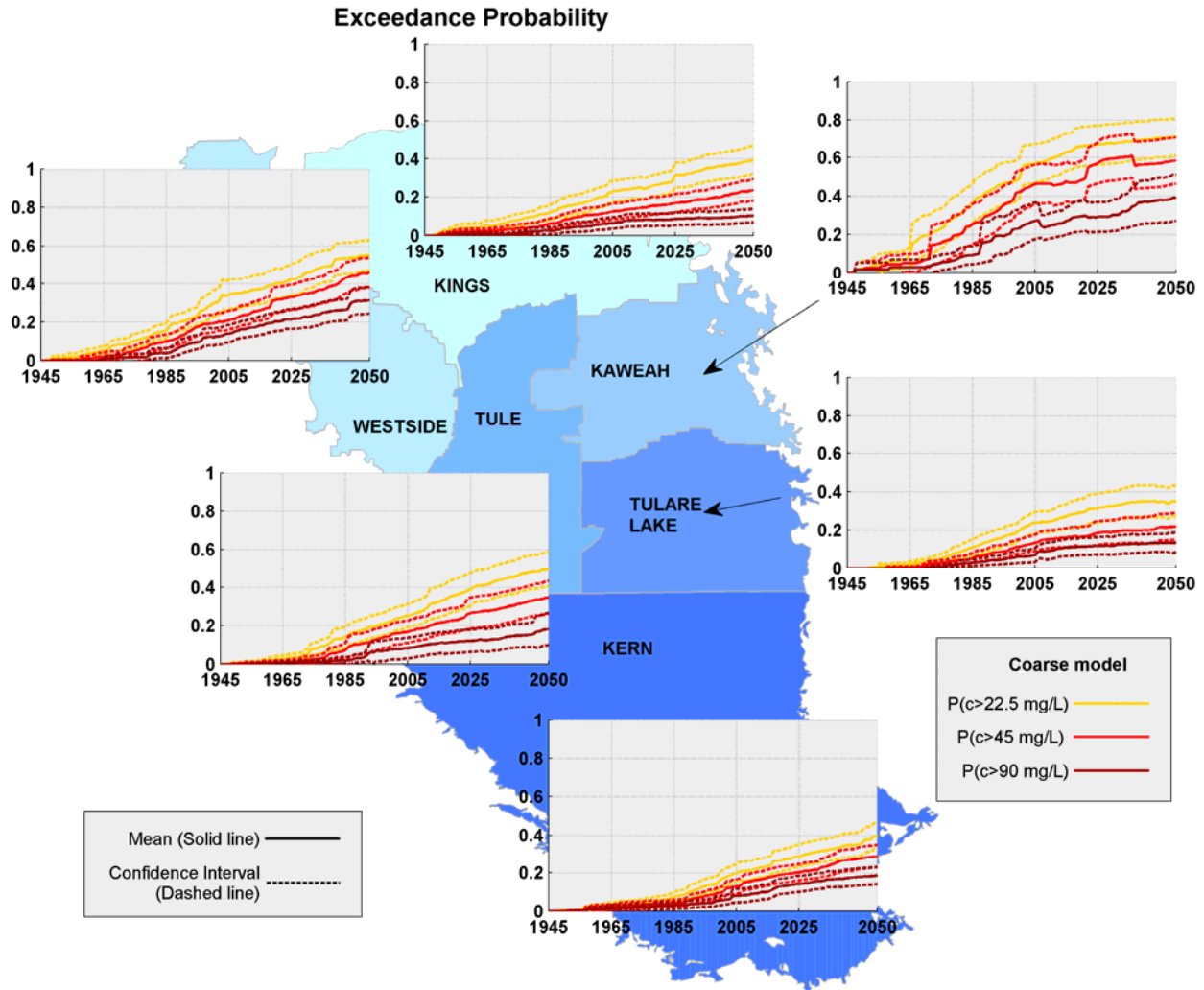


Figure 44. Exceedance probabilities for 22.5, 45, and 90 mg/L based on the fine model.



**Figure 45. Exceedance probabilities for 22.5, 45, and 90 mg/L based on the coarse model.**

For example, by the year 2050, the exceedance probability of the drinking water limit for the basin of Kern, based on the fine model, is approximately 30%, while based on the coarse model the same probability is ~42%. Similarly for the other regions, the two models exhibit a discrepancy on the order of 10% to 20%.

In conclusion, it is apparent that there is a strong disagreement between the model predictions, yet the two models are consistent as far as the impact of the alternative scenarios is concerned. In addition, they are consistent regarding the trends for each basin. The basin of Kaweah exhibits the highest concentration levels among the six basins (e.g., 80% and 60% of wells exceed the drinking water limit based on fine model and coarse model, respectively). For the Kern and Kings basins the two models converge that the concentration and exceedance probabilities will remain low, while a notable increase is expected for the west basins.

The difference between the two models indicates that two similar models (e.g., both are based on the CVHM model) may exhibit very different results. As shown in the previous paragraph, the streamline length distributions were quite different between the two models, with the coarse model having longer streamlines with older ages. Therefore, it is not surprising that the coarse model predicts lower concentrations. Although the fine model captures more precisely the local variability of the head field, one of the main drawbacks of the fine model is that it fails to maintain the general water balance due to the simplistic decomposition method. For example 85% of the groundwater recharge is diffuse recharge and the remaining corresponds to stream recharge. Yet the number of streamlines that originate from the streams, based the fine model, is approximately 6.5%. For the coarse model it appears that 20% of the streamlines originate from the streams. Therefore, these two models can be seen as the two extremes, where the fine model overestimates nitrate contamination and the coarse model tends to underestimate.

Overall the simulation of nonpoint source pollution for large groundwater basins is a subject that requires further research and deeper understanding of the transport mechanisms. The fine model approach, with adjustments to the simplified domain decomposition method and after accounting for denitrification, is the most promising approach. The coarse model approach, while apparently better in predicting average nitrate concentrations in some instances than the fine model, when comparing to actual average regional data, has been shown to have intrinsic weakness in the computation of travel paths that the fine model is able to address better. As a result, the coarse model appears to make better predictions especially in areas, where in fact denitrification is a significant controlling factor. Further improvements to the fine model approach are needed, and independently measured denitrification rates in the TLB region, to improve on the current modeling capability.

## 6. Conclusions

---

- Travel times in the unsaturated zone range from less than one year to decades, depending mostly on depth to groundwater, and on recharge rates under agricultural operations.
- We developed a new groundwater modeling tool that can be used in conjunction with estimated nitrate loading maps for past, current, and future conditions (Viers et al., 2012) to simulate the development of nitrate exceedance probabilities in sub-regional aquifer systems of interest. The model is consistent with measured nitrate concentration distributions and suggests significant increases in nitrate exceedance rates over the coming years.

## 7. Acknowledgments

---

This work was funded by the State Water Resources Control Board under agreement number 04-184-555-2 and 09-122-250. Portions of this Task Report were originally published as Section 7 in Boyle et al. (2012).

## 8. References

---

- Addiscott, T. M. and Wagenet, R. J., 1985. Concepts of solute leaching in soils: a review of modeling approaches. *Journal of Soil Science*, 36, 411–424.
- Aller, L., Bennett, T., Lehr, J. H., Petty, R. J., and Hackett, G., 1987. DRASTIC: A Standardized System for Evaluating Groundwater Pollution Potential Using Hydrogeologic Settings. EPA-600/2-87-035, Environmental Protection Agency.
- Almasri, M. N. and Kaluarachchi, J. J., 2007. Modeling nitrate contamination of groundwater in agricultural watersheds. *Journal of Hydrology*, 343, 211–229.
- Baker, R. O., Kuppe, C. S., Bora, S. R., and Batycky, R. P., 2002. Full-field modeling using previous streamline-based simulation: Four case studies. *SPE Reservoir Evaluation & Engineering*, 5, 126–134.
- Bandilla, K. W., Rabideau, A. J., and Jankovic, I., 2009. A parallel mesh-free contaminant transport model based on the analytic element and streamline methods. *Advances in Water Resources*, 32, 1143–1153.
- Basso B., Cammarano, D., Troccoli, A., Chen, D., and Ritchie, J.T., 2010. Long-term wheat response to nitrogen in a rainfed Mediterranean environment: Field data and simulation analysis. *European Journal of Agronomy*, 33, 132–138.
- Bear, J., 1979. *Hydraulics of Groundwater*. McGraw-Hill, New York, 567 pp.
- Beltman, W. H. J., Boesten, J. J. T. I., and van der Zee, S. E. A. T. M., 1995. Analytical modeling of pesticide transport from the soil surface to a drinking water well. *Journal of Hydrology*, 169, 209–228.
- Berkowitz, B., Cortis, A., Dentz, M., and Scher, H., 2006. Modeling non-Fickian transport in geological formation as a continuous time random walk. *Reviews of Geophysics*, 44, 1–49.
- Bhambri, P., and Mohanty, K. K., 2008. Two- and three- hydrocarbon phase streamline-based compositional simulation of gas injections. *Journal of Petroleum Science and Engineering*, 62, 1627.
- Bloomfield, J. P., Williams, R. J., Goody, D. C., Cape, J. N., and Guha, P., 2006. Impacts of climate change on the fate and behaviour of pesticides in surface and groundwater – A UK perspective. *Science of the Total Environment*, 369, 163–177.
- Blunt, M. J., Liu, K., and Thiele, T. R., 1996. A generalized streamline method to predict reservoir flow. *Petroleum Geoscience*, 2, 259–269.
-

- Botter, G., Settin T., Marani M., and Rinaldo A., 2006. A stochastic model of nitrate transport and cycling at basin scale. *Water Resour. Res.*, 42, W04415.
- Bouwman, F., Beusen, A. H. W., and Billen, G., 2009. Human alteration of the global nitrogen and phosphorus soil balances for the period 1970–2050. *Global Biogeochemical Cycles*, 23, 1–16.
- Bower, H., 2000. Integrated water management: Emerging issues and challenges. *Agricultural Water Management*, 45, 217–228.
- Burkhalter, J. P., and Gates, T. K., 2005. Agroecological impacts from salinization and waterlogging in an irrigated river valley. *Journal of Irrigation and Drainage Engineering*, 131, 197–209.
- Burow, K. R., Nolan, B. T., Rupert, M. G., and Dubrovsky, N. M., 2010. Nitrate in groundwater of the United States, 1991-2003. *Environmental Science & Technology*, 44, 4988–4997.
- Burow, K. R., Dubrovsky, N. M., and Shelton, J. L., 2007. Temporal trends in concentrations of DBCP and nitrate in groundwater in the eastern San Joaquin Valley, California, USA. *Hydrogeology Journal*, 15, 991–1007.
- Carle, S. F., Esser, B. K., and Moran, J. E., 2006. High-resolution simulation of basin-scale nitrate transport considering aquifer system heterogeneity. *Geosphere*, 2, 195–209.
- Chakraborti, D., Das, B. and Murrill, M. T., 2011. Examining India’s groundwater quality management. *Environmental Science & Technology*, 45, 27–33.
- Cho, J., and Mostaghimi, S., 2009. Dynamic agricultural non-point source assessment tool (DANSAT): Model development. *Biosystems Engineering*, 102, 486–499.
- Civita, M. and De Maio, M., 2004. Assessing and mapping groundwater vulnerability to contamination: The Italian “combined” approach. *Geofísica Internacional*, 43, 513–32.
- Cortis, A., Harter, T., Hou, L. L., Atwill, E. R., Packman, A. I., and Green, P. G., 2007. Transport of *cryptosporidium parvum* in porous media: Long-term elution experiments and continuous time random walk filtration modeling. *Water Resources Research*, 42, 1–12.
- Corwin, D. L. and Wagenet, R. J., 1996. Applications of GIS to the modeling of non-point source pollutants in the Vadose Zone: A conference overview. *Journal of Environmental Quality*, 25, 403–411.
- Corwin, D. L., Loague, K., and Ellsworth, T. R., 1999. *Assessment of Non-Point Source Pollution in the Vadose Zone*. AGU Press, Washington, DC.
- Cvetkovic, V., 2011. The tempered one-side stable density: a universal model for hydrological transport? *Environmental Research Letters*, 6(3), 034008, 5pp.

- Domenico, P. A. and Schwartz, F. W., 2008. *Physical and Chemical Hydrogeology*, 2nd Ed. Wiley & Sons, New York, NY.
- Dowd, B. M., Press, D. and Los Huertos, M., 2008. Agricultural nonpoint source water pollution policy: The case of California's Central Coast. *Agriculture, Ecosystems, and Environment*, 128, 151–161.
- Faunt, C. C., 2009. *Groundwater Availability of the Central Valley Aquifer, California*. Professional Paper 1766, United States Geological Survey.
- Fehlberg, E., 1969. Low-order Classical Runge-Kutta Formulas with Step-size Control and Their Application to Some Heat Transfer Problems. NASA Technical Report, NASA TR R-315.
- Fogg, G. E., LaBolle, E. M., and Weissmann, G. S., 1999. Groundwater Vulnerability Assessment: Hydrogeologic Perspective and Example from Salinas Valley, California, pp. 45-61, *Assessment of Non-Point Source Pollution in the Vadose Zone*, Vol. 108, Geophysical Monograph Series, edited by Corwin, D.L., et al., pp. 309-322. AGU, Washington DC.
- Freeze, R. A., and Cherry, J. A., 1979. *Groundwater*. Prentice-Hall International, Hemel Hempstead, Hertfordshire.
- Frind, E. O., 1988. Solution of the advection-dispersion equation with free exit boundary. *Numerical Methods for Partial Differential Equations*, 4, 301–313.
- Fry, V. A., Istok, J. D., and Guenther, R. B., 1993. An analytical solution to the solute transport equation with rate-limited desorption and decay. *Water Resources Research*, 29, 3201–3208.
- Gelhar, L., Welty, C., and Rehfeldt, K., 1992. A critical review of data on field-scale dispersion in aquifers. *Water Resources Research*, 28, 1955–1974.
- Gerritsen, M. G., 2008. *Industrial Compositional Streamline Simulation for Efficient and Accurate Prediction of Gas Injection and WAG Processes*. Final Report, Oil & Natural Gas Technology.
- Ginn, T. R., 2002. Streamtube-ensemble techniques for nonlinear multicomponent reactive transport in heterogeneous media, in R. Govindaraju (ed.) *Stochastic Methods in Subsurface Contaminant Hydrology*, ASCE Press, 410p.
- Giordano, M. (2009) Global groundwater? Issues and solutions. *Annual Review of Environment and Resources*, 34, 153–178.
- Govindaraju, R. S. (ed.), 2002. *Stochastic Methods in Subsurface Contaminant Hydrology*. ASCE, New York, NY.
- Green, C. T., Böhlke, J. K., Bekins, B. A., and Phillips, S. P., 2010. Mixing effects on apparent reaction rates and isotope fractionation during denitrification in a heterogeneous aquifer. *Water Resources Research*, 46, W08525.
- GWSP Digital Water Atlas, 2008, Map 48: Nitrogen Load (Mobilizable) (V1.0), <http://atlas.gwsp.org>.

- Hansen, B., Thorling, L., Dalgaard, T., and Erlandsen, M., 2011. Trend reversal of nitrate in Danish groundwater – A reflection of agricultural practices and nitrogen surpluses since 1950. *Environmental Science & Technology*, 45, 228–234.
- Hansen, S., Jensen, H. E., Nielsen, N. E. and Svendsen, H., 1991. Simulation of nitrogen dynamics and biomass production in winter wheat using the Danish simulation model Daisy. *Nutrient Cycling in Agroecosystems*, 27, 245–259.
- Harter, T., Davis, H., Mathews, M. C., and Meyer, R. D., 2002. Shallow groundwater quality on dairy farms with irrigated forage crops. *Journal of Contaminant Hydrology*, 55, 287–315.
- Heng, L. K., and White, R. E., 1996. A simple analytical transfer function approach to modeling the leaching of reactive solutes through field soil. *European Journal of Soil Science*, 47, 33–42.
- Herrera, P. A., Valocchi, A. J., and Beckie, R. D., 2010. A multidimensional streamline-based method to simulate reactive solute transport in heterogeneous porous media. *Advances in Water Resources*, 33, 711–727.
- Humenik, F. J., Smolen, M. D., and Dressing, S. A., 1987. Pollution from nonpoint sources: Where we are and where we should go. *Environmental Science & Technology*, 21, 737–742.
- Jaladi, M., and Rowell, D. L., 2008. Prediction leaching of potassium using the convective-dispersive and the convective log-normal transfer function models. *Environmental Geology*, 55, 863–874.
- Jang, M., 2002. 3D aquifer characterization using stochastic streamline calibration. *Advances in Water Resources*, 30, 420–429.
- Jang, M., and Choe, J., 2002. Stochastic optimization for global minimization and geostatistical calibration. *Journal of Hydrology*, 266, 40–52.
- Jang, M., and Choe, J., 2004. An inverse system for incorporation of conditioning to pressure and streamline-based calibration. *Journal of Contaminant Hydrology*, 69, 139–156.
- Jiang, Y., and Somers, G., 2009. Modeling effects of nitrate from non-point sources on groundwater quality in an agricultural watershed in Prince Edward Island, Canada. *Hydrogeology Journal*, 17, 707–724.
- Jukic, D., and Denic-Jukic, V., 2009. Groundwater balance estimation in karst by using a conceptual rainfall-runoff model. *Journal of Hydrology*, 373, 302–315.
- Jury, W., 1982. Simulation of solute transport using a transfer function model. *Water Resources Research*, 18, 363–368.
- Jury, W. A., and Roth, K., 1990. *Transfer Functions and Solute Movement through Soil*. Birkhaeuser, Basel.

- Jury, W., Sposito, G., and White, R., 1986. A transfer function model of solute transport through soil: 1. Fundamental concepts. *Water Resources Research*, 22, 243–247.
- Jury, W., Stolzy, L., and Shouse, P., 1982. A field test of the transfer function model for predicting solute transport. *Water Resources Research*, 18, 369–375.
- Kim, S., Jo, K., Kim, D., and Jury, W. A., 2004. Determination of two-dimensional laboratory-scale dispersivities. *Hydrological Processes*, 18, 2475–2483.
- King, J. L., and Corwin, D. L., 1999. Science, Information, Technology, and the Changing Character of Public Policy in Non-Point Source Pollution, in *Assessment of Non-Point Source Pollution in the Vadose Zone*. Geophys. Monogr. Ser., vol. 108, edited by D. L. Corwin et al., pp. 309-322, AGU, Washington D.C.
- Laftouhi, N., Vanclooster, M., Jalal, M., Witam, O., Aboufirassi, M., Bahir, M., and Persoons, E., 2003. Groundwater nitrate pollution in the Essaouira Basin (Morocco). *Comptes Rendus Geoscience*, 335, 307–317.
- Lee, S. S., 2007. Unsaturated-zone leaching and saturated-zone mixing model in heterogeneous layers, *Experimental Unsaturated Soil Mechanics*. Springer Proceedings in Physics, Vol. 112, Part VI, 387–399.
- Leij, F., and Dane, J., 1990. Analytical solutions of the one-dimensional advection equation and two- or three-dimensional dispersion equation. *Water Resources Research*, 26, 1475–1482.
- Li, S., Liu, Q., and Afshari, S., 2006. An object-oriented hierarchical patch dynamics paradigm (HPDP) for modeling complex groundwater systems across multiple-scales. *Environmental Modeling and Software*, 21, 744–749.
- Lin, L., Yang, J., Zhang, B., and Zhu, Y., 2010. A simplified numerical model of 3-D groundwater and solute transport at large scale area. *Journal of Hydrodynamics*, 22, 319–328.
- Lindenschmidt, K., 2006. Testing for the transferability of a water quality model to areas of similar spatial and temporal scale based on an uncertainty vs. complexity hypothesis. *Ecological Complexity*, 3, 241–252.
- Loague, K. and Corwin, D. L., 1998. Regional-scale assessment of nonpoint source groundwater contamination. *Hydrological Processes*, 12, 957–965.
- Martin, J. C., and Wegner, R. E., 1979. Numerical solution of multiphase, two-dimensional incompressible flow using streamtube relationships. *Society of Petroleum Engineers*, 19, 313–323.

- Martín-Queller, E., Moreno-Mateos, D., Pedrocchi, C., Cervantes, J., and Martínez, G., 2010. Impacts of intensive agricultural irrigation and livestock farming on a semi-arid Mediterranean catchment. *Environmental Monitoring and Assessment*, 167, 423–435.
- Mattern, S., and Vanclooster, M., 2010. Estimating travel time of recharge water through a deep Vadose Zone using a transfer function model. *Environmental Fluid Mechanics*, 10, 121–135.
- Meerschaert, M. M., Benson, D. A., and Bäumer, B., 1999. Multidimensional advection and fractional dispersion. *Physical Review*, 59, 5026–5028.
- Mehl, S., and Hill, M. C., 2002. Development and evaluation of a local grid refinement method for block-centered finite-difference groundwater models using shared nodes. *Advances in Water Resources*, 25, 497–511.
- Mercado, A., 1976. Nitrate and chloride pollution of aquifers: a regional study with the aid of a single-cell model. *Water Resources Research*, 12, 731–747.
- Molden, D. (ed.), 2007. *Water for Food Water for Life: A Comprehensive Assessment of Water Management in Agriculture*. Earthscan, London.
- National Research Council. 1993. *Groundwater Vulnerability Assessment: Predicting Relative Contamination Potential Under Conditions of Uncertainty*. National Academy Press, Washington, DC.
- Neuman, S. P., 1990. Universal scaling of hydraulic conductivities and dispersivities in geologic media. *Water Resources Research*, 26, 1749–1758.
- Nolan, B. T., Hitt, K. J., and Ruddy, B. C., 2002. Probability of nitrate contamination in recently recharged groundwaters in the conterminous United States. *Environmental Science & Technology*, 36, 2138–2145.
- Pavlis, P., Cummins, E., and McDonnell, K., 2010. Groundwater vulnerability assessment of plant protection products. *Human and Ecological Risk Assessment*, 16, 621–650.
- Perez-Guerrero, J. S., Pimentel, L. G., Skaggs, T. H., and Van Genuchten, M. T., 2009. Analytical solution of the advection-diffusion transport equation using a change-of-variable and integral transform technique. *International Journal of Heat and Mass Transfer*, 52, 3297–3304.
- Pilbeam, C. J., Gregory, P. J., Munankarmy, R. C., and Tripathi, B. P., 2004. Leaching of nitrate from cropped rainfed terraces in the mid-hills of Nepal. *Nutrient Cycling in Agroecosystems*, 69, 221–232.

- Pinault, J. L., Pauwels, H., and Cann, C., 2001. Inverse modeling of the hydrological and the hydrochemical behavior of hydrosystems: Application to nitrate transport and denitrification. *Water Resources Research*, 37, 2179–2190.
- Pollock, D. W., 1994. User's Guide for MODPATH/MODPATH-PLOT, Version 3: A particle tracking post-processing package for MODFLOW, the U. S. Geological Survey finite-difference ground-water flow model. Open-File Report 94-464, United States Geological Survey.
- Power, J. F., and Schepers, J. S., 1989. Nitrate contamination of groundwater in North America. *Agriculture, Ecosystems & Environment*, 26, 165–187.
- Putti, M., Yeh, W., and Mulder, W., 1990. A triangular finite volume approach with high-resolution upwind terms for the solution of groundwater transport equations. *Water Resources Research*, 26, 2865–2880.
- Refsgaard, J. C., Thorsen, M., Jensen, J. B., Kleeschulte, S., and Hansen, S., 1999. Large scale modeling of groundwater contamination from nitrate leaching. *Journal of Hydrology*, 221, 117–140.
- Ruud, N. C., Harter, T., and Naugle, A. W., 2004. Estimation of groundwater pumping as closure to the water balance of a semi-arid irrigated agricultural basin. *Journal of Hydrology*, 297, 51–73.
- Saghafian, B., 2006. Nonlinear transformation of unit hydrograph. *Journal of Hydrology*, 330, 596–603.
- Siebert, S., Burke, J., Faures, J. M., Frenken, K., Hoogeveen, J., Doell, P., and Portmann, F. T., 2010. Groundwater use for irrigation – A global inventory. *Hydrology and Earth System Sciences*, 14, 1863–1880.
- Schmid, W., Hanson, R. T., Maddock III, T. M., and Leake, S. A., 2006. User's Guide for the Farm Process (FMP1) for the U.S. Geological Survey's Modular Three-Dimensional Finite-Difference Ground-Water Flow Model, MODFLOW-2000: U.S. Geological Survey Techniques and Methods 6-A17.
- Smith, B., Bjorstad, P., and Gropp, W., 1996. *Domain Decomposition : Parallel Multilevel Methods for Elliptic Partial Differential Equations*. Cambridge University Press, New York, NY.
- Sonneveld, M. P., and Bouma, J., 2003. Methodological considerations for nitrogen policies in the Netherlands including a new role for research. *Environmental Science and Policy*, 6, 501–511.
- Spalding, R. F., and Exner, M. E., 1993. Occurrence of nitrate in groundwater – A review. *Journal of Environmental Quality*, 22, 392–402.
- Spruill, T. B., Showers, W. J., and Howe, S. S., 2002. Application of classification-tree methods to identify nitrate sources in ground water. *Journal of Environmental Quality*, 31, 1538–1549.

- Stadler, S., Osenbruck, K., Knoller, K., Suckow, A., Sultenfuss, J., Oster, H., Himmelsbach, T., and Hotzl, H., 2008. Understanding the origin and fate of nitrate in groundwater of semi-arid environments. *Journal of Arid Environments*, 72, 1830–1842.
- Stewart, I. T. and Loague, K., 2003. Development of type transfer functions for regional-scale nonpoint source groundwater vulnerability assessments. *Water Resources Research*, 39, 1359.
- Stuart, M. E., Goody, D. C., Hughes, A. G., and Jackson, C. R., 2006. A field and modeling study to determine pesticide occurrence in a public water supply in Northern England, UK. *Ground Water Monitoring and Remediation*, 26, 128–136.
- Stuart, M. E., Chilton, P. J., Kinniburgh, D. G., and Cooper, D. M., 2007. Screening for long-term trends in groundwater nitrate monitoring data. *Quarterly Journal of Engineering Geology and Hydrogeology*, 40, 361–376.
- Thiele, M. R., 2001. Streamline simulation. *Proceedings of the 6th International Forum on Reservoir Simulation*. Schloss Fuschl, Austria.
- Trowsdale, S. A., and Lerner, D. N., 2007. A modeling approach to determine the origin of urban ground water. *Journal of Contaminant Hydrology*, 91, 171–183.
- UN/WWAP (United Nations/World Water Assessment Program), 2003. 1st UN World Water Development Report: Water for People, Water for Life. UNESCO/ Berghahn, Paris, New York, Oxford.
- UN/WWAP (United Nations/World Water Assessment Program), 2006. 2nd UN World Water Development Report: Water for People, Water for Life. UNESCO/ Berghahn, Paris/New York/Oxford.
- Uricchio, V. F., Giordano, R., and Lopez, N., 2004. A fuzzy knowledge-based decision support system for groundwater pollution risk evaluation. *Journal of Environmental Management*, 73, 189–197.
- Van Drecht, G., Bouwman, A. F., Knoop, J. M., Beusen, A. H. W., and Meinardi, C. R., 2003. Global modeling of the fate of nitrogen from point and nonpoint sources in soils, groundwater, and surface water. *Global Biogeochemical Cycles*, 17, 1115.
- Viers, J. H., Liptzin, D., Rosenstock, T. S., Jensen, V. B., Hollander, A. D., McNally, A., King, A. M., Kourakos, G., Lopez, E. M., De La Mora, N., Fryjoff-Hung, A., Dzurella, K. N., Canada, H. E., Laybourne, S., McKenney, C., Darby, J., Quinn, J. F., and Harter, T., 2012. Nitrogen Sources and Loading to Groundwater. Technical Report 2 in: Addressing Nitrate in California’s Drinking Water with a Focus on Tulare Lake Basin and Salinas Valley Groundwater. Report for the State Water Resources Control Board Report to the Legislature. Center for Watershed Sciences, University of California, Davis.

- Visser, A., Broers, H. P., Heerdink, R., Bierkens, M. F. P., 2009. Trends in pollutant concentrations in relation to time of recharge and reactive transport at the groundwater body scale. *Journal of Hydrology*, 369, 427–439.
- Vitousek, P. M., Naylor, R., Crews, T., David, M. B., Drinkwater, L. E., Holland, E., Johnes, P. J., Katzenberger, J., Martinelli, L. A., Matson, P. A., Nziguheba, G., Ojima, D., Palm, C. A., Robertson, G. P., Sanchez, P. A., Townsend, A. R., and Zhang, F. S., 2010. Nutrient imbalances in agricultural development. *Science*, 324, 1519–1520.
- Watanabe, N., Bergamaschi, B. A., Loftin, K. A., Meyer, M. T., and Harter, T., 2010. Use and environmental occurrence of antibiotics in freestall dairy farms with manure forage fields. *Environmental Science & Technology*, 44, 6591–6600.
- Worrall, F., Wooff, D. A., Seheult, A. H., and Coolen, F. P. A., 2000. New approaches to assessing the risk of groundwater contamination by pesticides. *Journal of the Geological Society*, 157, 877–884.
- WWAP (World Water Assessment Program), 2006. *Water: A shared Responsibility*. United Nations World Water Development Report 2.
- WWAP (World Water Assessment Program), 2009. *Water in a Changing World*, 3rd Ed. United Nations World Water Development Report 3.
- Xin-Qiang, L., Lei, X., Hua, L., Miao-Miao, H., Yi-Chao, Q., Jin, L., Ze-Yu, N., Yu-Shi, Y., and Yingxu, C., 2011. Influence of N fertilization rates, rainfall, and temperature on nitrate leaching from a rainfed winter wheat field in Taihu watershed. *Physics and Chemistry of the Earth*, 36, 395–400.
- Zhang, H., and Hiscock, K. M., (In Press). Modeling the effect of forest cover in mitigating nitrate contamination of groundwater: A case study of the Sherwood Sandstone aquifer in the East Midlands, UK. *Journal of Hydrology*, 399, 212–225.
- Zheng, C. and Wang, P. P., 1999. MT3DMS: A Modular Three-Dimensional Multispecies Transport Model for Dimulation of Advection, Dispersion and Chemical Reactions of Contaminants in Groundwater Systems: Documentation and User's Guide. Contract Report SERDP-9-1, U.S. Army Engineer Research and Development Center, Vicksburg, MS.